FACULTY OF ENGINEERING AND ARCHITECTURE

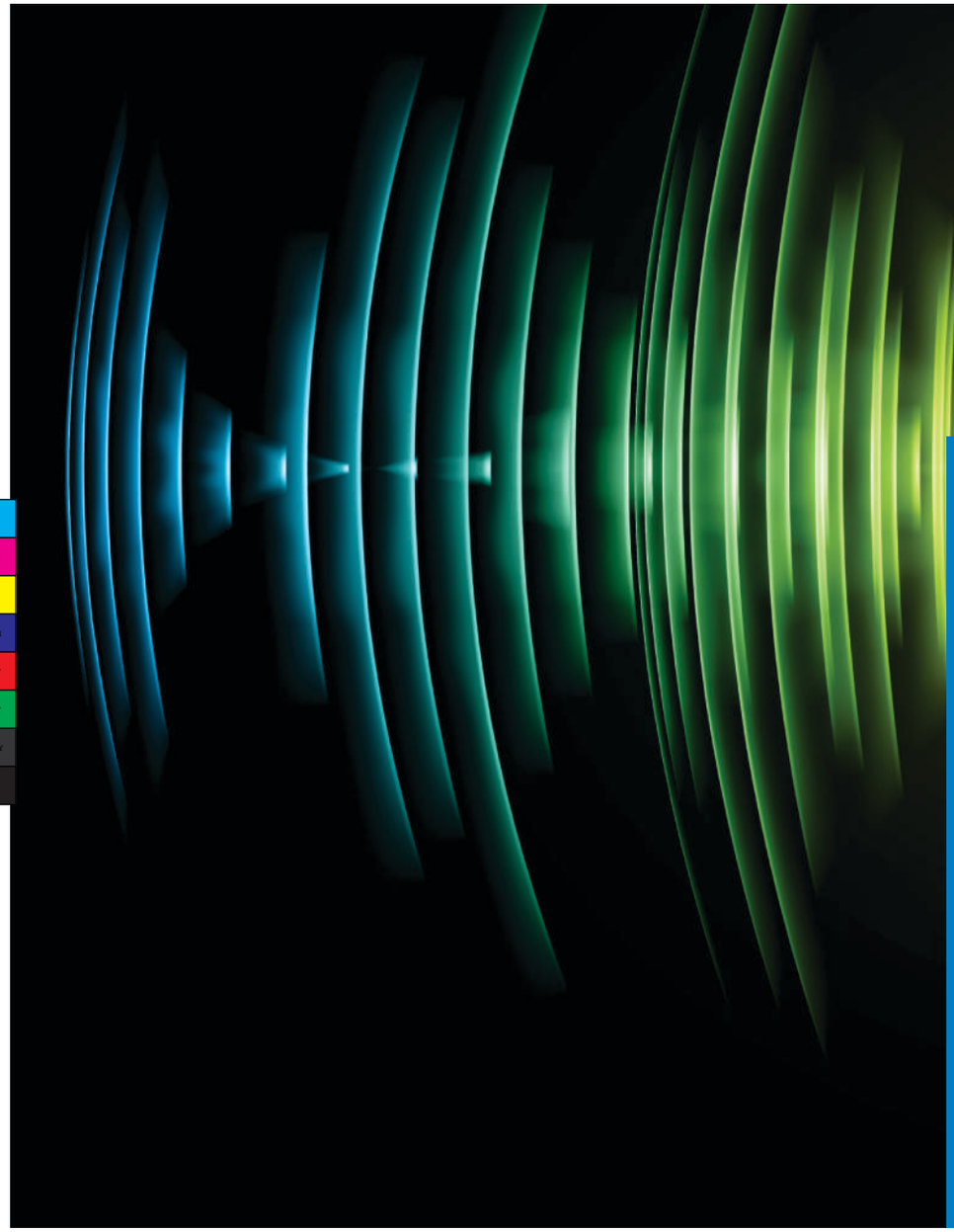

A graphical illustration of oscillating acoustic waves.

Irfan Ansari - doctoral dissertation

Electro-Optomechanical Transduction in Silicon Photonics through PZT Thin Film Integration

Irfan Ansari

Doctoral dissertation submitted to obtain the academic degree of
Doctor of Photonics Engineering

Supervisors

Prof. Dries Van Thourhout, PhD* - Prof. Jeroen Beeckman, PhD**

* Department of Information Technology
Faculty of Engineering and Architecture, Ghent University

** Department of Electronics and Information Systems
Faculty of Engineering and Architecture, Ghent University

December 2023

2023

GHENT UNIVERSITY

FACULTY OF ENGINEERING AND ARCHITECTURE

Electro-Optomechanical Transduction in Silicon Photonics through PZT Thin Film Integration

Irfan Ansari

Doctoral dissertation submitted to obtain the academic degree of
Doctor of Photonics Engineering

Supervisors

Prof. Dries Van Thourhout, PhD* - Prof. Jeroen Beeckman, PhD**

* Department of Information Technology
Faculty of Engineering and Architecture, Ghent University

** Department of Electronics and Information Systems
Faculty of Engineering and Architecture, Ghent University

December 2023

GHENT UNIVERSITY

ISBN 978-94-6355-791-7
NUR 965, 950
Wettelijk depot: D/2023/10.500/123

Members of the Examination Board

Chair

Prof. Filip De Turck, PhD, Ghent University

Other members entitled to vote

Prof. Klaartje De Buysser, PhD, Ghent University
Prof. Bart Kuyken, PhD, Ghent University
Prof. David Marpaung, PhD, Universiteit Twente, the Netherlands
Sandeep Seema Saseendran, PhD, imec

Supervisors

Prof. Dries Van Thourhout, PhD, Ghent University
Prof. Jeroen Beeckman, PhD, Ghent University

Acknowledgement

This journey has been a rollercoaster of experiences, filled with ups and downs (though, truth be told, the downs seemed to dominate). Sometimes, every step in the right direction seemed to come after galloping through all the possible wrong trajectories. Perhaps it was another testament to the famous/infamous Murphy's law or just a series of uncanny coincidences. After all, the world doesn't often announce a pandemic shutdown while you're in the midst of your Ph.D. Nevertheless, I find solace in acknowledging the fact that this journey has taught me invaluable lessons. It cultivated a sense of humility, patience, and perseverance well before the fruits of victory could be savored.

Now that the ship is ready to dock, I look back and feel grateful to all those who helped me sail through this journey. First and foremost, I am thankful to my advisors, Prof. Dries Van Thourhout and Prof. Jeroen Beeckman, for their support, mentorship, and invaluable insights. Their guidance has been instrumental in shaping the direction of my research and academic growth. I was lucky to have two active supervisors, which ensured that at least one of them could be available when needed. Also, thank you for going through the agonizing review process of my manuscripts and thesis. This exhaustive process of back-and-forth feedback gave me a glimpse of an academic path. As you can see, I chose an industrial path now, perhaps to not have to go through such a process myself.

I would also like to thank other professors in the PRG group: Roel Baets, Peter Bienstman, Wim Bogaerts, Geert Morthier, Gunther Roelkens, Nicolas Le Thomas, and Yanlu Li, and in the LCP group: Kristiaan Neyts, Filip Beunis, Filip Strubbe and Johan Lauwaert. You have always been there for any questions or spontaneous 'corridor meetings' to discuss anything. I would also like to extend my appreciation to the members of my Ph.D. examination committee, Prof. Filip De Turck, Prof. Bart Kuyken, Prof. Klaartje De Buysser, Prof. David Marpaung, and Dr. Sandeep Seema Saseendran, for their thoughtful feedback and constructive criticism, which greatly embellished the quality of this thesis.

I am grateful to all those teachers, mentors, and advisors whose guidance laid the crucial foundation upon which my Ph.D. dissertation stands today. My journey in photonics began during my undergraduate studies with the 'Introduction to Photonics' course led by Prof. Manoj Varma and Prof. Ambarish Ghosh at IISc Bangalore. This initial exposure sparked my passion, leading me to embark on

both my bachelor's and master's thesis projects in photonics at the physics department of IISc and ICFO Barcelona, respectively. Later, I had hands-on experience in integrated silicon photonics while working in Prof. Shankar Kumar Selvaraja's lab at IISc, where he introduced me to the PRG group, his alma mater.

I vividly remember the first day I arrived in Gent, and woke up the next day with snow cover everywhere. Amidst that surreal scenery, I arrived at the PRG group and was immediately taken by surprise by the friendliness of the staff members. From handling administration to helping with onboarding, Mike Van Puyenbroeck, Bert Coryn, Ilse Meersman, and Ilse Var Royen helped me in every way possible and continued to support me throughout my journey. Dealing with the paperwork in Belgium would have been a nightmare without their intervention. Kristien De Meulder, thank you for solving our often stupid computer-related issues, without making us feel stupid. I still think you might have some magic tricks that fixed some issues with your presence itself. Steven, Muneeb, and Liesbet, thank you for being the tripod of the cleanroom support system. Without your help and guidance, I don't know how many more of my devices would have collapsed. Thanks to Jasper Jans and Clemens for helping with the measurement setups. Special thanks to Clemens for reducing the entropy of the lab. Thanks to Thomas Vervust (CMST) for the DWL, David Schaubroeck (CMST) for the ALD deposition, Joris (IDlab) for being my RF troubleshooter, and Nish (IDlab) for helping with the high-speed modulator-related queries.

I had started my PhD with a subgroup 'optomechanics' consisting of Jesper, Paul, Khannan, and Awanish. I am thankful to everyone for the discussions and support. Special thanks to Jesper and Awanish, who were always available to help and share their experience. Subsequently, I became a part of a new 'PZT' subgroup consisting of Gilles, Tessa, and John, and later joined by Ewout, Kobe, Enes and Hannes. Thank you everyone for trying your best. Special thanks to John and Tessa for their support with the PZT fabrication in the beginning, and meneer Gilles for giving me the pep talk when I felt low. Thank you, Enes, for breaking the ceiling for the gown size in the CR, from XXL to "Enes". If only they had delivered your gown in time while John was still in Gent....

I started with the 3rd floor office in the iGent tower, which soon became the most fun office in the group, special thanks to Soren, Alejandro, Mahmoud and Javad. The 'best out of the three' dart game was a guilty pleasure. Pre- Covid era was filled with social lunch on the 5th-floor kitchen, which saw evolutions of several friendships. Thanks to Clemens, Nina, Joan, Lukas x2, Antonio, Sarah, Mahmoud, Alejandro, Alessio, Andrew, Stijn, Sanja, Khannan, Ivo, Alex, Banafsheh, Bahawal, Ali, Ewoud, Emmanuel and many more who made lunch break a fun break. Alex, on your first day at the PRG lunch, I asked you to join me for a relay marathon, which you declined. But I can't thank you enough for joining the day-to-day marathon of life and helping me move forward through the highs and lows. Also, thanks to Clemens, Alex, Mattias, Evangelia, Meryem, Jing, Chupao, Emad, and Pan for bringing positivity and fun to the new office on the 5th floor. Clemens, I hope one day you can buy a Santec with cash or epurse. Thanks Emiel and Yanlu for helping with the LDV setup, Jasper and Tom x2 for helping with the

transfer printing. Thanks Isaac, Khannan, Clemens, Alex, Kristof, and Manuel, for creating new WhatsApp groups for every new activity. Thank you Kristof for teaching some Dutch, now I can say 'Hoe gaat het met jouw' with an almost perfect Flemish accent. Alessio, Alejandro, and Kristof, thanks for the ping-pong breaks. Luis, thank you for giving me hope to organize Chinese cooking together with Chao and Tao. Thanks Laurens, for always being available to discuss any RF-related questions. Thank you Abdul for your unparalleled enthusiasm to discuss photonics market and epixfab events. Thanks Nagarjun and Khannan for feeding me with South Indian food, science, and philosophy. Thanks Tom Reep for constantly asking about my thesis progress, I look forward to returning the favor soon. Thanks Stijn Poelman, Jasper, Lucas Oorlynck and Lukas Elsinger for organizing the bike rides, and Iman and Luis for organizing the beach volleyball. I also enjoyed organizing and participating in the PSG events. Thanks to its cool members Migle, Khannan, Camiel, Lucas, Freddy, Brecht, and Ingrid. If I am missing anyone acknowledgement-worthy, my apologies.

I am also thankful to the expat group of friends who made sure that I remained sane during my PhD journey. Thanks to Alex, Briana, Ana, Benoit, Oleh, Mia, Rupert, and Sam for being awesome friends. What started with a small bunch of people hanging out after the Dutch class, gradually evolved into a bigger group, now coined as 'Corona BBQ'. Although we haven't organized a BBQ in a very long time, definitely not during the Covid. Thanks Marghe, Alessio, Savvina, Mahmoud and Nina for organizing the activities. Thanks Kamal, Ananth, Saurav, Sulakshana, Sarvagya, and Awanish for organizing the pakwan gathering from time to time. It certainly helped alleviate my homesickness. Thanks to Wout and Raveena for the temporary shelter during the end of my thesis writing. I'm grateful to Alex, Kelvin, and Clemens for helping with the stressful moving during the last phase of my thesis writing. Thanks Shraavya for joining the force with the house change and taking extra responsibilities so I could focus on running the last miles of the thesis.

I am lucky to have life-long friends who bestow their support and friendship no matter where they are located. Special mention to a few of my former classmates, Nikunj, Vamsi KV, Pranav Gupta, Pranav Garg, Sunny, Akash, Akshya, Arjun, Praveer, Sathya, Martin, and Athi. Also, thanks to the friends from ICFO, especially Alex and Manab.

I would like to express my gratitude to Geerke for her support and encouragement during the challenging times of my Ph.D. Thank you for your companionship and positive influence. Lastly, I extend my heartfelt appreciation to Amma, Abba, Bhaiya, Bhabhi, and my extended family for their unconditional love, encouragement, and sacrifices that made this academic achievement possible.
To everyone who has been a part of this journey, thank you for being the bedrock of my success.

Gent, December 2023
Irfan Ansari

Table of Contents

List of Figures

List of Tables

List of Acronyms

AC	Alternating Current
AOM	Acousto-Optic Modulator
ALD	Atomic Layer Deposition
Ar	Argon
ASH	Average Slope Height
BHF	Buffered Hydrofluoric Acid
BTO	Barium Titanate
CCD	Charge-Coupled Device
C-band	Communications Band
CMP	Chemical Mechanical Polishing
CMOS	Complementary Metal-Oxide-Semiconductor
CSD	Chemical Solution Deposition
DC	Direct Current
DUT	Device Under Test
EO	Electro-Optic
EMC	Electromagnetic Compatibility
ESA	Electrical Spectrum Analyzer
FEM	Finite Element Method
FFT	Fast Fourier Transformation
GDS	Graphic Design System
HF	Hydrofluoric Acid
ICP	Inductively Coupled Plasma
IDT	Interdigitated Transducer
LDV	Laser Doppler Vibrometry
LN	Lithium Niobate
MB	Moving Boundary
MEMS	Micro-Electro-Mechanical System
MPW	Multi-Project Wafer
PECVD	Plasma-Enhanced Chemical Vapor Deposition
PE	Photoelastic Effect
PICs	Photonic Integrated Circuits
PR	Photoresist
PZT	Lead Zirconate Titanate
RF	Radio Frequency
RIE	Reactive Ion Etching
SAW	Surface Acoustic Wave

SEM	Scanning Electron Microscope
Si	Silicon
SOI	Silicon-on-Insulator
SOLT	Short-Open-Load-Through
UV	Ultraviolet
VNA	Vector Network Analyzer
WG	Waveguide

Nederlandse Samenvatting

Inleiding

Silicium (Si) fotonica heeft de afgelopen decennia een ongekende groei doorgemaakt, voornamelijk vanwege de compatibiliteit met bestaande fabricagemethodes voor geïntegreerde schakelingen (IC) [1]. Als gevolg daarvan is de Si fotonische geïntegreerde schakeling (PIC) gecommercialiseerd en heeft het toepassingen gevonden in verschillende gebieden, waaronder telecommunicatie, sensortechnologie en informatieverwerking. Desalniettemin zorgt de snelle vooruitgang van de moderne technologie voortdurend voor het verleggen van de grenzen van PIC technologie. Een voorbeeld is het opnemen van piezoelektrische functionaliteit in PIC's om de dynamische controle van optische eigenschappen, precieze optische frequentiereferenties, efficiënte amplitude- en frequentiemodulatie, en niet-reciproke lichtgeleiding te realiseren. Hoewel sommige piëzoelektrische dunne lagen zoals AlN, ZnO en $LiNbO_3$ zijn geïntegreerd in een Si PIC, heeft hun zwakke piëzo-reactie de volledige potentie van de piëzomechanismen binnen Si PICs beperkt. Daarom blijft de zoektocht naar een robuust piëzoelektrisch materiaal dat naadloos integreert met Si PICs een lopende inspanning.

Onlangs werd de directe integratie van een PZT dunne laag gedemonstreerd met behulp van Chemical Solution Deposition (CSD). Deze methode maakt gebruik van een ultradunne (10-15 nm) transparante La-gebaseerde bufferlaag, waardoor de PZT-laag compatibel is met de PICs [2]. De hoge kwaliteit van de laag werd aangetoond door de realisatie van een efficiënte Pockels-modulator met lage propagatieverliezen op een SiN-platform [3]. Bovendien getuigt succesvolle tweede harmonische generatie met behulp van de PZT-film van het potentieel van dit materiaal voor niet-lineaire optische toepassingen [4]. In deze scriptie onderzoeken we de piëzoelektrische eigenschappen van deze laag om lichtsignalen in Si PICs te regelen en te manipuleren.

Belangrijkste resultaten

Om de piëzoelektrische mogelijkheden van de PZT-lagen te testen, werd een interdigitale transducer (IDT) gedefinieerd bovenop een PZT-laag die was afgezet op een glasplaatje. De IDT werd aangestuurd met een RF-signaal op verschillende frequenties. Wanneer een IDT wordt geactiveerd bij zijn resonantiefrequentie, wordt een deel van de elektrische energie omgezet in mechanische energie. Dit

manifesteert zich als een dip in de verstrooiingsparameter S_{11}. Door de S_{11} van de IDTs met gepoolde en ongepoolde PZT-lagen te meten, ontdekten we dat de uitlijning van de PZT-domeinpolarisatie cruciaal was voor de efficiënte activering van acoustische golven (SAW). Voor een efficiënte SAW-transductie moet de polarisatie van het PZT-domein langs de aangelegde elektrische veldlijnen liggen.

Na de elektrische karakterisering van de SAW-transductie werd een PZT-laag geïntegreerd op een geplanariseerde Si fotonische chip. Daarna werden IDT's bovenop de PZT laag gedefinieerd. Nu loopt de geactiveerde SAW door de golfgeleider en de SAW moduleert het lichtsignaal in de golfgeleider door foto-elastische koppeling. De fasemodulatie in het uitgangslicht wordt gemeten met behulp van een heterodyne-opstelling zoals getoond in figuur 4(a). Wanneer de fase van het invoerlicht wordt gemoduleerd, verschijnt er een zijband in het frequentiedomein van het uitgangslicht, zoals te zien is in figuur 4(b). De piekvermogens van de zijband geven de mate van fasemodulatie aan. Wanneer dit piekmodulatievermogen genormaliseerd wordt met het piekvermogen van de akoesto-optische modulator (AOM), geeft dit de modulatie-efficiëntie.

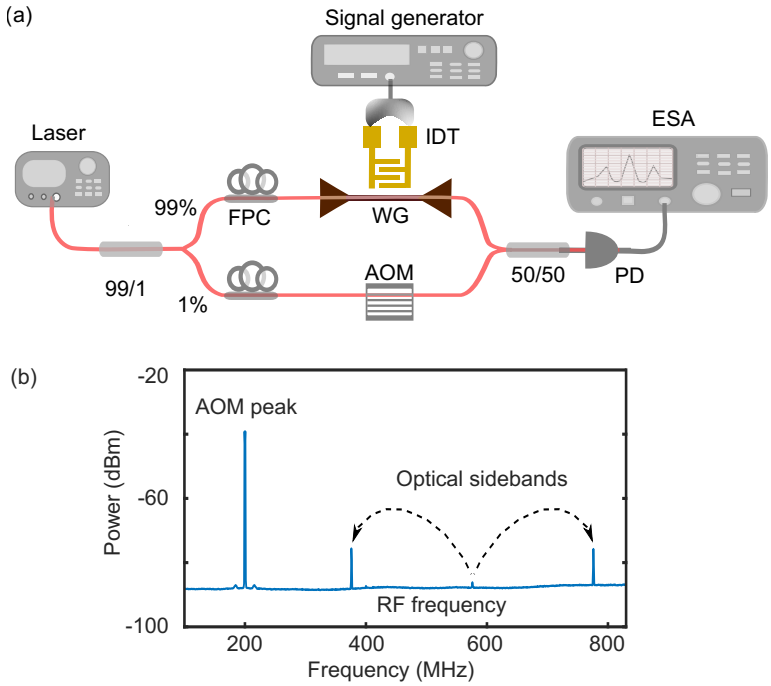

Figuur 1: (a) Een heterodyne opstelling gebruikt voor het meten van de fasemodulatie, (b) Zijbanden die verschijnen in het uitgangsspectrum als gevolg van de fasemodulatie van het licht.

Figuur 5(a) toont een schematische weergave van een SAW-modulator geïntegreerd op een fotonische chip. Figuur 5(b) toont de optische modulatie gemeten in een

golfgeleider door een IDT met een periode van 12 μm, 20 vingerparen en een opening van 100 μm te activeren. De pieken in het modulatiespectrum komen overeen met de verschillende akoestische modi die zijn geactiveerd met de IDT. We verkregen een VπL van ongeveer 3,35 V·cm bij 576 MHz voor een 350 nm dikke Au IDT. Door middel van simulaties wezen we op de hoge massa en reflecties van IDTs gedefinieerd in een goud laag, die de werking nadelig beïnvloeden. Daarom werd een nieuwe component met een dikte van 100 nm en een kleinere periode (2 μm) van aluminium (Al) gefabriceerd om GHz akoestische golven te activeren. Al werd gebruikt voor de IDT vanwege de lagere (ongeveer 1/7) dichtheid in vergelijking met Au , wat het effect van massa-belasting kan verminderen zoals bleek uit onze simulatie. We verkregen een VπL van ongeveer 3,6 V·cm met de Al IDT, bestaande uit slechts 4 vingerparen.

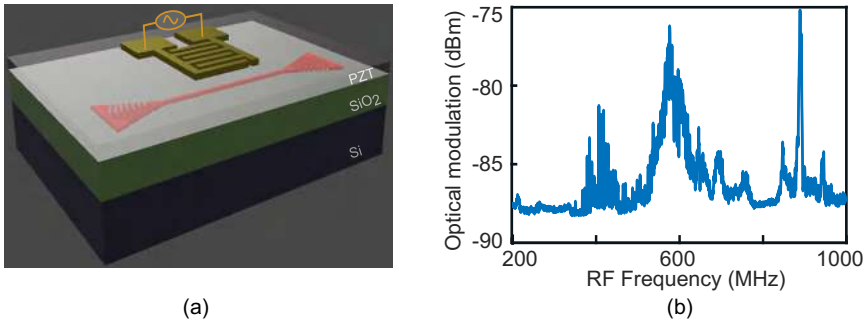

Figuur 2: (a) 3D schematisch diagram van een SAW-modulator (b) Fasemodulatie gemeten in de golfgeleider met betrekking tot de aangelegde RF-frequentie.

Vervolgens optimaliseerden we een proces om ondergeëtste PZT-gebaseerde micro-elektromechanische structuren (MEMS) te fabriceren. Een ondergeëtste PZT laag op een Si substraat werd gefabriceerd door de onderliggende SiO_2 laag weg te etsen met waterstoffluoride (HF) damp. De component werd aangedreven met een RF-signaal en gekarakteriseerd met een laser-Doppler-vibrometer (LDV).

Na verificatie van de MEMS-actuatie werden MEMS-structuren gedefinieerd binnen Si PIC's. Een van dergelijke structuren was een elektro-opto-mechanische transducer (EOMT), met een vrijhangende elektro-optische modulatorstructuur zoals getoond in figuur 6 (a). We ontdekten dat dit apparaat zowel een breedband modulatie door het elektro-optische effect als een smalband modulatie door de mechanische resonantie aangedreven door het piëzo-elektrische effect vertoont. Hun interferentie resulteert in een Fano-resonantie in het microgolfgebied, zoals gepresenteerd in figuur 6 (b). We observeren Fano-resonanties bij frequenties tot 6,7 GHz met een extinctieverhouding van 21 dB, en een hoge extinctieverhouding van 41 dB bij de primaire resonantie van 223 MHz.

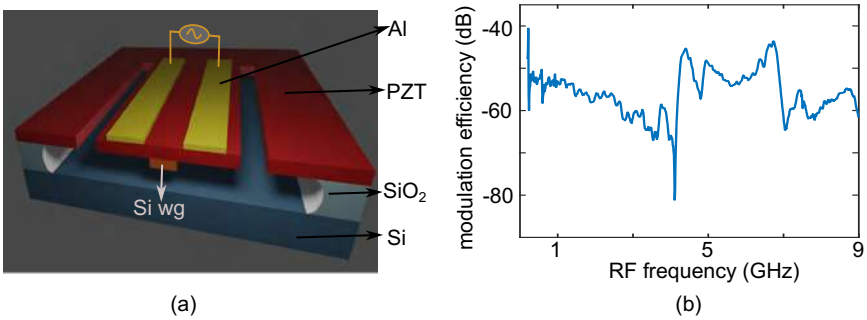

Figuur 3: (a) 3D schematisch diagram van een fotonisch MEMS-apparaat (b) Modulatie-efficiëntie gemeten in de golfgeleider met betrekking tot de aandrijvende RF-frequentie.

Conclusie

We hebben een sterk piëzo-elektrisch effect aangetoond in onze PZT lagen door de faseverandering veroorzaakt door een SAW te meten. Uit dit onderzoek bleek dat het polingsproces op onze ferro-elektrische PZT laag en het ontwerp van de IDT met dunne metalen van lage dichtheid zeer belangrijk zijn voor een efficiënte SAW-transductie. Het polingsproces wordt uitgevoerd om de PZT-domeinen langs de aangelegde elektrische veldlijnen uit te lijnen, wat zorgt voor een sterke longitudinale transductie. Bovendien helpt het ontwerp van de IDT met dunne metalen van lage dichtheid om het massaloading-effect en de grating-reflectie te verminderen. We hebben ook opgemerkt dat ons onderetsproces met HF-damp enkele bijproducten van SiO_2-etsing onder de PZT-laag achterlaat. Dit bemoeilijkt de transfer-printing van de PZT-coupons. Ten slotte hebben we een Si-fotonische MEMS-component ontworpen en piëzo-elektrisch aangedreven Fano-resonanties gedemonstreerd in het microgolfgebied. Dit kan nieuwe mogelijkheden bieden voor de ontwikkeling van zeer gevoelige en efficiënte componenten voor diverse toepassingen, waaronder sensoren, filters, schakelaars en modulatoren.

References

[1] Bahram Jalali and Sasan Fathpour. *Silicon Photonics*. Journal of Lightwave Technology, 24(12):4600–4615, 2006.

[2] J. P. George, P. F. Smet, J. Botterman, V. Bliznuk, W. Woestenborghs, D. Van Thourhout, K. Neyts, and J. Beeckman. *Lanthanide-Assisted Deposition of Strongly Electro-optic PZT Thin Films on Silicon: Toward Integrated Active Nanophotonic Devices*. ACS Applied Materials & Interfaces, 7(24):13350–13359, 2015.

[3] Koen Alexander, John P. George, Jochem Verbist, Kristiaan Neyts, Bart Kuyken, Dries Van Thourhout, and Jeroen Beeckman. *Nanophotonic Pockels modulators on a silicon nitride platform*. Nature Communications, 9(1):4–9, 2018.

[4] Gilles F. Feutmba, Artur Hermans, John P. George, Hannes Rijckaert, Irfan Ansari, Dries Van Thourhout, and Jeroen Beeckman. *Reversible and Tunable Second-Order Nonlinear Optical Susceptibility in PZT Thin Films for Integrated Optics*. Advanced Optical Materials, n/a(n/a):2100149.

English summary

Introduction

Silicon (Si) photonics has witnessed an unprecedented growth in the past decades, primarily due to its compatibility with the existing integrated circuit (IC) fabrication [1]. As a result, Si photonic integrated circuits (PICs) have been commercialized and the technology has found applications in several areas, including telecommunication, sensing technology and quantum information processing. However, the rapid advancement of modern technology consistently challenges the limits of PIC technology. One such advancement is to incorporate piezoelectric capabilities in PICs to realize the dynamic control of optical properties, precise optical frequency references, efficient amplitude and frequency modulation, and non-reciprocal light routing. Although some piezoelectric thin films like AlN, ZnO, and $LiNbO_3$ have been integrated into Si PICs, their weak piezo-response has curtailed the full potential of the piezoelectric mechanisms within Si PICs. Consequently, the quest for a robust piezoelectric material that seamlessly integrates with Si PICs remains an ongoing endeavor.

Recently, the direct integration of a PZT thin film on PICs was demonstrated using chemical solution deposition (CSD). This method uses an ultra-thin (10-15 nm) transparent La based buffer layer, rendering the PZT film compatible with PICs [2]. The high quality of the film was showcased through the realization of a strong Pockels modulator with a low propagation loss on a SiN platform [3]. Additionally, successful second harmonic generation from the PZT film further attests to the potential of this material for novel non-linear photonic applications [4]. In this thesis, we delve into the piezoelectric capability of this film to control and manipulate light signals in Si PICs.

Key results

To test the piezoelectric actuation of the PZT film, an inter-digitated transducer (IDT) was defined on top of the PZT film deposited on a glass substrate. The IDT was driven with an RF signal at different frequencies. When an IDT is actuated at its resonance frequency, a part of the input electrical energy is transduced into mechanical energy. This is manifested as a dip in the reflection scattering parameter S_{11}. By measuring the S_{11} of the IDTs with poled and unpoled PZT layer, we found that the alignment of the PZT domain polarization was crucial for the

actuation of surface acoustic waves (SAW). For an efficient SAW transduction, the PZT domain polarization must be along the applied electric field lines.

After the electrical characterization of the SAW transduction, a PZT film was integrated onto a planarized Si photonic chip. Thereafter, IDTs were defined on top of the PZT film. The actuated SAW travels through the waveguide and modulates the light signal in the waveguide through the photoelastic coupling. The phase modulation in the output light is measured using a heterodyne setup as shown in figure 4(a). When the phase of the input light is modulated, a sideband appears in the frequency domain of the output light, as can be seen in figure 4(b). The peak power of the sideband indicates the extent of the phase modulation. When this peak modulation power is normalized with the peak power of the acousto-optic modulator (AOM), it gives modulation efficiency.

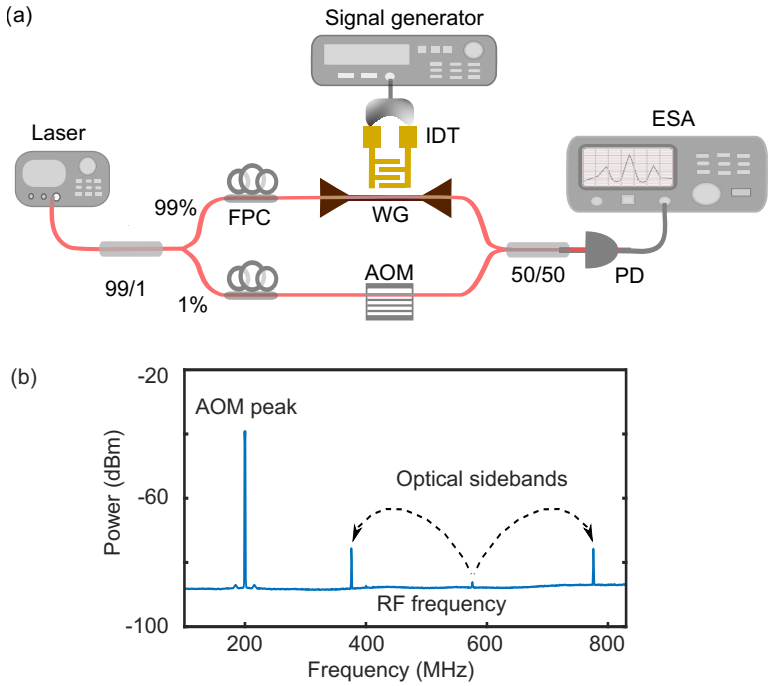

Figure 4: (a) A heterodyne setup used for measuring the phase modulation, (b) Sidebands appearing in the output spectrum due to the phase modulation of the input light.

Figure 5(a) illustrates a schematic of a SAW modulator integrated on a photonic chip. Figure 5(b) shows the optical modulation measured in a waveguide from an IDT of 12 μm period, 20 finger-pairs, and 100 μm aperture. The peaks in the modulation spectrum correspond to the different acoustic modes actuated with the IDT. We obtained a half-wavelength voltage length product $V_{\pi}L \sim 3.35$ V·cm at 576 MHz from a 350 nm thick gold (Au) IDT. Through computational analysis, we pointed out the issue of mass-loading and grating reflection stemming from

the thick Au IDT, which was severely hampering the device performance. Subsequently, a new device with 100 nm thick and smaller period (2 μm) Aluminum (Al) IDT was fabricated to actuate GHz acoustic waves. Al was used for the IDT because of its lower ($\sim$ 1/7) density compared to the Au IDT, which can mitigate the mass-loading effect, as seen from our simulation. We obtained a competitive $V_\pi L \sim 3.6$ V·cm with the Al IDT consisting of only 4 finger-pairs.

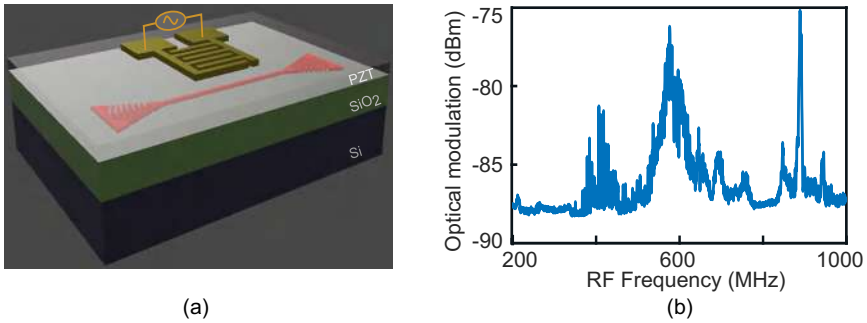

Figure 5: (a) 3D schematic of a SAW modulator (b) phase modulation measured in the waveguide with respect to the driving RF frequency.

Next, we optimized a process flow to fabricate suspended PZT based microelectromechanical system (MEMS) devices. A suspended PZT on Si device was fabricated by undercutting the SiO_2 sacrificial layer with hydrogen fluoride (HF) vapor. The device was driven with an RF signal and its actuation was characterized with a laser Doppler vibrometry (LDV). Additionally, we showcased the suspension of long PZT coupons using the same process flow. Some PZT coupons were successfully transfer-printed on a Si target sample. But, some PZT coupons had bonding issues due to the residues underneath the PZT film. We suspect these residues could be some by-products of the HF vapor etching process.

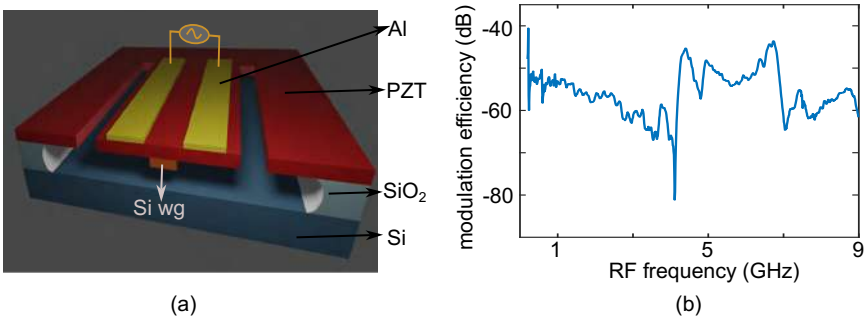

Figure 6: (a) 3D schematic of a photonic MEMS device (b) modulation efficiency measured in the waveguide with respect to the driving RF frequency.

After confirming the MEMS actuation, the MEMS devices were defined within

Si PICs. One such structure was an electro-optomechanical transducer (EOMT), where an electro-optic modulator structure was suspended as shown in figure 6(a). We found that this device can leverage a broadband modulation from the electro-optic effect and a narrow band modulation from the mechanical resonance driven with the piezoelectric effect. Their interference results in a Fano resonance in the microwave domain as presented in figure 6(b). We observe Fano resonances at frequencies up to 6.7 GHz with an extinction ratio of 21 dB, and a high extinction ratio of 41 dB at the primary resonance 223 MHz.

Conclusion

We demonstrated a strong piezoelectric effect in our PZT film by measuring the SAW-induced phase modulation. Through this investigation, we realized that the poling process on our ferroelectric PZT film, and the design of the IDT with thin and low-density metals are very important for efficient SAW transduction. The poling process aligns the PZT domains along the applied electric field lines, which procures a strong longitudinal transduction. And the design of the IDT with low-density thin metal mitigates the mass-loading effect and grating reflection. We also observed that our under-etching process with HF vapor leaves some by-products from the SiO_2 etching, underneath the PZT layer. This hampers the transfer-printing of the PZT coupons. Finally, we designed a Si photonic MEMS device and demonstrated piezoelectrically driven Fano resonances in the microwave domains. This could open up new possibilities for the development of highly sensitive and efficient devices for a range of applications, including sensing, filtering, switching, and modulation.

References

[1] Bahram Jalali and Sasan Fathpour. *Silicon Photonics*. Journal of Lightwave Technology, 24(12):4600–4615, 2006.

[2] J. P. George, P. F. Smet, J. Botterman, V. Bliznuk, W. Woestenborghs, D. Van Thourhout, K. Neyts, and J. Beeckman. *Lanthanide-Assisted Deposition of Strongly Electro-optic PZT Thin Films on Silicon: Toward Integrated Active Nanophotonic Devices*. ACS Applied Materials & Interfaces, 7(24):13350–13359, 2015.

[3] Koen Alexander, John P. George, Jochem Verbist, Kristiaan Neyts, Bart Kuyken, Dries Van Thourhout, and Jeroen Beeckman. *Nanophotonic Pockels modulators on a silicon nitride platform*. Nature Communications, 9(1):4–9, 2018.

[4] Gilles F. Feutmba, Artur Hermans, John P. George, Hannes Rijckaert, Irfan Ansari, Dries Van Thourhout, and Jeroen Beeckman. *Reversible and Tunable*

Second-Order Nonlinear Optical Susceptibility in PZT Thin Films for Integrated Optics. Advanced Optical Materials, n/a(n/a):2100149.

1 Introduction

In the realm of modern photonics, where the manipulation of light promises extraordinary advancement, the integration of diverse materials and novel mechanisms into established platforms stands as a hallmark of innovation. Among these pioneering pursuits, the fusion of piezoelectric thin films with silicon photonics has emerged as a captivating frontier. This journey begins at this junction where the pulse of light meets the heartbeat of mechanics, promising a future filled with awe and wonder.

1.1 Background and motivation

Photonic integrated circuits (PICs) have gained remarkable traction due to their potential to revolutionize various fields, including telecommunications, data processing, sensing, and quantum information. Among these, the silicon-on-insulator (SOI) based photonic platform has stood out due to its high index contrast and compatibility with complementary metal-oxide-semiconductor (CMOS) fabrication processes, enabling scalability, mass production and the coexistence of electronic and photonic components on a single chip [1–3]. Nonetheless, Si PICs have struggled to keep pace with the growing demands of new functionalities on a photonic chip. One of the crucial lacking features in Si PICs is the piezoelectric effect, as crystalline Si does not exhibit this effect due to its centrosymmetric crystal structure [4–6].

The piezoelectric effect is a phenomenon observed in materials lacking cen-

trosymmetry, wherein the application of force or mechanical stress leads to the generation of electric charges in the material [7]. This mechanism, also known as the direct piezoelectric effect, is depicted in figure 1.1 (a). Conversely, when an electric field is applied to the piezoelectric material, it causes a change in its shape or mechanical deformation. This mechanism, known as the inverse piezoelectric effect, is illustrated in figure 1.1 (b).

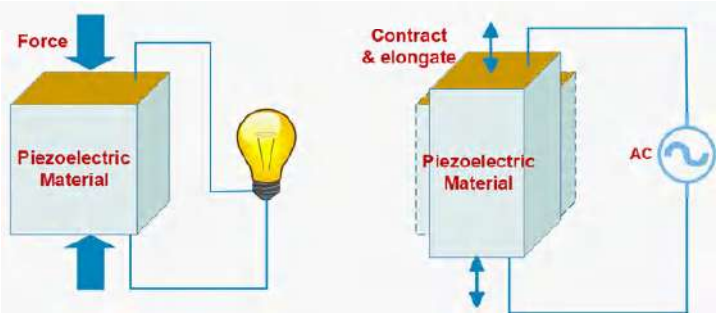

Figure 1.1: (a) Direct piezoelectric effect (b) Indirect piezoelectric effect [8].

1.1.1 Piezoelectric SAW actuation

The piezoelectric effect has been harnessed in non-centrosymmetric photonic platforms such as $LiNbO_3$ [9–13], GaAs [14–17] and InP [18, 19] to generate surface acoustic wave (SAW), enabling various photonic applications including narrowband modulation, filters, mode-shifters, non-reciprocal light transmission and frequency comb generation.

A SAW is generated by creating a time-varying periodic deformation pattern along the surface of an elastic material [20]. This deformation can be generated piezoelectrically by defining an inter-digital transducer (IDT) on top of the piezoelectric substrate or a piezoelectric thin film integrated on an elastic substrate. A typical design of an IDT is illustrated in figure 1.2(a). The IDT consists of interleaved metal electrodes deposited on a piezoelectric substrate. When an alternating electrical signal is applied to these electrodes, it generates a periodic stress pattern in the underlying piezoelectric material due to the indirect piezoelectric effect. This stress pattern launches surface acoustic waves that propagate along the material's surface within half of the SAW wavelength. The electric potential from an IDT and the resulting deformation at the SAW actuation are shown in the simulation of a unit IDT cell[1] in figure 1.2 (b) and (c), respectively. Conversely,

[1]The piezoelectric simulation of the SAW mode was carried out with COMSOL, a finite element method (FEM) based solver. For simulation details, see appendix B.3

when a SAW interacts with the IDT, it induces an alternating electrical signal in the electrodes through the direct piezoelectric effect. The IDT-actuated SAWs are widely used for frequency-selective filtering in electronic circuits [21].

The periodic arrangement of the electrodes defines the wavelength and characteristics of the generated SAW. The SAW resonance frequency is determined by its wavelength, the acoustic phase velocity of the medium, and the boundary condition (free surface) [21, 22].

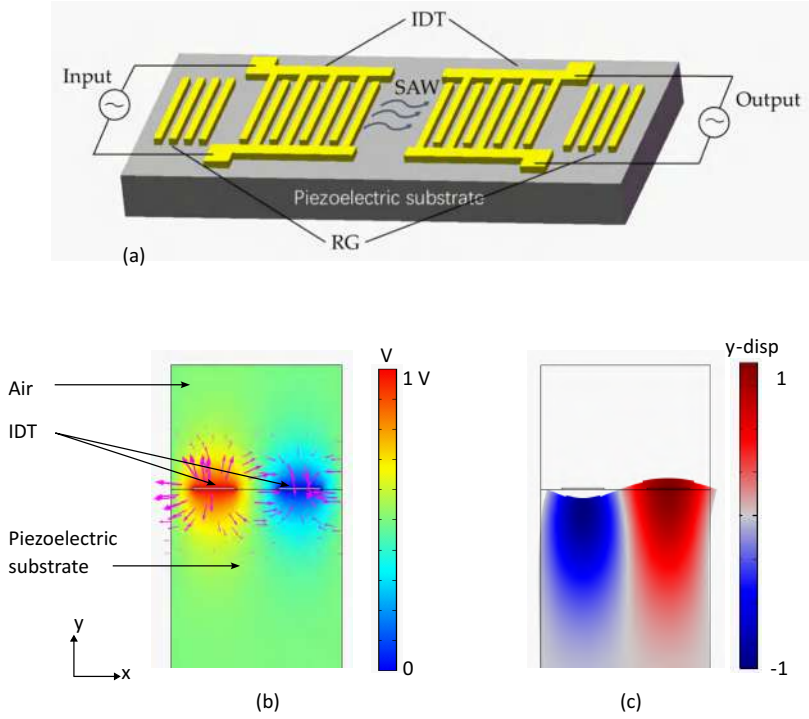

Figure 1.2: (a) A SAW-based RF filter with a transmitter and receiver IDT [23], (b) 2D simulation showing the electric potential (electric field lines depicted with arrows) from an IDT, (c) 2D simulation showing the vertical (along y) displacement profile at SAW excitation.

When a SAW is introduced into integrated photonics, the spatiotemporal profile of a traveling SAW creates a refractive index modulation in the waveguide material through the photoelastic effect [24]. This index grating scatters the incoming light signal into stokes and anti-stokes signals, as depicted in figure 1.3(a). In the SOI photonic platform, the SAW actuation has been mainly achieved through piezoelectric thin film integration, followed by the fabrication of an IDT on top. For instance, [25] reported a half-wave-voltage-length (V_πL) of 1.8 V·cm at 3.11

GHz through AlN integration. However, AlN exhibits a low-piezoelectric response, which curtails the performance of such a device. Although scandium (Sc) doped AlN has been explored for Si PIC integration due to its better piezoelectric response (5× compared to AlN), the improvement in acousto-optic modulation is still not very significant. For example, through AlScN film integration, [26] measured the V_πL to be 0.95 V·cm at 3.04 GHz.

An alternate approach to actuate SAW on the SOI, through the thermoelastic effect, has been demonstrated by [27, 28]. In this approach, as illustrated in figure 1.3(b), a modulated pump light emitted from the output facet of an optical fiber is directed onto a gold grating patterned on top of the SOI substrate. Absorption of the pump light induces periodic heating and cooling of the grating stripes, accompanied by thermal expansion and contraction. This results in a periodic strain pattern that is transferred into the underlying SOI substrate. When the frequency of the incident pump light matches with the resonance frequency, a SAW is launched perpendicular to the grating. The wavelength of the SAW is determined by the grating period, and the resonance frequency is determined by the grating period (wavelength) and the substrate property. In [27], the index modulation Δn was reported to be 1.2x10^{-6} with an average 500 mW optical pump power at 2.45 GHz.

The thermo-elastic approach obviates the need for piezoelectric material integration and provides a small footprint. However, requiring an additional high-power optical pump and a fiber alignment to a particular region on the chip creates cost and packaging issues. On the other hand, the piezoelectric approach is more pragmatic and energy efficient. Nonetheless, in addition to the material integration, the return loss of the input RF signal from the IDT due to the impedance mismatch between the source and the IDT could also be a concern. This is often solved by designing the IDT of a suitable impedance or adding a matching network to the IDT [29].

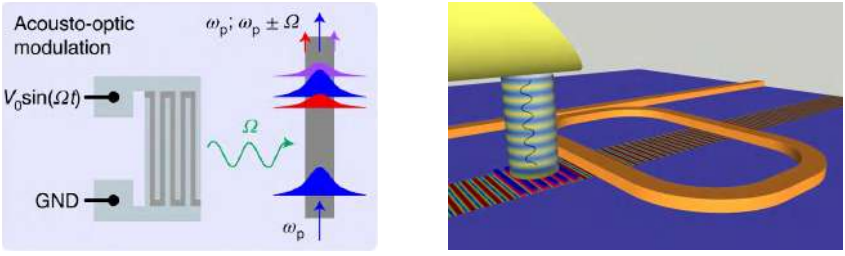

Figure 1.3: SAW actuation with (a) piezoelectric effect (b) thermo-elastic effect.

1.1.2 Piezoelectric MEMS actuation

Si PICs demand efficient tuning mechanisms to compensate for variations in the fabrication process and environmental perturbations, particularly to make re-configurable devices. As Si PICs hold potential as platforms for programmable photonics and neuromorphic computing, which rely on a large network of tunable phase shifters and couplers [30, 31]. Figure 1.4 compares the common tuning mechanisms in Si PICs. The most widely used tuning techniques in Si PICs are thermo-optic and plasma-dispersion-based tuning. However, they pose a bottleneck due to their limited speed, large footprint, or high energy consumption. Thermo-optic-based tuning typically requires 1-10 mW for a 2π phase shift and has a maximum speed of up to a few kHz. Additionally, the thermal cross-talk between the heating elements limits the compactness of the device [32]. On the other hand, plasma-dispersion-based tuning offers bandwidths up to several GHz. However, it introduces significant optical loss due to the injection of charge carriers into the waveguide [33]. The electro-optic effect-based modulator requires a long interaction length, increasing the device footprint.

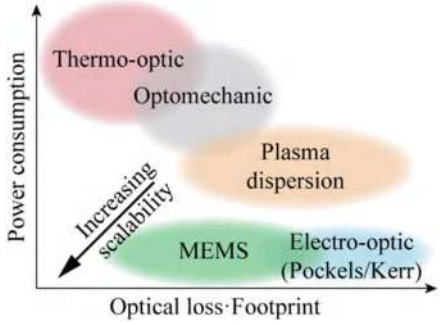

Figure 1.4: Comparison of optical tuning mechanisms [34].

As an alternative, micro-electro-mechanical system (MEMS) based tuning mechanisms have emerged as a promising option to achieve large-scale PIC tuning owing to their low power consumption ($\sim$ μW), low optical loss, and small footprint [35]. MEMS-based photonic devices primarily rely on electrostatic and piezoelectric actuation.

Figure 1.5 illustrates two main configurations of the electrostatic MEMS, where attractive forces between the charged plates drive the actuators. In figure 1.5(a), a low-doped Si waveguide and another low-doped tuning coupler are employed as a parallel-plate actuator. The drawback of this design is that doping in the Si waveguide introduces an additional optical loss. Figure 1.5(b) illustrates how this problem is countered by designing a set of parallel plate actuators in a comb-drive fashion. This comb-drive actuator is connected to a movable (tuning) coupler.

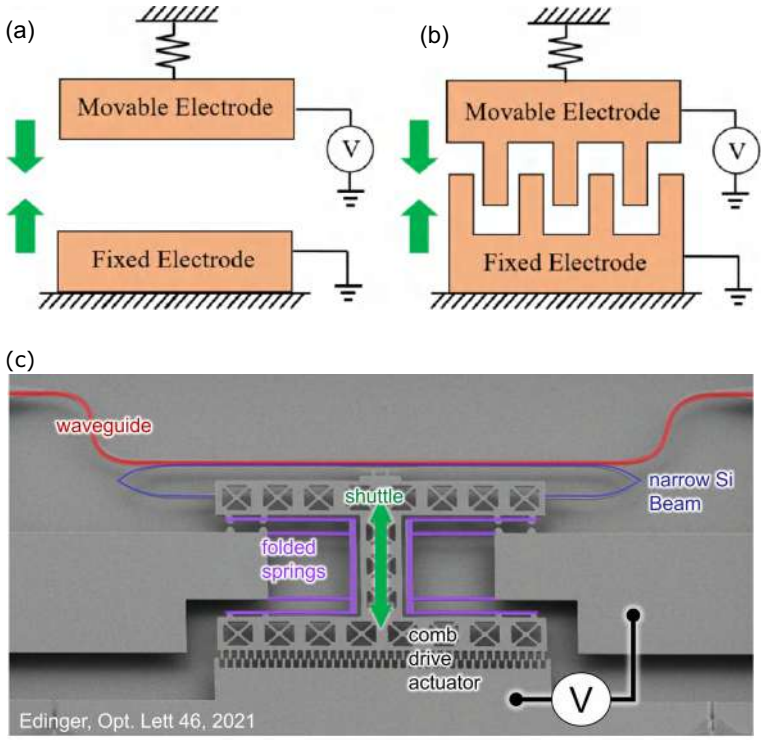

Figure 1.5: (a) Electrostatic MEMS driving with parallel plate actuator, (b) MEMS driving with a comb-drive actuator, (c) an SEM image of a tunable phase-shifter with a comb-drive actuator.

The drawback of this design is the large footprint and a higher risk of device collapse during the undercut process. Additionally, electrostatic actuators have a high risk of pull-in while driving, and their inherent large capacitance for driving increases the RC time constant, limiting their bandwidth ($\sim$ MHz). For instance, figure 1.5(c) shows a scanning electron microscope (SEM) image of an electrostatic MEMS-based tunable phase shifter implemented in an SOI platform [36]. In this device, a narrow Si beam (of length 50 μm) is driven with a comb-drive actuator, which tunes the optical field in the adjacent waveguide. With static driving (using a DC signal), the voltage required for a π-phase shift (V_π) was estimated to be 10.7 V. The frequency response measurement indicated the device operation bandwidth up to 1.03 MHz.

In contrast, piezoelectric actuation generates the driving force through induced stress or strain in the piezoelectric material under an applied electric field [34]. Nevertheless, the integration of piezoelectric materials on PICs poses compatibility-related challenges, and these materials tend to suffer from mechanical fatigue after

several cycles of driving [37, 38]. Besides, polycrystalline piezoelectric materials rely on a poling process (discussed in the next section) to perform well.

Hence, the seamless integration of a robust piezoelectric material into Si PICs holds the potential of low-power tuning but poses several challenges.

1.2 PZT film integration as a new frontier

Various piezoelectric thin films, including aluminum nitride (AlN) [39], lithium niobate ($LiNbO_3$) [40], and zinc oxide (ZnO) [41], have been successfully integrated into Si photonics. However, these materials exhibit a much weaker piezoelectric response than lead zirconate titanate (PZT). This difference is evident in their longitudinal piezoelectric constants (d_{33}) measured in bulk, as presented in table 1.1.

	ZnO	AlN	PZT	$LiNbO_3$ 128° cut
Density 10^3 (kg/m^3)	5.61-5.72	3.25-3.3	7.57	4.64
Young's modulus (GPa)	110-140	300-350	61	130-170
Longitudinal acoustic velocity (m/s)	6336	10,150-11,050	4500	3680-3980
Piezo-constant d_{33} (pm/V)	12	4.5-6.4	289-380	12
Effective coupling coefficient k^2 (%)	1.5-1.7	3.1-8	20-35	5-11.3

Table 1.1: Properties of common piezoelectric materials integrated on SOI [42].

PZT (chemical formula $PbZr_xTi_{1-x}O_3$, $0 \leq x \leq 1$) is one of the most widely used piezoelectric ceramic materials due to its strong piezoelectricity, high electromechanical coupling, common availability, and high-temperature compatibility (Curie point $\sim 370°C$) [43–45]. It belongs to the "piezoelectric ceramics," a subset of ferroelectric materials[2] (see figure 1.6), which are polycrystalline and usually have a strong piezoelectric effect. Below its Curie temperature, the crystal structure of PZT is tetragonal, as illustrated in figure 1.7(a). It exhibits spontaneous electrical polarization due to its ferroelectric nature. Above the Curie temperature, the crystal structure transforms into a centrosymmetric cubic phase, losing its ferroelectric and piezoelectricity.

Since PZT is a polycrystalline ceramic, its macroscopic behavior is determined by the net polarization of its domains. The domains within different grains of a piezoelectric ceramic can have different polarization (electric dipole orientation),

[2]Other examples of piezoelectric ceramics: lead titanate and strontium titanate

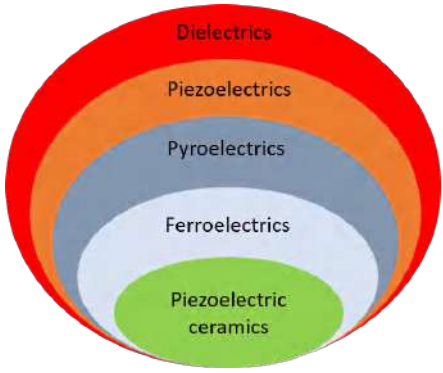

Figure 1.6: Hierarchical categorization of the dielectric subgroups.

as shown in figure 1.7(b). If the domains are randomly oriented, the net polarization of the material is zero. To induce a macroscopic polarization and align the domains in a specific direction, the material needs to undergo a process called "poling," as illustrated in 1.7(c). Poling involves applying a strong external electric field to reorient the dipoles in a concerted manner. This aligns the domains and creates a net polarization in the direction of the applied field. After the poling process, the ferroelectric material may exhibit a non-zero remanent polarization, meaning that even after removing the external field, some of the dipoles remain aligned in the poling direction. This remanent polarization characterizes the ferroelectric hysteresis loop, which is a key feature of ferroelectric materials. Figure 1.8 compares a typical hysteresis loop between a strong ferroelectric material such as PZT and a weaker ferroelectric material such as barium titanate (BTO) [46]. Due to its high remanent polarization, PZT is widely used in applications where stable and switchable polarization states are essential, such as in non-volatile memory devices and transducers [8].

Integrating a highly textured PZT thin film on SOI could be a promising route to realize novel functionalities. However, PZT thin films have traditionally been grown using a Pt seed layer, making them incompatible with photonic technology due to the high optical loss [47]. Although PZT films sandwiched between two Pt electrodes have been successfully used to obtain stress-optic phase modulation [48], the modulation speed was limited to about 5 kHz. In [49], a PZT film was sputter-deposited on a Si PIC using a MgO buffer layer. Nevertheless, this method remains challenging due to the complexity of precisely controlling film thickness and material composition. This challenge is exacerbated by the need for dedicated equipment and process lines, adding to the overall cost.

Recently, a novel approach for integrating highly textured PZT-films has been developed, using an ultrathin and transparent lanthanide-based buffer layer de-

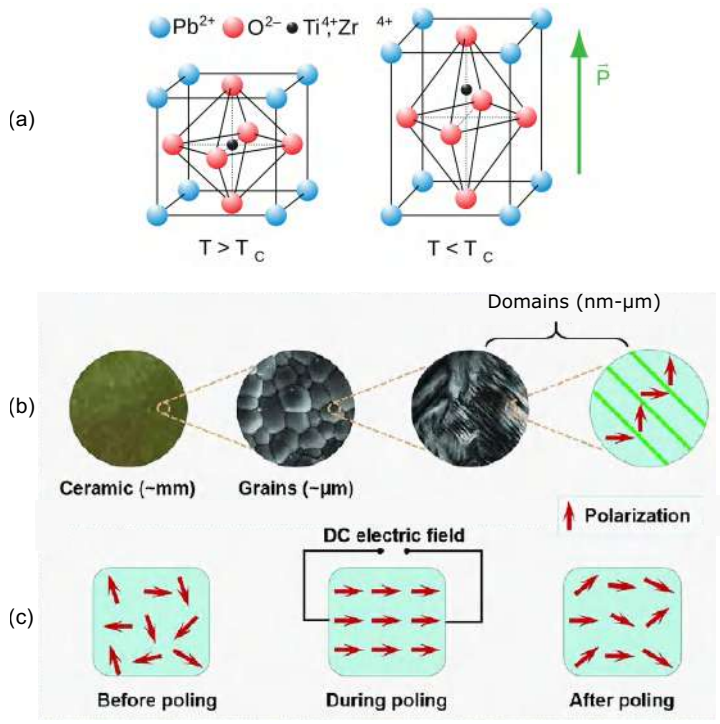

Figure 1.7: (a) PZT unit cell structure above and below Curie temperature T_C (image source: Wikipedia), (b) grains and domains with different electric dipole orientation in a piezoelectric ceramic, (c) poling process to align the domain polarization.

posited through chemical solution deposition (CSD), a cost-effective method [50, 51]. Figure 1.9(a) presents a scanning transmission electron microscope (STEM) image[3] of a PZT thin film deposited on a SiO_2 layer using $\sim$ 10 nm thick $La_2O_2CO_3$ buffer layer. This PZT film was integrated with a silicon nitride (SiN) ring resonator, as shown in figure 1.9(b), to achieve electro-optic modulation. The electric field applied over the PZT film changes its refractive index due to Pockel's effect. When a voltage is applied to the coplanar electrodes deposited on PZT/SiN, as shown in figure 1.9(c), the light signal propagating into the PZT layer gets modulated. This is observed as a shift in the transmission spectrum of the device, as presented in figure 1.9(d). The high quality of this PZT film was showcased through the demonstration of a low propagation loss ($<$ 1dB/cm) in a hybrid PZT/SiN waveguide, a strong effective Pockels coefficient (67 pm/V), and the modulation bandwidth beyond 33 GHz [52].

Additionally, we also demonstrated that this film exhibits a strong second-order

[3] STEM imaging was done by Hannes Rijckaert from the SCRiPTS group

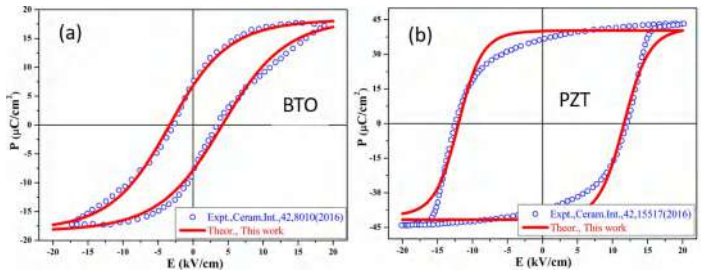

Figure 1.8: Ferroelectric hysteresis loop of (a) BTO (b) PZT [46].

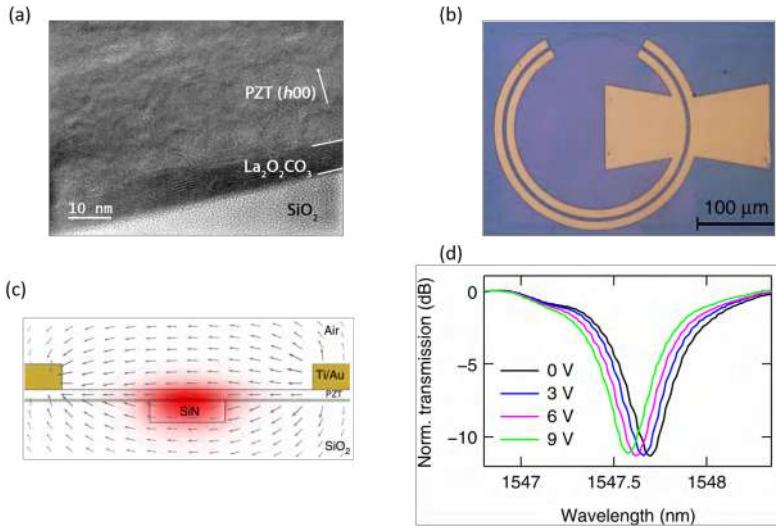

Figure 1.9: (a) Cross-section image with STEM showing a PZT layer deposited on $La_2O_2CO_3$ buffer layer on top of a SiO_2 layer, (b) an optical image of a PZT integrated on SIN ring resonator, (c) cross-section of the modulator showing the electric field distribution (depicted with arrows), (d) shift in the transmission spectrum from the applied voltage to the PZT-based Pockel's modulator.

nonlinearity ($\chi^2_{zzz} \sim 128$ pm/V) through second harmonic generation [53]. Therefore, a detailed investigation of the piezoelectric actuation with this PZT film is warranted [54–56].

1.3 Objectives and thesis structure

This thesis aims to investigate the piezoelectric actuation property of our PZT thin film, particularly for SAW and MEMS driving. These mechanisms are further exploited to control and manipulate how light propagates in Si PIC. The subsequent

chapters of this thesis are structured to provide an understanding of the complexity pertaining to the PZT-based device fabrication, characterization of the piezoelectric property, and ensuing light modulation from the PZT thin film integrated into Si PICs.

Chapter 2 describes the process optimization for the PZT film to achieve photonic MEMS devices. Chapter 3 presents the piezoelectric characterization of the PZT film through surface acoustic wave actuation and acousto-optic modulation in the Si waveguide. Chapter 4 deals with characterizing the piezoelectric actuation of suspended PZT-MEMS devices and the transfer-printing of the PZT coupons. Chapter 5 extends the study of the suspended PZT on Si devices to harness enhanced electro-optomechanical coupling. Finally, Chapter 6 concludes all the results and discusses the prospect of the PZT film integration for various applications.

1.4 Publications and awards

1.4.1 Publications in international journals

1. I. Ansari, G. F. Feutmba, J. P. George, Jeroen Beeckman, D. Van Thourhout, "Piezoelectrically driven Fano resonance in Silicon photonics" *arXiv*, vol. x, no. y, pp., 2023 [to be submitted].

2. I. Ansari, J. George, G.F Feutmba, Tessa VDV, A. Pandey, Jeroen Beeckman, D. Van Thourhout, "Light modulation in Silicon photonics by PZT actuated acoustic waves", *ACS Photonics*, vol. 9, no. 6, pp. 1944 –1953, 2022.

1.4.2 Publications in international conferences

1. I. Ansari, K. De Geest , J. De Witte , T. Vandekerckhove, H. Rijkaert, E. Picavet, E. Lievens, G. F. Feutmba, T. Van de Veire, B. Kuyken, J. Beeckman, D. Van Thourhout, "PZT micro-transfer printing for photonic MEMS", *IEEE Photonics Conference*, United States, TuE3.4, 2023 [accepted]

2. I. Ansari, J. Beeckman, D. Van Thourhout, " PZT based acoustic resonator for the refractive index modulation", *IEEE- Workshop on Recent advances in Photonics*, India, pp. 1–2, 2022

3. I. Ansari, E. Dieussaert, J. George, G.F Feutmba, J. Beeckman, D. Van Thourhout, " PZT based actuator for an efficient electro-optomechanical in-

teraction in Si-photonic integrated circuit", *SPIE Photonics West*, United States, p.12004–67

4. I. Ansari, D. V. Thourhout, J. P. George, G. F. Feutmba and J. Beeckman, "Acousto-optic modulation in a Si-waveguide", *IEEE 17th International Conference on Group IV Photonics*, pp. 1–2, 2021

5. I. Ansari, E. Dieussaert, J. George, G.F Feutmba, J. Beeckman, D. Van Thourhout, "PZT based MEMS actuators for photonic integration", *Annual Symposium of the IEEE Photonics Society Benelux Chapter*, Belgium, 2021.

6. I. Ansari, T. Van de Veire, J. George, G.F Feutmba, J. Beeckman, D. Van Thourhout, "Si-photonic integrated PZT thin film for acousto-optic modulation", *Conference on Lasers and Electro-Optics, United States*, p.JTh2B.24, 2020

7. I. Ansari, T. Van de Veire, J. George, G.F Feutmba, J. Beeckman, D. Van Thourhout, "Piezoelectric characterization of Si-photonic integrated PZT thin film", *Annual Symposium of the IEEE Photonics Society Benelux Chapter*, Netherlands, 2019

1.4.3 Awards

- IEEE Photonics Student & Young Professionals (SYP) grant to attend IPC-2023 at Orlando (US)
- Silver award at Huawei PhD student contest, Silicon Photonics edition-2022. Presented paper "Light modulation in Si Photonics by PZT actuated acoustic waves"
- Optica Student Leadership Conference (SLC) grant to attend FiO-2022 at Rochester (US)

References

[1] Graham T Reed and Andrew P Knights. *Silicon photonics: an introduction*. John Wiley & Sons, 2004.

[2] W. Bogaerts, R. Baets, P. Dumon, V. Wiaux, S. Beckx, D. Taillaert, B. Luyssaert, J. Van Campenhout, P. Bienstman, and D. Van Thourhout. *Nanophotonic waveguides in silicon-on-insulator fabricated with CMOS technology*. Journal of Lightwave Technology, 23(1):401–412, 2005.

[3] Bahram Jalali and Sasan Fathpour. *Silicon Photonics*. Journal of Lightwave Technology, 24(12):4600–4615, 2006.

[4] Chi Xiong, Wolfram HP Pernice, and Hong X Tang. *Low-loss, silicon integrated, aluminum nitride photonic circuits and their use for electro-optic signal processing*. Nano letters, 12(7):3562–3568, 2012.

[5] Dan-Xia Xu, Jens H Schmid, Graham T Reed, Goran Z Mashanovich, David J Thomson, Milos Nedeljkovic, Xia Chen, Dries Van Thourhout, Shahram Keyvaninia, and Shankar K Selvaraja. *Silicon photonic integration platform—have we found the sweet spot?* IEEE Journal of Selected Topics in Quantum Electronics, 20(4):189–205, 2014.

[6] Lukas Chrostowski and Michael Hochberg. *Silicon photonics design: from devices to systems*. Cambridge University Press, 2015.

[7] Gustav Gautschi and Gustav Gautschi. *Background of piezoelectric sensors*. Springer, 2002.

[8] Zenghui Liu, Hua Wu, Wei Ren, and Zuo-Guang Ye. *4.05 - Piezoelectric and ferroelectric materials: Fundamentals, recent progress, and applications*. In Jan Reedijk and Kenneth R. Poeppelmeier, editors, Comprehensive Inorganic Chemistry III (Third Edition), pages 135–171. Elsevier, Oxford, third edition edition, 2023.

[9] Lutong Cai, Ashraf Mahmoud, and Gianluca Piazza. *Low-loss waveguides on Y-cut thin film lithium niobate: towards acousto-optic applications*. Opt. Express, 27(7):9794–9802, Apr 2019.

[10] Linbo Shao, Mengjie Yu, Smarak Maity, Neil Sinclair, Lu Zheng, Cleaven Chia, Amirhassan Shams-Ansari, Cheng Wang, Mian Zhang, Keji Lai, and Marko Lončar. *Microwave-to-optical conversion using lithium niobate thin-film acoustic resonators*. Optica, 6(12):1498–1505, Dec 2019.

[11] Christopher J. Sarabalis, Timothy P. McKenna, Rishi N. Patel, Raphaël Van Laer, and Amir H. Safavi-Naeini. *Acousto-optic modulation in lithium niobate on sapphire*. APL Photonics, 5(8):086104, 2020.

[12] Ahmed E. Hassanien, Steffen Link, Yansong Yang, Edmond Chow, Lynford L. Goddard, and Songbin Gong. *Efficient and wideband acousto-optic modulation on thin-film lithium niobate for microwave-to-photonic conversion*. Photon. Res., 9(7):1182–1190, Jul 2021.

[13] Zejie Yu and Xiankai Sun. *Gigahertz Acousto-Optic Modulation and Frequency Shifting on Etchless Lithium Niobate Integrated Platform*. ACS Photonics, 8(3):798–803, 2021.

[14] M. M. de Lima, M. Beck, R. Hey, and P. V. Santos. *Compact Mach-Zehnder acousto-optic modulator*. Applied Physics Letters, 89(12):121104, 2006.

[15] M. Beck, M. M. de Lima, E. Wiebicke, W. Seidel, R. Hey, and P. V. Santos. *Acousto-optical multiple interference switches*. Applied Physics Letters, 91(6):061118, 2007.

[16] Krishna C. Balram, Marcelo I. Davanço, B. Robert Ilic, Ji-Hoon Kyhm, Jin Dong Song, and Kartik Srinivasan. *Acousto-Optic Modulation and Optoacoustic Gating in Piezo-Optomechanical Circuits*. Phys. Rev. Applied, 7:024008, Feb 2017.

[17] Stephan Kapfinger, Thorsten Reichert, Stefan Lichtmannecker, Kai Müller, Jonathan J Finley, Achim Wixforth, Michael Kaniber, and Hubert J Krenner. *Dynamic acousto-optic control of a strongly coupled photonic molecule*. Nature communications, 6(1):1–6, 2015.

[18] B. Sun, A. Kar-Roy, and C. S. Tsai. *Guided-Wave Acousto-Optic Bragg Diffractions in InP/InGaAsP/InP Waveguide*. In Integrated Photonics Research, page IThG15. Optical Society of America, 1995.

[19] K. Makles, T. Antoni, A. G. Kuhn, S. Deléglise, T. Briant, P.-F. Cohadon, R. Braive, G. Beaudoin, L. Pinard, C. Michel, V. Dolique, R. Flaminio, G. Cagnoli, I. Robert-Philip, and A. Heidmann. *2D photonic-crystal optomechanical nanoresonator*. Opt. Lett., 40(2):174–177, Jan 2015.

[20] Lord Rayleigh. *On Waves Propagated along the Plane Surface of an Elastic Solid*. Proceedings of the London Mathematical Society, s1-17(1):4–11, 1885.

[21] R.F. Milsom, N.H.C. Reilly, and M. Redwood. *Analysis of Generation and Detection of Surface and Bulk Acoustic Waves by Interdigital Transducers*. IEEE Transactions on Sonics and Ultrasonics, 24(3):147–166, 1977.

[22] A.J. Slobodnik. *Surface acoustic waves and SAW materials*. Proceedings of the IEEE, 64(5):581–595, 1976.

[23] Liang Lei, Bo Dong, Yuxuan Hu, Yisong Lei, Zhizhong Wang, and Shuangchen Ruan. *High-Frequency Surface Acoustic Wave Resonator with Diamond/AlN/IDT/AlN/Diamond Multilayer Structure*. Sensors, 22(17), 2022.

[24] Robert W Boyd. *Nonlinear optics*. Academic press, 2020.

[25] Eric A. Kittlaus, William M. Jones, Peter T. Rakich, Nils T. Otterstrom, Richard E. Muller, and Mina Rais-Zadeh. *Electrically driven acousto-optics and broadband non-reciprocity in silicon photonics*. Nature Photonics, 15:43–52, 1 2021.

[26] Chukun Huang, Haotian Shi, Linfeng Yu, Kang Wang, Ming Cheng, Qiang Huang, Wenting Jiao, and Junqiang Sun. *Acousto-optic modulation in silicon waveguides based on piezoelectric aluminum scandium nitride film*. Advanced Optical Materials, 10(6):2102334, 2022.

[27] Dvir Munk, Moshe Katzman, Mirit Hen, Maayan Priel, Moshe Feldberg, Tali Sharabani, Shahar Levy, Arik Bergman, and Avi Zadok. *Surface acoustic wave photonic devices in silicon on insulator*. Nature Communications, 10(1):4214, dec 2019.

[28] Moshe Katzman, Dvir Munk, Maayan Priel, Etai Grunwald, Mirit Hen, Naor Inbar, Moshe Feldberg, Tali Sharabani, Roy Zektzer, Gil Bashan, Menachem Vofsi, Uriel Levy, and Avi Zadok. *Surface acoustic microwave photonic filters in standard silicon-on-insulator*. Optica, 8(5):697–707, May 2021.

[29] J. Kirschner. *Surface Acoustic Wave Sensors: Design for Application*. 2010.

[30] Daniel Pérez, Ivana Gasulla, Lee Crudgington, David J Thomson, Ali Z Khokhar, Ke Li, Wei Cao, Goran Z Mashanovich, and José Capmany. *Multipurpose silicon photonics signal processor core*. Nature communications, 8(1):636, 2017.

[31] Alexander N Tait, Thomas Ferreira De Lima, Ellen Zhou, Allie X Wu, Mitchell A Nahmias, Bhavin J Shastri, and Paul R Prucnal. *Neuromorphic photonic networks using silicon photonic weight banks*. Scientific reports, 7(1):7430, 2017.

[32] HH Li. *Refractive index of silicon and germanium and its wavelength and temperature derivatives*. Journal of Physical and Chemical Reference Data, 9(3):561–658, 1980.

[33] RICHARDA Soref and BRIANR Bennett. *Electrooptical effects in silicon*. IEEE journal of quantum electronics, 23(1):123–129, 1987.

[34] Carlos Errando-Herranz, Alain Yuji Takabayashi, Pierre Edinger, Hamed Sattari, Kristinn B. Gylfason, and Niels Quack. *MEMS for Photonic Integrated Circuits*. IEEE Journal of Selected Topics in Quantum Electronics, 26(2):1–16, 2020.

[35] Carlos Errando-Herranz, Frank Niklaus, Göran Stemme, and Kristinn B Gylfason. *Low-power microelectromechanically tunable silicon photonic ring resonator add-drop filter*. Optics letters, 40(15):3556–3559, 2015.

[36] Pierre Edinger, Alain Yuji Takabayashi, Carlos Errando-Herranz, Umar Khan, Hamed Sattari, Peter Verheyen, Wim Bogaerts, Niels Quack, and Kristinn B. Gylfason. *Silicon photonic microelectromechanical phase shifters for scalable programmable photonics*. Opt. Lett., 46(22):5671–5674, Nov 2021.

[37] Andrea Mazzalai, Davide Balma, Nachiappan Chidambaram, Ramin Matloub, and Paul Muralt. *Characterization and fatigue of the converse piezoelectric effect in PZT films for MEMS applications*. Journal of Microelectromechanical systems, 24(4):831–838, 2014.

[38] RR Benoit, RQ Rudy, JS Pulskamp, RG Polcawich, and SS Bedair. *Advances in piezoelectric PZT-based RF MEMS components and systems*. Journal of Micromechanics and Microengineering, 27(8):083002, 2017.

[39] Chi Xiong, Wolfram H P Pernice, Xiankai Sun, Carsten Schuck, King Y Fong, and Hong X Tang. *Aluminum nitride as a new material for chip-scale optomechanics and nonlinear optics*. New Journal of Physics, 14(9):095014, sep 2012.

[40] Payam Rabiei, Jichi Ma, Saeed Khan, Jeff Chiles, and Sasan Fathpour. *Heterogeneous lithium niobate photonics on silicon substrates*. Optics express, 21(21):25573–25581, 2013.

[41] Nebiyu A Yebo, Petra Lommens, Zeger Hens, and Roel Baets. *An integrated optic ethanol vapor sensor based on a silicon-on-insulator microring resonator coated with a porous ZnO film*. Optics Express, 18(11):11859–11866, 2010.

[42] Y.Q. Fu, J.K. Luo, N.T. Nguyen, A.J. Walton, A.J. Flewitt, X.T Zu, Y. Li, G. McHale, A. Matthews, E. Iborra, H. Du, and W.I. Milne. *Advances in piezoelectric thin films for acoustic biosensors, acoustofluidics and lab-on-chip applications*. Progress in Materials Science, 89:31–91, 2017.

[43] B. A. Auld. *Acoustic fields and waves in solids*. https://books.google.be/books?id=q_9rJYpgjZ0C&lpg=PP1&dq=Elastic%20Waves%20in%20Solids%20II&pg=PP1#v=onepage&q&f=false.

[44] Mohsen Safaei, Henry A Sodano, and Steven R Anton. *A review of energy harvesting using piezoelectric materials: state-of-the-art a decade later (2008–2018)*. Smart Materials and Structures, 28(11):113001, oct 2019.

[45] HANS JAFFE. *Piezoelectric Ceramics*. Journal of the American Ceramic Society, 41(11):494–498.

[46] Zhi Ma, Yanan Ma, Zhipeng Chen, Fu Zheng, Hua Gao, Hongfei Liu, and Huanming Chen. *Modeling of hysteresis loop and its applications in ferroelectric materials*. Ceramics International, 44(4):4338–4343, 2018.

[47] N. Izyumskaya, Y.-I. Alivov, S.-J. Cho, H. Morkoç, H. Lee, and Y.-S. Kang. *Processing, Structure, Properties, and Applications of PZT Thin Films*. Critical Reviews in Solid State and Materials Sciences, 32(3-4):111–202, 2007.

[48] Naser Hosseini, Ronald Dekker, Marcel Hoekman, Matthijn Dekkers, Jan Bos, Arne Leinse, and Rene Heideman. *Stress-optic modulator in TriPleX platform using a piezoelectric lead zirconate titanate (PZT) thin film*. Opt. Express, 23(11):14018–14026, Jun 2015.

[49] Suraj Singh and Shankar Kumar Selvaraja. *Sputter-deposited PZT-on-Silicon electro-optic modulator*. In 2021 IEEE Photonics Conference (IPC), pages 1–2. IEEE, 2021.

[50] J. P. George, P. F. Smet, J. Botterman, V. Bliznuk, W. Woestenborghs, D. Van Thourhout, K. Neyts, and J. Beeckman. *Lanthanide-Assisted Deposition of Strongly Electro-optic PZT Thin Films on Silicon: Toward Integrated Active Nanophotonic Devices*. ACS Applied Materials & Interfaces, 7(24):13350–13359, jun 2015.

[51] Ewout Picavet, Hannes Rijckaert, Eduardo Solano, Oier Bikondoa, Edgar Gutierrez Fernandez, Petriina Paturi, Laura Van Bossele, Henk Vrielinck, Jeroen Beeckman, and Klaartje De Buysser. *The self out-of-plane oriented $La_2O_2CO_3$ film: an integration tool for fiber textured ferroelectric thin films*. Journal of Materials Chemistry C, 11(23):7705–7713, 2023.

[52] Koen Alexander, John P. George, Jochem Verbist, Kristiaan Neyts, Bart Kuyken, Dries Van Thourhout, and Jeroen Beeckman. *Nanophotonic Pockels modulators on a silicon nitride platform*. Nature Communications, 9(1):4–9, 2018.

[53] Gilles F. Feutmba, Artur Hermans, John P. George, Hannes Rijckaert, Irfan Ansari, Dries Van Thourhout, and Jeroen Beeckman. *Reversible and Tunable Second-Order Nonlinear Optical Susceptibility in PZT Thin Films for Integrated Optics*. Advanced Optical Materials, n/a(n/a):2100149.

[54] Irfan Ansari, Tessa Van de Veire, John P. George, Gilles.F. Feutmba, Jeroen Beeckman, and Dries Van Thourhout. *Si-photonic integrated PZT thin film for acousto-optic modulation*. In Conference on Lasers and Electro-Optics, page JTh2B.24. Optical Society of America, 2020.

[55] Peter J. M. van der Slot, Marco A. G. Porcel, and Klaus-J. Boller. *Surface acoustic waves for acousto-optic modulation in buried silicon nitride waveguides*. Opt. Express, 27(2):1433–1452, Jan 2019.

[56] Irfan Ansari, Dries Van Thourhout, John P. George, Gilles F. Feutmba, and Jeroen Beeckman. *Acousto-optic modulation in a Si-waveguide*. In 2021 IEEE 17th International Conference on Group IV Photonics (GFP), pages 1–2, 2021.

2

Fabrication and process optimization

Although the deposition method of our PZT film was extensively optimized [1, 2], further processing of this film was relatively unexplored. For example, to pattern the PZT film, it was etched using an inductively coupled plasma (ICP) tool with Ar and SF_6 reactive gases. But the etch recipe was not optimized. That resulted in a slow PZT etch rate and poor selectivity against the photoresist (PR) mask, making it impossible to pattern a thicker PZT film. Moreover, the previously employed ICP tool was subsequently repurposed exclusively for etching III-V materials. As for the remaining etching tool, a reactive ion etching (RIE) tool, a new set of parameters and recipes needed to be developed. Also, it was unknown how the PZT film reacts with common reactants like hydrogen fluoride (HF) and buffered hydrogen fluoride (BHF) solutions used for under-etching a SiO_2 sacrificial layer. Additionally, the selection of an appropriate stop material to safeguard sensitive components during this process required thorough investigation. These were important questions to be examined to achieve a PZT based micro-electromechanical system (MEMS) for photonics application. This led to the optimization of a full process flow, as shown in fig 2.1. The main challenges were the following:

1. Patterning of the PZT layer: since our PZT film is annealed at a very high temperature (600-800°C), it is chemically resistant and difficult to etch with standard etch recipes. Besides, the byproducts of PZT dry etching exhibit a high risk of contaminating the etching chamber, which limits the tool options in our (UGent) cleanroom. For these reasons, a suitable etching recipe was developed using a reactive-ion etching (RIE) tool, the only ”allowed” tool

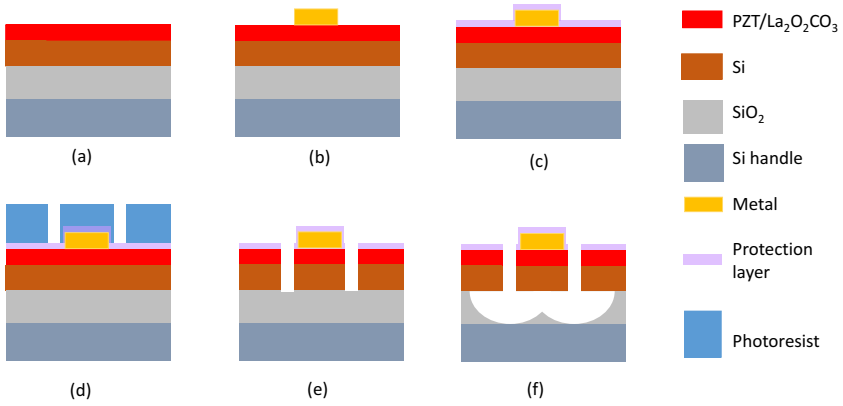

Figure 2.1: Fabrication steps for a typical PZT-MEMS actuator. (a) PZT deposition on the planarized device (b) patterning and metallization of the electrodes (c) deposition of a protection layer (d) photoresist mask patterning (e) dry etch to open the under-etch window (f) HF/BHF exposure to under-etch the sacrificial BOX layer.

for PZT etching.

2. Under-etching: an appropriate etchant had to be determined (aqueous HF and BHF, vapor HF) that can give sufficient yield and a good selectivity against the protection mask.

3. Protection mask against HF/BHF etchant: we needed to use HF/BHF for under-etching the sacrificial buried-oxide (BOX) in SOI. But the aggressive nature of these reactants requires a suitable protection scheme to protect the sensitive components on the chip during the under-etching process.

2.1 PZT film deposition

Our in-house fabrication starts with the PZT film deposition process [1], which relies on a CSD method involving four steps. Since this method involves spin-coating of the precursor solutions, the substrate surface has to be flat or planarized for uniform film deposition. [2]

[1] PZT film deposition in this work was mainly carried out by John P. George and Tessa V. De Veire, and later by Ewout Picavet and Kobe De Geest

[2] Planarization is the process of flattening and smoothing a surface by eliminating surface topologies and irregularities. The most common technique for planarizing a silicon-on-insulator (SOI) substrate is through oxide deposition, followed by chemical mechanical polishing (CMP) [3].

1. Preparation of a precursor solution
2. Spin-coating the precursor on a planarized substrate
3. Pyrolysis of organic compounds at 300-500°C to obtain an amorphous film
4. Annealing at an elevated temperature (600-800°C) under O_2 gas flow for crystallization

Before the PZT deposition, the substrate is cleaned with acetone and isopropyl alcohol (IPA), and dehydrated on a hotplate at 100-120°C for 3-5 minutes to evaporate any water or moisture. Subsequently, the sample is cleaned in O_2 plasma for about 10 minutes to get rid of any polymers or organic residues. Then, a lanthanide-based intermediate layer ($La_2O_2CO_3$) is deposited on a planarized substrate with CSD method. This intermediate layer acts as a barrier layer to prevent the lead (Pb) diffusion into the substrate and as a seed layer for a textured PZT growth. Subsequently, the PZT film is deposited with CSD method. In each cycle up to the pyrolysis step, the thickness of the deposited PZT film is around 50 nm. Hence, for a thicker PZT film, step 1 to step 3 is repeated until the desired thickness[3] is achieved. Finally, the PZT film is annealed in a tube furnace to let it crystallize. For more details about the PZT film deposition process, see the PhD thesis of John P. George [1].

2.2 Electrode pattering on the PZT film

For the electrode metallization atop the PZT film, an image-reversal photo-lithography, followed by a lift-off process, was employed. The UV exposure time and the development time of the UV-exposed photoresist were optimized to get a good patterning [4]. The "image reversal" contact lithography process steps were as follows:

1. Sample cleaning with acetone and IPA, followed by dehydration on a hotplate at 120°C for 3-5 minutes.
2. Spin-coating TI prime adhesive layer at 3000 rpm for 40s
3. Baking the sample on a hotplate at 120°C for 3 min
4. Spin-coating AZ 5214 at 3000 rpm for 40s
5. Baking the sample on a hotplate at 100°C for 3 min
6. Sample cooling down for $\sim$ 5 min

[3] This layer-by-layer deposition also introduces thickness dependency on the PZT properties [1, 4]
[4] UV exposure time optimization was led by Muhammad Muneeb

7. Ultra-violet (UV) exposure[5] for 11.5 sec in 'vacuum' mode
8. Post-baking at 120°C for 3 min
9. Flood-exposure on the sample for 52 sec
10. Developing the sample in AZ 400K: H_2O solution with volume ratio 1:3 for $\sim$ 50-52 sec
11. Soft-resist removal through O_2 plasma in RIE tool for 30 sec to ensure the fill removal of the patterned photoresist (measured PR thickness with the profilometer $\sim$ 1500 nm).

The photoresist patterned sample was then loaded in a metal evaporator for the metallization[6]. Finally, the metalized sample was merged into an acetone solution for the lift-off.

2.3 Al_2O_3 protection mask

PZT film can react with the typical etchants used for under-etching SiO_2. Figure 2.2 (a) and (b) illustrate the microscope images of the PZT films after they were exposed to BHF and HF vapor, respectively. we see that the BHF solution reacts quickly with the PZT layer, resulting in pitting corrosion on its surface. Hence, a protection mask is necessary for the PZT patterning with the BHF. On the other hand, when the sample is exposed to the HF vapor, it starts showing some corrosion after a relatively longer etch duration ($>\sim$ 25 min).

To protect the sensitive components and the PZT film during a long HF vapor exposure, an Al_2O_3 film can be used as a hard mask [5]. The use of a hard mask solves the 'peeling-off effect' (discussed later) in a photoresist mask, providing better protection against lateral etching. However, the hard mask layer stays on top of the suspended device. Nevertheless, given the low density and small thickness, the mass-loading effect from the remaining Al_2O_3 layer can be neglected for the electromechanical actuation of the device.

To test the Al_2O_3 protection capability, first, 300 nm SiO_2 film was deposited on an SOI substrate at $\sim$ 270°C with plasma-enhanced chemical vapor deposition (PECVD). Then, the SiO_2 layer was patterned with contact lithography using a photoresist mask, followed by RIE process. The sample was cleaned with acetone and isopropyl alcohol (IPA), and dehydrated on a hotplate at 120°C for 3-5 minutes. Subsequently, the sample was cleaned in O_2 plasma for about 10 minutes.

[5] In all our contact photo-lithography, i-line (365 nm) UV from a mercury gas-discharge lamp was used to expose the sample through a chrome-on-quartz photomask.

[6] metallization was done by Muhammad Muneeb and/or Steven Verstuyft

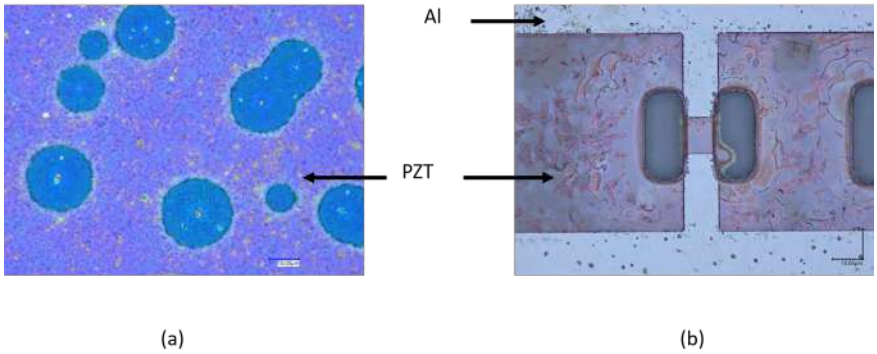

Figure 2.2: (a) PZT film after 12 min exposure with an etchant solution containing BHF and H_2O in 1:10 by volume, (b) PZT film after 90 min exposure to HF vapor.

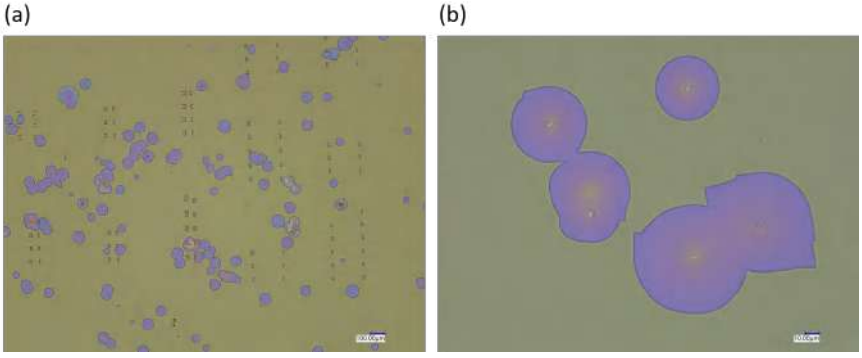

Figure 2.3: Microscope image after 30 min of HF vapor exposure on a sample containing 50 nm ALD deposited Al_2O_3 over 300 nm of PECVD SiO_x (patterned) on an SOI substrate. (a) area showing several etched SiO_x regions through the protection mask. (b) zoomed-in image shows pinhole centers of the etched regions

After that, a 50 nm thick Al_2O_3 film was deposited using atomic layer deposition (ALD)[7] on top of the substrate. ALD was performed at a high temperature (250 °C) with several cycles of deposition, giving a very high-density Al_2O_3 film, which makes it chemically resistant. On the contrary, PECVD deposited SiO_2 has a low density, so it can be very sensitive to the HF etching.

In fig 2.3, a microscope image of the sample after 30 min HF vapor exposure is shown. This shows several etch etch spots. On zooming in, we can see each of these etchings seemed to have taken place through some pinholes/contaminating particles. We noted that these spots appeared mainly in the patterned SiO_2 region, whereas away from the patterned regions, they were less present. This

[7] ALD was done by David Schaubroeck from the CMST group

suggested that the etching spots could have appeared due to the presence of the etching residues/particles from the SiO_2 patterning. As, the thinner/uneven Al_2O_3 deposited over these particles allows etchants to attack through them.

Now that we learned about the protection property of the Al_2O_3 mask, the next challenge was to pattern it. Al_2O_3 is chemically resistant even against the fluorine based reactant gases used in dry-etching. However, the wet-patterning of the Al_2O_3 mask was shown to be effective [6]. Hence, a series of tests was performed to pattern the Al_2O_3 film using wet etchants such as AZ400K, HF and BHF solutions. A hard-baked photoresist TI 35E was used as a patterning mask. The sample preparation was done in the following steps:

1. ALD deposition of 41 nm Al_2O_3 on a Si substrate
2. Sample cleaning with acetone and IPA. Dehydration followed by O_2 plasma exposure for 10 min.
3. Spin-coating the photoresist TI 35E at 3000 rpm for 40s
4. Baking the sample on a hotplate at 100°C for 3 min
5. Sample cooling down for $\sim$ 5 min
6. UV exposure for 70 sec in 'vacuum' mode
7. Wait for at least 10 min
8. Developing the sample in AZ 400K: H_2O solution with volume ratio 1:3 for $\sim$ 50 sec
9. Post-baking the sample at 120 °C on the hotplate.
10. Soft-resist removal in RIE tool for 2-4 min to ensure the fill removal of the patterned photoresist (measured resist thickness with the profilometer $\sim$ 3700 nm).
11. Flood exposure for 3-4 min to ensure further hardening of the photoresist.
12. Hard-baking the sample on a hotplate at $\sim$ 145°C. The sample was gradually cooled down to avoid cracks in the hard-baked photoresist layer.

After the sample preparation, it was cleaved into four pieces to test etching with 100% AZ400K, 25% AZ400K, 1% HF and 2% BHF solution. Each piece was dipped into an etchant solution for 2 min and then put into the deionized water to stop the etching process. After drying, the residual Al_2O_3 thickness was monitored

using a Filmetrics tool[8]. The results of these tests are summarized in the following table.

Etch method	Al_2O_3 thickness (nm) after 2 min etching	Observation
100% AZ400K	0	Too aggressive, PR and Al_2O_3 both gone
25% AZ400K	29.4, 28.5, 28.2, 29.5	still attacks the PR
1% HF	2.5, 9, 1.4, 1.2, 7.4	Better selectivity but uneven and aggressive etching
2% BHF	7.4, 7.5, 7.9, 6.5, 8	Better selectivity, uniform but fast etching

Table 2.1: Wet-patterning of Al_2O_3 film. Al_2O_3 thickness was measured at different locations on the sample after each etching step.

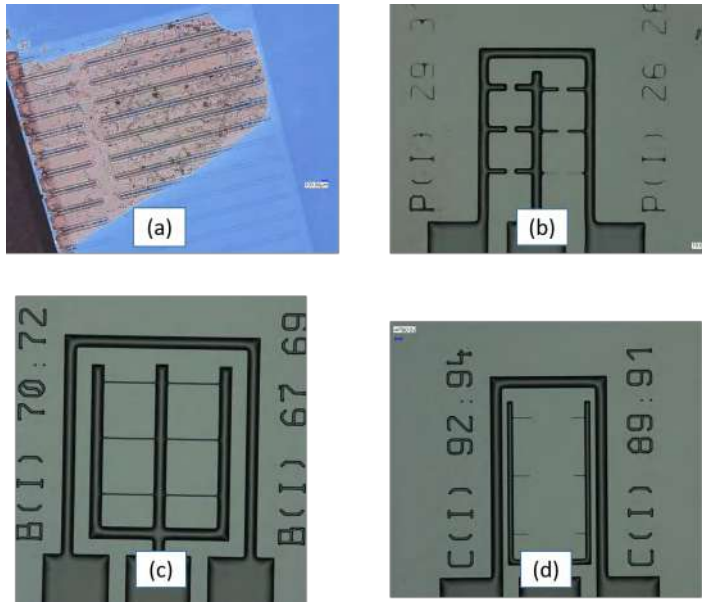

Figure 2.4: Optical images after 2 min exposure to the liquid etchants as described in table 2.1. (a) aggressive etching from 100 % AZ400K developer dissolves the hard-baked photoresist (b) 25 % AZ400K is still etching the photoresist (c) 1 % HF shows better selectivity against photoresist. However, after cleaning the photoresist, we can see uneven etching indicating leakage of HF through the photoresist (d) 2% BHF shows better selectivity and uniform etching such that even the smallest features survive.

We observe that 100% AZ400K attacks the photoresist and Al_2O_3 underneath

[8]Filmetrics is a tool to measure the film thickness based on its reflection of the light over a range of wavelength [7]

aggressively, whereas 25% AZ 400K still dissolves the photoresist mask (slowly). 1% HF showed better selective etching compared to AZ 400K, but the etched thickness was uneven and there was significant lateral etching. On the other hand, 2 % BHF gave the best etch selectivity and uniform etching.

time (min)	Al_2O_3 thickness (nm)	etch-rate (nm/min)
0	50	0
1	37	13
+1	29	8
+1	16	13
+1	7	9

Table 2.2: Wet-patterning of Al_2O_3 film with 1% BHF.

Now, in the next step, BHF was diluted to 1% to have more controlled (slower) etching. Another piece from the previously prepared sample as described above was used for testing. The sample was dipped into 1% BHF solution for 1 minute and then the residual Al_2O_3 thickness was measured with Filmetrics tool. This step was repeated until the Al_2O_3 thickness was negligible. The etch results are given in table 2.2. We found that the average etch rate of Al_2O_3 with 1% BHF is $\sim$ 11 nm/min.

2.4 PZT patterning optimization

During the deposition process, the PZT sample is annealed at a high temperature (between 600 to 800°C) to allow crystallization of the PZT film. Consequently, the PZT film gets very dense and resistant to the normal chemical etching process. Due to the slow etching of PZT, its selectivity against the patterning mask (photoresist) becomes very poor. Hence, we carried out etching tests with different combinations of the etchant gases and the input parameters (chamber pressure and RF power) of RIE.

To prepare the testing sample, $\sim$ 150 nm thick PZT film was deposited on a Si substrate. A thick photoresist (MicroChemicals TI 35E) mask was patterned on the sample using a positive photo-lithography process as follows:

1. Spin-coating TI 35E photoresist on the PZT/Si sample at 3000 rpm for 40s
2. Baking the sample on a hotplate at 100°C for 3 min
3. UV exposure for 70 s in 'vacuum' mode
4. Waiting for at least 10 min
5. Developing the sample in AZ400K: H_2O with 1:3

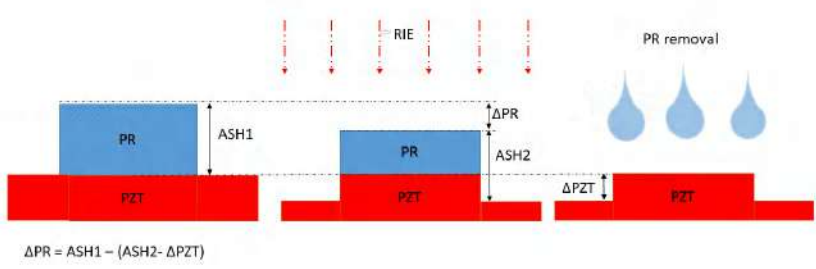

Figure 2.5: PZT film patterning step. (a) UV lithography to pattern the photoresist (b) etching of the PZT film in the RIE tool (c) cleaning the photoresist to obtain the patterned PZT film.

6. Hard baking the sample at 120°C for about 3 min

The prepared sample was cleaved into multiple pieces. Each piece was loaded in the RIE tool separately and etched with a different recipe. After a certain etching time, the photoresist was cleaned using acetone, and isopropyl alcohol (IPA), followed by an exposure in O_2 plasma to get rid of any residues. The thickness of the etched photoresist (ΔPR) and the PZT film (ΔPZT) were calculated based on the average slope height (ASH) measurement with a profilometer, before etching, after etching, and after removing the photoresist. These steps are illustrated in figure 2.5.

2.4.1 PZT etch trial 1: SF_6 with different RF power and chamber pressure

In the first trial, only SF_6 was used as the reactant gas with the flow rate of 20 sccm at 150 W of RF power and 20 mTorr chamber pressure.

time (min)	ΔPR (nm)	ΔPZT (nm)	PR etch-rate (nm/min)	PZT etch-rate (nm/min)	selectivity (PZT:PR)
15	1778	76	118	5	1:23.6
+10	1278	61	128	6	1:21.3
+5	474	13	95	2.6	1:36.5

Table 2.3: A summary of the average etched thickness estimated from the profilometer measurement. The test sample was 3613 nm thick hard-baked TI 35E photoresist on top of a 150 nm PZT film deposited on a Si substrate.

In table 2.3, the etching results of the PZT film with SF_6 are summarized. We

found that while PZT was etched very slowly, the photoresist mask got etched much faster, suggesting poor selectivity. This indicates that SF_6 alone is not ideal for etching the PZT film. Other parameters or/and reactant gases should be tested.

Power (W)	Pressure (mTorr)	ΔPZT (nm)	PZT etch-rate (nm/min)	selectivity (PZT:PR)
150	20	76	5	1:15.2
300	20	205	13.7	1:15
150	10	94	6.2	1:15.2

Table 2.4: PZT etch-rate (15 min etching) with RF power and chamber pressure.

Now with the same reactant gas (SF_6), we varied the RF power and the chamber pressure. The measured etch rates are shown in table 2.4. We observe that increasing the RF power results in a higher etch rate. This could be due to the higher concentration and energy of the etchant ions and radicals. Also, reducing the chamber pressure results in a slightly better etch rate, possibly because of a longer mean free path of the etchants. Therefore, for a good etch rate, we keep the RF power high and chamber pressure low. Next, we tried mixing different etchant gases.

2.4.2 PZT etch trial 2: SF_6 mixture with Ar and O_2

For the first trial with more complex gas mixtures, Ar was introduced to allow more physical etching through Ar^+, and a small amount of O_2 gas was also added to help clean up the byproducts through O_2 plasma formation.

SF_6 (sccm)	Ar (sccm)	O_2 (sccm)	PR etch-rate (nm/min)	PZT etch-rate (nm/min)	selectivity (PZT:PR)
40	10	4	201	10.3	1:19.5
25	25	4	130	9.8	1:13.3
10	40	4	93	8.2	1:11.3

Table 2.5: Etch result (15 min etching) for different mix ratio or SF_6 and Ar while RF power and chamber pressure was fixed at 300 W and 20 mTorr respectively.

In table 2.5, the etching results are presented for four different ratios of SF_6 and Ar. It can be noticed that by adding Ar, indeed, the overall etch-rate improves. This could be possibly due to the inert Ar gas cleaning the etch residues/byproducts from the surface of the sample. We noticed that the highest PZT etch rate was achieved with SF_6 and Ar mixture with a flow rate ratio of 4:1. However, SF_6 is an aggressive etchant towards the photoresist mask, which results in a poor

etch selectivity. Hence, in the next trial, we tested mixing another fluoride-based reactant gas.

2.4.3 PZT etch trial 3: mix gases with CHF_3

In [8], it was shown that etching the PZT film with CHF_3 gives better selectivity. Therefore, in the new trial, we introduced CHF_3 among the reactant gases. In table 2.6, the etch results from different flow rates of SF_6 and CHF_3 are presented while keeping the flow rate of Ar and O_2 fixed. The RF power and the chamber pressure were also varied to find the best etching result.

Recipe #	SF_6 (sccm)	CHF_3 (sccm)	RF power (W)	pressure (mTorr)	PR etch (nm/min)	PZT etch (nm/min)	selectivity (PZT:PR)
I	0	40	300	20	28.7	4	1:7.2
II	0	40	450	10	13	12	1:1.1
III	10	30	300	20	107.6	10	1:10.8
IV	10	30	450	20	131.6	18.3	1:7.2
V	10	30	300	10	109	10.9	1:10
VI	10	30	450	10	122	18.4	1:6.6
VII	15	25	300	20	124	11.2	1:11.1
VIII	30	10	300	20	226	12	1:18.8

Table 2.6: Etch result (7 min etching) for different ratios of SF_6 and CHF_3, and different RF power and chamber pressure. The flow rate of Ar and O_2 was fixed at 10 sccm and 5 sccm respectively.

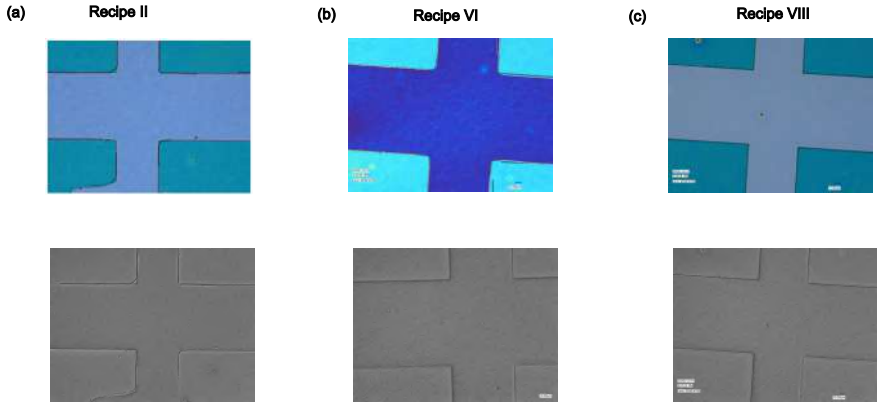

Figure 2.6: Optical image and optical SEM image taken with Keyence microscope show the surface morphology of the etched PZT samples with different recipes.

In table 2.6, three extreme results are highlighted. The best selectivity is

achieved with recipe II, where no SF_6 is present because SF_6 is an aggressive etchant for the photoresist. However, the PZT etch rate is lower. With recipe VIII, the etch selectivity is the worst, but the PZT etch rate is high (considering it was performed at 300W of RF power). Recipe VI, which has an average ratio of SF_6 and CHF_3 gives a decent etch rate and selectivity. Subsequently, the optical images of the etched PZT samples from these three recipes were taken with a microscope, as shown in fig 2.6. We see that with recipe II (high CHF_3 flow rate), the etched surface and the side walls are rather rough. On the other hand, with recipe VIII (high SF_6 flow rate), the etched surface and the side walls were smoother. This suggests that PZT etching by SF_6 is more chemical etching compared to that by CHF_3. Thus, depending on the requirement of high selectivity or high etch rate, recipe II or VIII could be used. For a balanced etch rate and selectivity, recipe VI (with a mixture of both CHF_3 and SF_6) can be implemented.

2.5 SiO_2 under-etching for surface micromachining

SiO_2 is a commonly used sacrificial layer for surface micromachining to fabricate micro-sensors and actuators in integrated circuit (IC) technology [9]. The common etchants for under-etching SiO_2 are HF and BHF solutions. HF is a very high vapor pressure solution, with a room-temperature boiling point. Typically, the HF solution is water diluted so that the hydrogen bonding between H_2O and HF can increase the boiling point, making it easier to handle or transport [10]. HF can be used both in solution and vapor form. BHF is a buffered solution typically containing 7 parts by volume 40% ammonium fluoride (NH_4F) and 1 part by volume 49% HF. These etchants offer higher selectivity against Si because of the high electronegativity of fluoride, which helps break the strong Si-O bond in SiO_2. Notably, both these etchants are highly corrosive and can have irreversible health complications if exposed to the skin or eyes [11]. Hence, in addition to the personal protective equipment (PPE), extra measures are taken to avoid their exposure to anyone around. For example, all the experiments with these etchants were only done inside a dedicated wet bench, where the closed (transparent) shutter and continuous vertical airflow ensured that no solution or vapor escaped outside the wet bench.

The etch rate of SiO_2 depends on its deposition method. For example, buried SiO_2 in SOI samples is grown thermally at a high temperature ($\sim$ 800-1200°C). This results in a chemically strong, highly dense, and good quality film, which has a low etch rate compared to the SiO_2 deposited with PECVD in our clean room. The PECVD process is carried out at a lower temperature ($\sim$ 270°C), and it gives a less dense and chemically unstable SiO_2 with impurities like H and N.

2.5.1 Wet-etching of SiO_2

The wet-etching process of SiO_2 is performed with HF or BHF because of its residue-free and uniform under-etching. Additionally, a readily available photoresist layer can be used as a protection mask against wet etchants. The etching process takes place in the following steps:

- Reactants are adsorbed on the SiO_2 surface
- Chemical reaction
- Desorption of the reaction byproducts

The HF solution is used in various concentrations depending on the required selectivity or etch rates. The overall etch reaction of SiO_2 with HF solution is understood to be the following [9, 12]:

$$SiO_2 + 6HF \rightarrow 2H^+ + SiF_6^{2-} + 2H_2O \tag{2.1}$$

However, there is a major issue of resist peeling-off with HF-etching, which appears after a certain etching time or during the resist rinsing process. We believe that the highly mobile HF etchant molecules diffuse through the photoresist mask to attack the underneath oxide, thus weakening the photoresist adhesion. This phenomenon is termed as 'peeling effect'. A thicker photoresist mask can be used to minimize this effect. Additionally, BHF can be a better etchant due to its less mobile HF_2^- ions in the presence of NH_4^+ ions, resulting in a low diffusion through the photoresist mask. The etching mechanism with BHF is considered to be the following: [9, 13]:

$$SiO_2 + 4HF + 2NH_4F \rightarrow 2NH_4^+ + SiF_6^{2-} + 2H_2O \tag{2.2}$$

Hence, BHF was preferred for the under-etching process. We used hard baked photoresist (TI 35E) as a protection mask against BHF to protect the sensitive layer or components on the chip. Figure 2.7(b) shows that even if we have some lateral margin of the protection mask, the wet etchant can sip through the interfaces to cause lateral etching. Another issue with the wet etching is the 'peeling off' of the photoresist mask.

We faced some challenges later on in depositing the new PZT layers. Hence, we decided to use an oxide layer (SiO_x film) in place of a PZT layer to test the protection mask during the under-etching process. We deposited ~300 nm SiO_x film on an SOI substrate using a PECVD process. Then a TI 35E photoresist mask was patterned using the steps described above in 2.4. A dry-etching was done in the RIE tool to make underetch windows through the SiO_x/Si layer. Finally, this sample was dipped into the BHF solution to enable under-etching of the SiO_2 layer through the windows. This process is illustrated in figure 2.7. Here 2.7 (b),

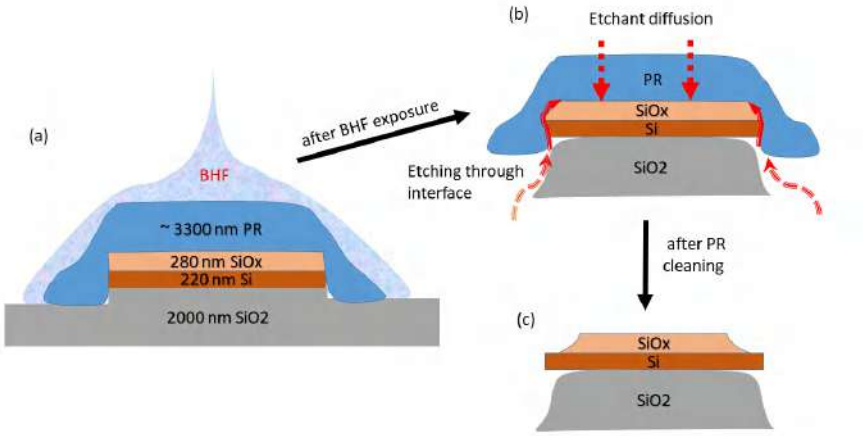

Figure 2.7: (a) Schematic illustration of the BHF wet-etching of sacrificial SiO_2, while protecting the sensitive SiO_x using a photoresist (PR) mask (b) arrows showing the etchant diffusion through the photoresist mask, which causes peeling-off of the photoresist mask (c) a typical cross-section view of sacrificial SiO_2 after a short etching time.

shows how the wet etchant attacks through the multi-layer interfaces such as the Si-photoresist interface. We hypothesize that if we deep-etch the windows into SiO_2, the etchant will take more time to reach the Si-photoresist interface. That could reduce the extent of the SiO_x lateral etching. Hence, we prepared two test samples. In one sample, the dry-etching was done up to 1900 nm thickness of SiO_2. Meanwhile, in the other sample, the dry-etching was done up to 1200 nm thickness of SiO_2. Figure 2.8 shows the optical images of these two samples after 20 min exposure in the BHF solution. We observed that, indeed, in the case of a deep etched SiO_2 sample (with 1200 nm thick SiO_2), the lateral etching was lower as shown in 2.8 (b).

The following hypothesis was that the lateral etching was being exacerbated by the peeling effect on the edges of the photoresist. Hence, we prepared two samples; one with $\sim$ 3340 nm of TI 35E photoresist, and another with a thicker $\sim$ 6400 nm photoresist AZ 10xT.

Figure 2.9 (a) and (b) show the optical images of the two samples with thin and thick photoresists, respectively, after 30 min exposure in the BHF solution. We observed that for the same etching duration, the lateral etching is lesser with the thicker photoresist. To further confirm this, we took the cross-section image of these structures with an SEM as shown in figure 2.10. Here 2.10(a) and (b) are the SEM images of the thinner resist sample, while 2.10(c) and (d) are the SEM images of the thicker resist sample. From comparing the image (b) and (d), it

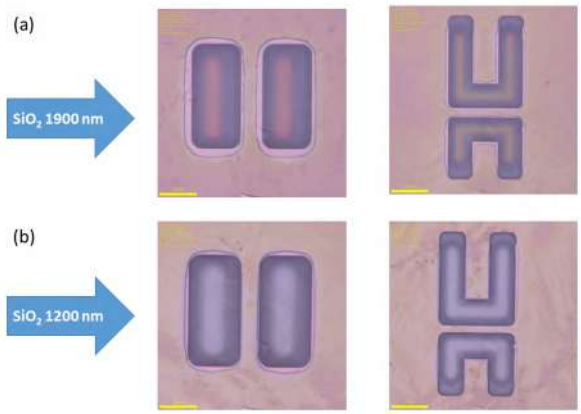

Figure 2.8: Optical image after 20 min exposure in BHF solution of samples with (a) 1900 nm SiO_2 (b)1200 SiO_2 nm.

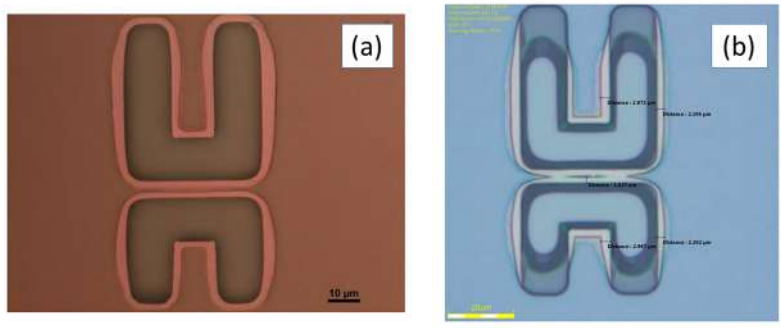

Figure 2.9: Optical image after 30 min exposure in BHF solution of samples with (a) ∼ 3340 nm thick TI 35E photoresist (b) ∼ 6400 nm thick AZ 10xT photoresist.

is clear that the lateral etching of the SiO_x layer is lower than the thicker resist sample. This indicates that the photoresist mask might have been peeling-off on the edges due to the diffusion of etchant through the thinner photoresist mask.

2.5.2 Dry-etching with HF vapor

As we noticed with the wet-etching, there is an unavoidable issue of lateral etching. This issue can be mitigated to some extent by using a thicker photoresist and having some lateral margin of the mask but these measures compromise the de-

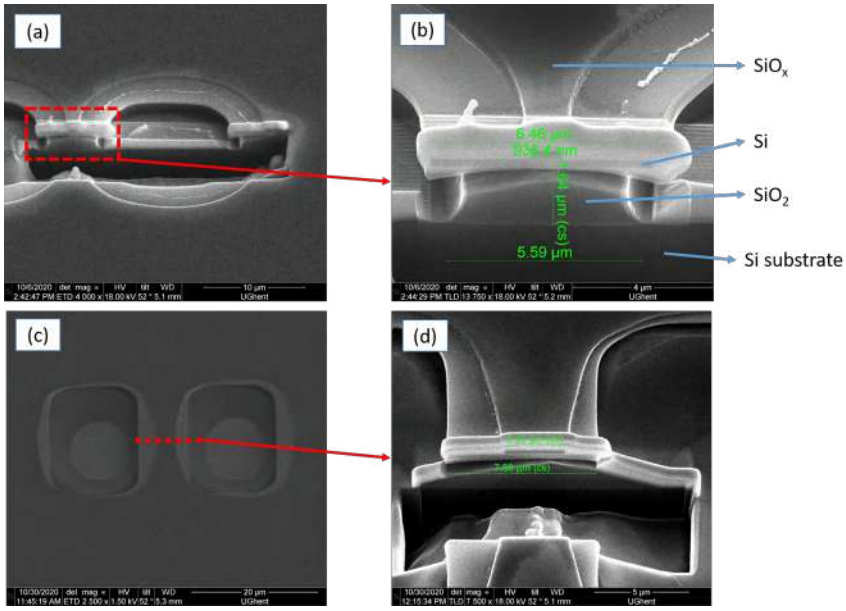

Figure 2.10: SEM imaging of the samples after 30 min BHF exposure. (a) SEM cross-section of the sample with thinner TI 35E photoresist (b) a zoom-in image shows the lateral etching (c) SEM image of the sample with thicker AZ10xT before the cross-section (d) a cross-section image of the sample showing less lateral etching.

vice resolution. Another major issue with the under-etching is that the suspended structures tend to collapse. This is mainly due to the capillary force between the suspended structures and the substrate during the drying process [14]. Considering these drawbacks, etching of SiO_2 with HF vapor was investigated. In this method, HF vapor etches SiO_2 in a quasi-dry environment allowing stiction-free release.

We used an HF vapor phase etcher (vpe) apparatus from Idonus [15] as shown in fig 2.12. 49 % HF solution is filled in the reaction chamber. A pure HF solution is very volatile and quickly evaporates at room temperature. That is why it is mixed with water so that the hydrogen bonding between HF and H_2O ensures a higher boiling point. Nevertheless, the evaporation at room temperature remains high enough to etch SiO_2. The samples could be loaded on the wafer holder using either an electrostatic chuck or a mechanical clamp. After loading the samples on the wafer holder, the wafer holder is put upside down on top of the reaction chamber.

The etching process with HF vapor is supposed to take place in the following steps [16, 17]:

$$SiO_2 + 2H_2O \rightarrow Si(OH)_4$$
$$Si(OH)_4 + 4HF \rightarrow SiF_4 + 4H_2O \tag{2.3}$$

In the first step, the water (moisture in the air) initiates the reaction and forms silanol groups ($Si(OH)_4$). Subsequently, the silanol group is attacked by HF to produce more water and silicon fluoride (SiF_4). Finally, these reaction products are released from the surface by desorption.

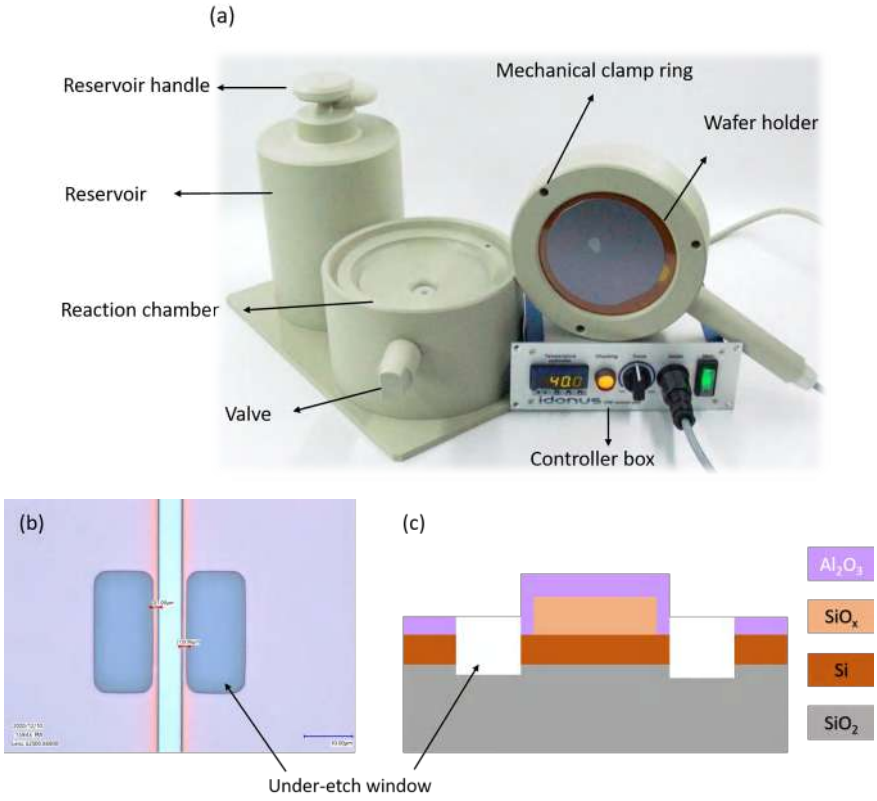

Figure 2.12: (a) An image of HF vpe-100 tool taken from the Idonus website [15] (b) optical image showing the top view of a sample prepared for under-etching (c) a diagram showing the cross-section view of the sample.

To test the dry release by HF vapor and the protection mask against it, we used a SiO_x/SOI sample. The goal was to protect the HF-sensitive SiO_x layer, which was deposited with PECVD. The sample was prepared as follows:

- First, the PECVD deposited SiO_x layer was patterned with RIE using a AZ5214 photoresist mask (image reversal lithography).

- After thoroughly cleaning the sample, it was loaded in an ALD chamber to deposit 50 nm Al_2O_3.

- Now, TI 35E photoresist was spin-coated (at 3000 rpm for 40 seconds) on the Al_2O_3/patterned SiO_x/SOI sample and under-etch windows were patterned with image reversal UV lithography.

- The patterned mask sample was loaded in the RIE chamber to etch the Al_2O_3, the Si and a bit of the SiO_2 layer through the patterned windows. The residual SiO_2 thickness was measured to be $\sim$ 1750 nm using Filmetrics.

- The photoresist mask was removed using acetone & IPA cleaning, followed by a 10 min dip in AZ 100 remover at 70°C, and finally 5 min O_2 plasma exposure.

Before the sample was loaded in the HF-VPE, it was baked at a high temperature (150 °C) for 10-15 min on a hotplate to allow evaporation of any water on the sample. Figure 2.13(a) shows the prepared sample (Al_2O_3 encapsulated on patterned SiO_x beam on SOI). For the under-etching process, the sample was loaded in the HF-vpe with the sample holder temperature set to 40 °C. After 3 min of exposure, the sample was carefully unloaded with HF resistant plastic tweezers. Figure 2.13(b) shows an SEM image of the sample after the HF vapor exposure, and before making the cross-section on the beam[9]. Figure 2.13(c) shows the SEM image of the beam cross-section. The zoom-in image in figure 2.13(d) shows that SiO_x, despite being encapsulated by the Al_2O_3 hard mask, was etched. That means some amount of HF vapor etchant is able to (laterally) penetrate through the hard-mask interface. Also, SiO_x, being very sensitive to the HF vapor, is not a good alternative to the PZT (chemically more stable) to test the protection mechanism.

Eventually, we tried under-etching a PZT layer deposited on a silicon-on-insulator (SOI) substrate. Figure 2.14 (a) and (b) show the optical images of a cantilever patterned 400 nm thick PZT film on SOI, before and after 60 min HF vapor exposure respectively. We noticed that even after 60 min of exposure, the PZT layer looks relatively intact compared to the SiO_x layer used earlier. Although, we could notice some local dissolution (pitting, inter-granular corrosion) on the PZT surface.

[9]FIB cross-section and SEM imaging was done by Liesbet Van Landschoot

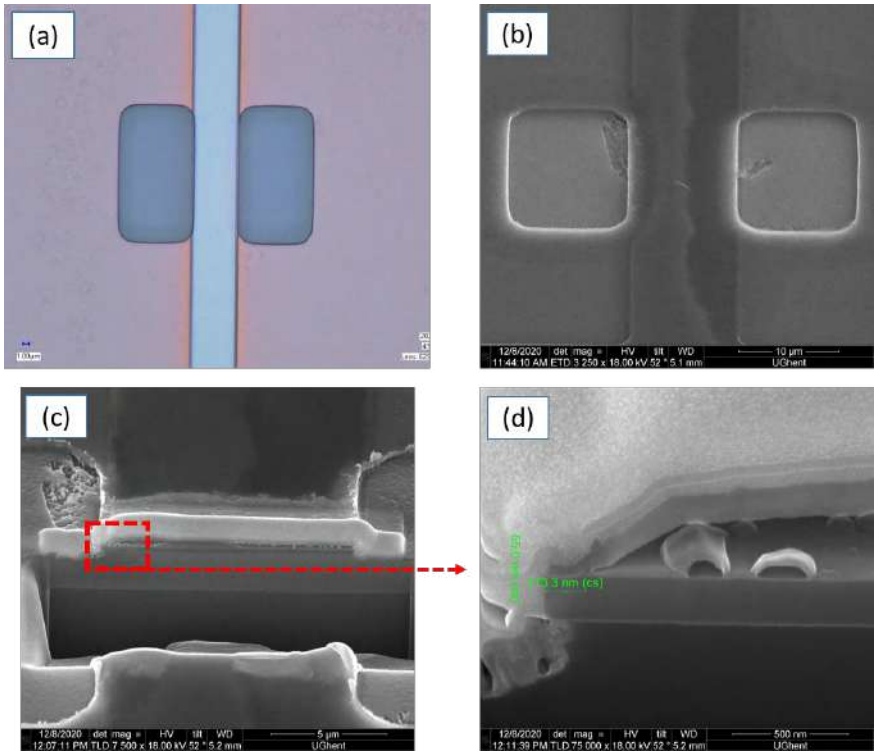

Figure 2.13: (a) Optical image of a sample ready for the HF vapor exposure (b) SEM image of the sample after HF vapor etching, and before making the cross-section with FIB (c) cross-section image of the beam (d) zoomed-in image showing under-etched SiO_x despite being encapsulated by Al_2O_3 mask.

2.6 Conclusion

The process flow to fabricate suspended devices with PZT film on SOI was optimized. We varied the etch gases, RIE chamber pressure and RF voltage to find a good PZT etch rate and selectivity against the photoresist mask. We released the PZT on Si device by isotropically etching a SiO_2 sacrificial layer. For this under-etching process, we tried HF and BHF. We found the HF vapor phase etching to be an effective etching mechanism for our sample. The downside of this technique is that the substrate temperature is the only controllable parameter in our HF vapor phase etcher. Hence, it is difficult to get very reliable and repeatable etch results. Nevertheless, this dry process gives stiction-free release and freedom to monitor the release process immediately after the exposure. We also tested the protection capability of ALD deposited Al_2O_3 thin film against the HF vapor. This ultrathin hard mask can be left on the sample, as it does not exert any significant

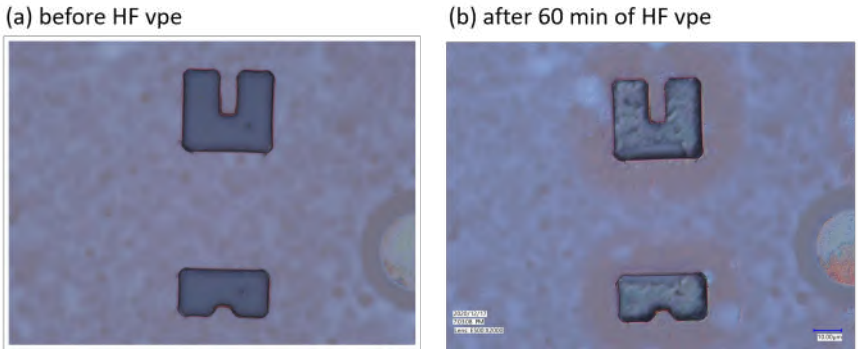

Figure 2.14: HF vapor etching of PZT/SOI. (a) a 400 nm PZT on SOI after patterning the etch windows with RIE (b) suspended PZT/Si cantilevers after 60 min of HF vapor etching.

mass-loading effect on the MEMS devices.

References

[1] John Puthenparampil George. *Integration of ferroelectric thin films on silicon for electro-optic devices*. PhD thesis, Ghent University, 2016.

[2] J. P. George, P. F. Smet, J. Botterman, V. Bliznuk, W. Woestenborghs, D. Van Thourhout, K. Neyts, and J. Beeckman. *Lanthanide-Assisted Deposition of Strongly Electro-optic PZT Thin Films on Silicon: Toward Integrated Active Nanophotonic Devices*. ACS Applied Materials & Interfaces, 7(24):13350–13359, 2015.

[3] Parshuram B Zantye, Ashok Kumar, and AK Sikder. *Chemical mechanical planarization for microelectronics applications*. Materials Science and Engineering: R: Reports, 45(3-6):89–220, 2004.

[4] JP George. *In-plane characterization of PZT thin films for the creation of a general impedance model*. Journal of Applied Physics, 129(9), 2021.

[5] Bakke, Thor and Schmidt, Jan and Friedrichs, Martin and Völker, Benjamin and Bakke at ipms, Thor and De. *Etch stop materials for release by vapor HF etching*. Proc. MicroMechanics Eur. Workshop, 16, 01 2005.

[6] Piotr Firek, Jan Szmidt, Katarzyna Nowakowska-Langier, and Krzysztof Zdunek. *Electric characterization and selective etching of aluminum oxide*. Plasma Processes and Polymers, 6(S1):S840–S843, 2009.

[7] *Understanding Film Thickness Measurements*. url-https://www.filmetrics.com/technology. URL accessed: 2023-09-01.

[8] Shi Peng and Yao Xi. *Effect of microstructure on reactive ion etching of sol–gel-derived PZT thin film*. Ceramics International, 30(7):1215–1218, 2004. 3rd Asian Meeting on Electroceramics.

[9] J Bühler, FP Steiner, and H Baltes. *Silicon dioxide sacrificial layer etching in surface micromachining*. Journal of Micromechanics and Microengineering, 7(1):R1, 1997.

[10] David J. Monk, David S. Soane, and Roger T. Howe. *A review of the chemical reaction mechanism and kinetics for hydrofluoric acid etching of silicon dioxide for surface micromachining applications*. Thin Solid Films, 232(1):1–12, 1993.

[11] D. Peters and R. Miethchen. *Symptoms and treatment of hydrogen fluoride injuries*. Journal of Fluorine Chemistry, 79(2):161–165, 1996.

[12] S. Verhaverbeke, I. Teerlinck, C. Vinckier, G. Stevens, R. Cartuyvels, and M. M. Heyns. *The Etching Mechanisms of SiO2 in Hydrofluoric Acid*. Journal of The Electrochemical Society, 141(10):2852–2857, oct 1994.

[13] Yasuo Kunii, Satoshi Nakayama, and Masahiko Maeda. *Wet Etching of Doped and Nondoped Silicon Oxide Films Using Buffered Hydrogen Fluoride Solution*. Journal of The Electrochemical Society, 142(10):3510–3513, oct 1995.

[14] Niels Tas, Tonny Sonnenberg, Henri Jansen, Rob Legtenberg, and Miko Elwenspoek. *Stiction in surface micromachining*. Journal of Micromechanics and Microengineering, 6(4):385, dec 1996.

[15] *Idonus-vapor phase etcher*. `https://www.idonus.com/`. URL accessed: 2023-03-01.

[16] C. R. Helms and B. E. Deal. *Mechanisms of the HF/H2O vapor phase etching of SiO2*. Journal of Vacuum Science & Technology A, 10(4):806–811, 1992.

[17] M Offenberg. *Vapor HF etching for sacrificial oxide removal in surface micromachining*. Electrochemical Soc. Fall Meet, 1994, 94(2):1056–1057, 1994.

3 SAW modulation

This chapter investigates the piezoelectric actuation of surface acoustic waves (SAWs) with the PZT film. An inter-digitated transducer (IDT) was fabricated on the PZT film to generate SAW through RF driving. The SAW actuation was characterized by the electrical measurement of the IDTs, followed by the optical measurement of the SAW-induced phase modulation.

3.1 Electrical characterization of SAW

When the applied RF frequency to the IDT is equal to the resonance frequency (determined by the IDT period), SAWs are launched in both directions of the IDT, perpendicular to its aperture. At this frequency, the input RF power is converted into acoustic power, lowering the reflected RF power from the IDT. This can be detected as a dip in the electrical reflection scattering parameter (S_{11}) of the IDT. Furthermore, if there is another IDT along the SAW propagation, it can convert the acoustic power back into the electrical power. This transduction can be detected as a peak in the electrical transmission scattering parameter (S_{21}) measured on the second IDT [1, 2].

The electrical scattering parameters on our IDTs were measured using a vector network analyzer (VNA). Before the measurement, the VNA (Fieldfox) was calibrated with a standard calibration substrate using the short-open-load-through (SOLT) method for our two-port system. An RF probe (GS100), connected to the VNA via an SMA cable, was used to apply an electrical signal of -10 dBm to the

IDT contact pads. Another RF probe was connected to the VNA to detect the electrical signal from the other IDT. This two-port measurement system is shown in figure 3.1. The contact pads of the IDT (each 100 μm $\times$ 100 μm) with a center-to-center distance of 100 μm were designed to match the pitch (100 μm) of the GS100 probes.

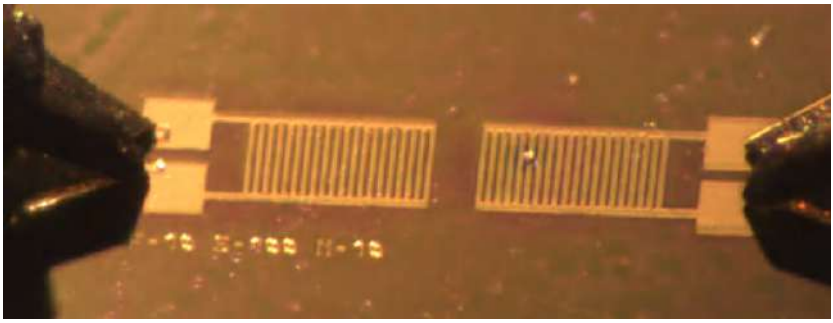

Figure 3.1: An IDT-IDT pair of pitch 20 μm, aperture 200 μm and number of finger-pairs 10 separated by 100 μm. Two GS probes are connected to the contact pads of the IDTs for the electrical measurement

3.1.1 Characterization without poling

In the first trial, IDT pairs were fabricated on two types of samples. One on a standard $LiNbO_3$ (128° Y cut, DSP SAW grade [3]) as a control sample to bench-mark the SAW transduction. And a second one on a 150 nm PZT thin film deposited on a Si substrate as a test sample. The PZT was deposited as described in [4]. The IDT-pairs were patterned with UV lithography, followed by deposition of a 20 nm Ti/ 350 nm Au layer through thermal evaporation and a lift-off process. A fabricated IDT-pair is shown in figure 3.1. For detailed fabrication steps, see chapter 2.

Figure 3.2 shows the magnitude of the electrical reflection parameter S_{11} and transmission parameter S_{21}, measured on two IDT-pairs of different periods from the control sample (LN). The IDTs with pitch 6 μm, aperture 100 μm, and 10 finger-pairs were separated by 20 μm. The IDTs with pitch 20 μm, aperture 200 μm, and 10 finger-pairs were separated by 100 μm.

The IDT of pitch 6 μm shows a strong dip at 294 MHz in S_{11}, and a strong peak at the same frequency in S_{21}. Similarly, the IDTs of pitch 20 μm show a strong dip at 96.3 MHz in S_{11} and a corresponding strong peak in S_{21}. This indicates that the S_{11} dips and corresponding S_{21} peaks are from the SAW actuation because the SAW resonance frequency is determined by the IDT period. Therefore, as expected the standard LN substrate shows actuation of a SAW mode.

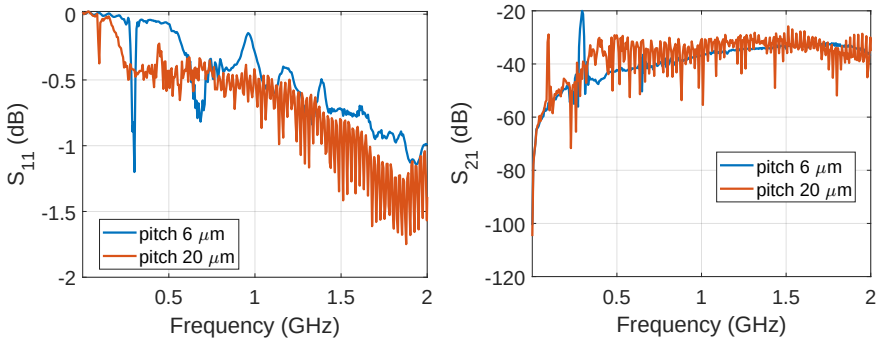

(a) (b)

Figure 3.2: VNA measurement on IDT fabricated on LN substrate. (a) and (b) shows the magnitude of S_{11} and S_{21} measured on two IDTs with different periods.

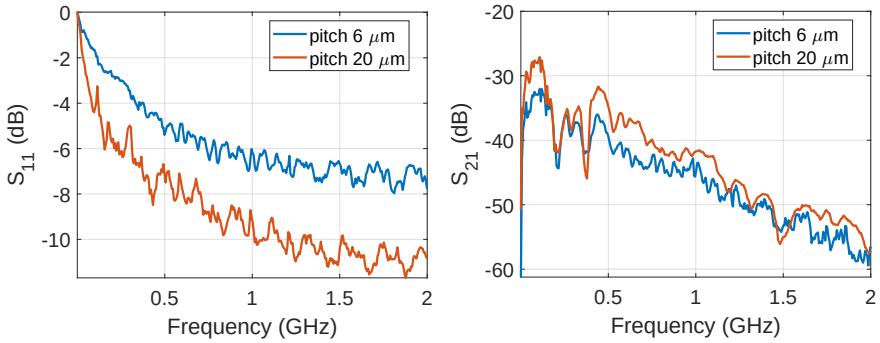

(a) (b)

Figure 3.3: VNA measurement on IDT fabricated on 150 nm PZT deposited on a Si substrate. (a) and (b) shows the magnitude of S_{11} and S_{21} measured on two IDTs with different periods.

Now that the measurement method was verified, the test sample with IDTs on an as-deposited PZT film was characterized. Figure 3.3 shows the electrical scattering parameters measured on the IDT-pairs from the test sample. Despite having similar IDT-pairs as the LN control sample, no clear dip in S_{11} or peak in S_{21} from the test sample was observed. This lack of SAW actuation alluded that our as-deposited PZT film might not have any significant piezoelectric effect.

3.1.2 PZT poling

The fact that our PZT film is a polycrystalline material, was not considered in the first electrical characterization. This could be a reason why we did not see any actuation. Because the macroscopic behavior of a polycrystalline material is determined by the net crystallographic orientation of its domains [5]. Hence, orienting all the domains in a common direction is crucial to maximize the net effect. The domains can be aligned by applying a sufficiently high electric field through the process known as electrical poling.

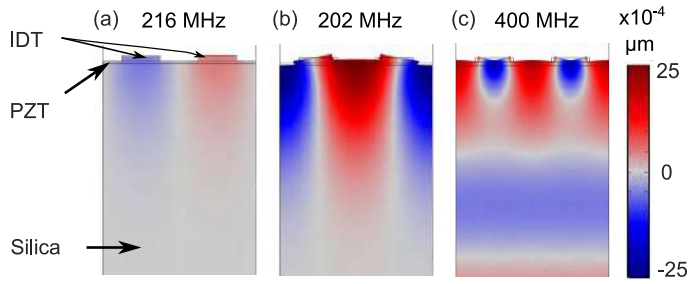

Figure 3.4: FEM simulation showing the vertical displacement from the SAW actuation for three PZT domain polarities: (a) out of the substrate plane, (b) uniformly in-plane, perpendicular to the IDT fingers, and (c) periodically oriented along the IDT electric field lines. The unit cell was driven with an RF signal of amplitude 1V.

To determine how the PZT domain polarization affects the SAW actuation, an FEM simulation was carried out on an IDT unit cell (1 period) as shown in figure 3.4. The pitch (period)[1] of the IDT was set 6 μm (12 μm). The multi-layered unit cell consisted of a 350 nm Au electrode, a 200 nm PZT film, and a Silica substrate with thickness 4 $\times$ IDT period. A Floquet periodic boundary condition was imposed on the left and right boundaries of the unit cell. The bottom of the unit cell contained an additional 1 IDT-period thick perfectly matched layer (PML) domain to absorb the incoming acoustic waves. The bottom-most boundary was set as a low-reflecting boundary to avoid any reflection. After meshing the setup, the piezoelectric response was simulated in the frequency domain.

Figure 3.4 shows the actuated SAW modes for three orientations of the PZT domain polarization: (a) out-of-plane polarization, (b) uniform in-plane polarization, perpendicular to the IDT-aperture, and (c) periodic polarization along the electric field lines applied by the IDT. We notice that the resulting displacement is much

[1]The pitch of an IDT here is the distance between the two successive electrodes. The period of an IDT is the distance between the two similar bias (i.e. source or ground) electrodes. So, an IDT period = 2 $\times$ pitch.

weaker with the out-of-plane oriented PZT domains (a), compared to the in-plane oriented PZT domains (b), and (c). This can be explained by the inverse piezoelectric tensor of PZT. From the piezoelectric constitutive equation, the induced strain is determined as [6],

$$\begin{bmatrix} S_1 \\ S_2 \\ S_3 \\ S_4 \\ S_5 \\ S_6 \end{bmatrix} = \begin{bmatrix} 0 & 0 & d_{31} \\ 0 & 0 & d_{31} \\ 0 & 0 & d_{33} \\ 0 & d_{24} & 0 \\ d_{15} & 0 & 0 \\ 0 & 0 & 0 \end{bmatrix} \begin{bmatrix} E_x \\ E_y \\ E_z \end{bmatrix},$$

where d_{ij} is the tensor describing the inverse piezoelectric effect for PZT and E_i is the applied electric field. In the simulation, we used the following inverse-piezoelectric coefficients for PZT: d_{31} =-171 pm/V, d_{33} =374 pm/V, $d_{15} = d_{24} =$ 584 pm/V [7].

From this relation, we see that for a longitudinal actuation of PZT (necessary to launch a SAW), the applied electric field should be along the z-axis (E_z) in the crystal coordinate system, i.e. along the PZT domain polarization. Therefore, in order to have an effective SAW actuation with an IDT, the domains should be aligned (uniformly or periodically) in the substrate plane, perpendicular to the IDT aperture.

Furthermore, we notice that a periodic orientation of the PZT domains (figure 3.4(c)) results in a SAW resonance frequency (400 MHz) that is almost twice the SAW resonance frequency (202 MHz) from the PZT with all domains uniformly in-plane oriented (figure 3.4(b)). This is because the actuation with a periodic domain polarity results in a SAW wavelength that is half of the IDT period, hence the resonance frequency doubles.

3.1.3 Characterization with PZT poling

Our deposition method results in PZT films grown preferentially in c-orientation (out of the substrate plane) [4]. That means, as per the analysis before, that the PZT film needs to be poled in-plane to have a strong SAW actuation. To experimentally verify the poling effect, a new series of experiments was started. The new devices were designed to allow in-plane poling of the PZT film.

In the first fabrication step, parallel electrode-pairs (separation 80-150 μm) were defined with laser direct write (LDW) lithography[2], followed by deposition of a 20 nm Ti/ 350 nm Au layer through thermal evaporation and a lift-off process. These metal electrodes were used to uniformly pole the PZT film in-plane, for about 1 hour at 40°C. The applied DC voltage varied between 820-1100 V, depending on the electrode separation.

[2]DWL was done by Thomas Vervust

In the second step, the same metallization process was repeated for fabricating test IDTs (in the poled PZT region) and control IDTs (in an unpoled region) as shown in figure 3.6(a). The number of finger-pairs was limited to about 5-7, given the resolution of the lithography process and the limited spacing between the poling electrodes. For the same reason, only a standalone IDT was fabricated rather than an IDT-IDT pair. This does not compromise the characterization as it was observed from the LN sample that the S_{11} response in itself enables the verification of a SAW actuation.

For the poling process a direct current (DC) voltage source with low current output was used. The poling voltage was limited by the breakdown voltage of the PZT film, which varied from sample to sample. On average the PZT breakdown voltage was ~ 20 V/μm. For some devices (with larger electrode gaps), the voltage source could not provide the required poling voltage i.e. $>$1kV. In that case, a voltage amplifier was used next to the voltage source. An example of a sample, that experienced an electrical breakdown is shown in figure 3.5. To avoid this situation, the current compliance should be set very low ($<$1 mA).

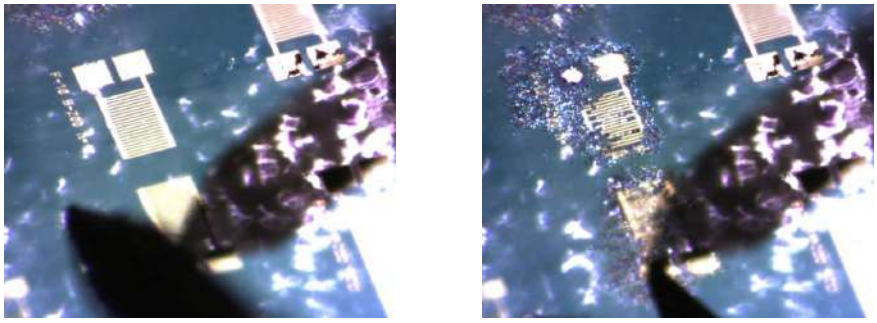

(a) (b)

Figure 3.5: Device breakdown during the poling process. (a) Before poling, (b) After a few minutes of poling at high DC voltage exceeding the breakdown voltage

In figure 3.6(a) a microscope image of a test IDT (between electrodes) and an identical, control IDT (without electrodes) fabricated on a PZT-on-glass substrate are shown. The PZT film under the test IDT is uniformly in-plane poled (using parallel electrodes), whereas, for the control IDT, it is unpoled. Figure 3.6(b) shows the electrical reflection parameter S_{11} measured on the two types of IDTs (period 16 μm). We observe two dips, at 161 MHz and 247 MHz, in the S_{11} measured on the test IDT and none from the control IDT. These dips indicate the actuation of acoustic waves because the input RF power is now converted into acoustic power, lowering the reflected RF power. Therefore, this result already indicates that the IDT deposited on the poled PZT is more efficient in actuating

acoustic waves compared to the IDT on as deposited (unpoled) PZT. Figure 3.6(c) shows the S_{11} response for two IDTs with different periods. We observe that the resonance frequencies shift proportionally with the IDT period. This corroborates that, indeed, the S_{11} dips are from the acoustic wave actuation, as their excitation frequencies are determined by the IDT period. Thus, we conclude that our PZT film exhibits a piezo-electric effect and allows for the actuation of acoustic waves.

With the uniform in-plane poling scheme using an electrode pair across the IDT pattern, the size of the poled PZT region is limited by the maximum applicable voltage. Consequently, the size of the actuators is also limited. Therefore, in subsequent devices, we poled the PZT film using the IDT electrodes themselves.

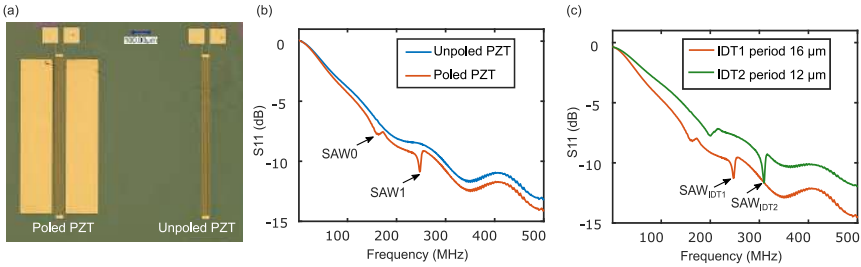

Figure 3.6: (a) Microscope image showing a test IDT fabricated in between parallel electrode bars (80 μm spacing) for the poling process and an identical control IDT fabricated without the electrode bars. (b) S_{11} signal measured for test (poled) and control (unpoled) IDT with period 16 μm. (c) S_{11} signal measured for poled IDTs with period 12 μm and 16 μm.

3.2 Fabrication of integrated SAW modulator

For characterizing the interaction of SAW with the light signal in integrated waveguides, we used an SOI photonic chip, fabricated through a multi-project wafer (MPW) run, as the starting point. In the MPW fabrication process, the waveguides were defined in a 220 nm thick silicon layer on top of a 2 μm buried oxide layer. The chips were planarized using oxide deposition and chemical mechanical polishing (CMP). We deposited a 200 nm thick PZT layer on the SOI chip. We then defined IDTs on top of the PZT layer using optical lithography, followed by deposition of 20 nm Ti/ 350 nm Au layer through thermal evaporation and a lift-off process as shown in figure 3.7. Contrary to the approach taken for the glass substrate described in the previous paragraph, for these chips, the PZT in the IDT region was poled using the IDT itself by applying a voltage of 30-60 V (depending on the IDT-finger spacing) at 40°C for about 40 min.

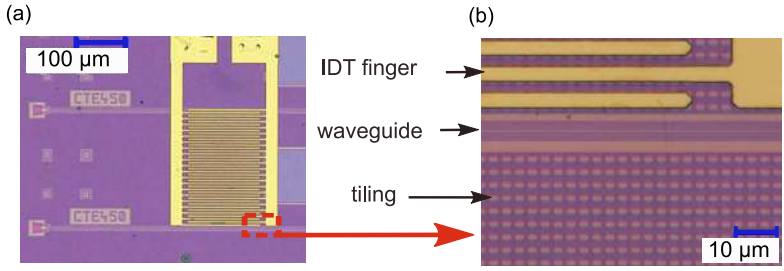

Figure 3.7: (a) Microscope image of an IDT with finger-width 3µm, aperture 180µm and 20 finger-pairs, (b) zoomed-in image showing the tiling pattern (containing shallow and deep etched Si) distributed over the regions without waveguide designs. These patterns have a periodicity of 3 µm and are defined in the 220 nm thick Si-device layer to maintain uniformity during the wafer fabrication.

3.3 Optical characterization of SAW

The acoustic wave excited by the IDT results in a dynamic strain profile, which perturbs the refractive index of the medium (photo-elastic effect). In the waveguide, this index modulation diffracts the incident carrier mode into two sidebands. After traveling through the modulator of length L, the modulated field can be described as (for detail, see 3.5.1),

$$\psi_1(t) = \Re A_1\{e^{i\omega_0 t} + \frac{\alpha(L)}{2}[e^{i(\omega_0+\Omega)t} - e^{i(\omega_0-\Omega)t}]\} \tag{3.1}$$

We thereby assumed that the modulator is short; thus, the phase mismatch between the modulated signals (sidebands) and the carrier mode is negligible.

In this equation (3.1), A_1 is the electric field amplitude of the output light from the DUT (waveguide), ω_0 is the angular frequency of the incident light, Ω is the angular frequency of the acoustic wave and $\alpha(L)$ is the phase modulation amplitude. $\alpha(L) = -(2\pi\Delta n_{eff}L/\lambda_0)$ where Δn_{eff} is the effective index change induced by the acoustic wave and λ_0 is the free space wavelength of the light. $\alpha(L)$ is a measure of the modulation efficiency and depends on the coupling between the induced acoustic field and the optical field in the waveguide.

To experimentally measure the optical phase modulation, we used a heterodyne setup as shown in figure 3.8. The output signal of the modulator is combined with a frequency-shifted signal from an acousto-optic modulator(AOM) to down-convert the carrier signal in the photodetector. The frequency-shifted signal exiting the AOM is given by:

$$\psi_2(t) = \Re A_2\{e^{i(\omega_0+\Delta\omega)t}\} \tag{3.2}$$

Where A_2 is the amplitude of the output light from the AOM and $\Delta\omega = 2\pi\times$ 200

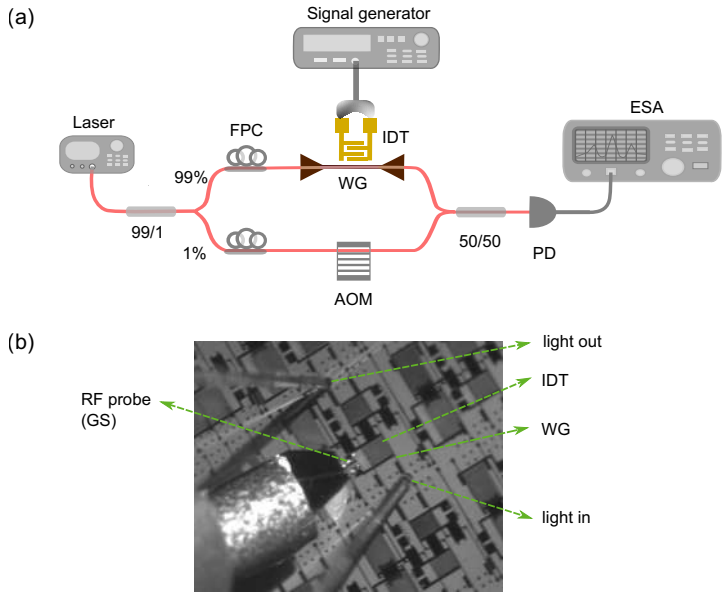

Figure 3.8: (a)Schematic of the heterodyne setup used to measure the acousto-optic phase modulation. A commercial acousto-optic modulator (AOM) was used as a local oscillator to frequency shift the reference signal by 200 MHz. This frequency-shifted signal was then mixed with the phase-modulated signal emerging from the DUT via a 3dB fiber combiner to down-convert the carrier signal on a detector. (b) an image of DUT showing an RF probe connected to the IDT and fiber aligned to the grating coupler of the waveguide.

MHz is the frequency shift induced by the AOM. Thus, the field coupled into the photodiode (PD) is:

$$\psi_{PD}(t) = \psi_1(t) + \psi_2(t)$$

The output current from the PD, I_{PD} is equal to the responsivity of the PD times the optical input power $\implies I_{PD} \propto |\psi_{PD}|^2$. The electrical power measured by the ESA equals $P_{ESA} = I_{PD}^2 \times Z_0$, where Z_0 is the load impedance (50 Ω). Hence, the power spectrum measured in the ESA is proportional to:

$$P_{ESA}(t) \propto \Big[|A_1|^2 + |A_2|^2 + (A_1^* A_2 + A_2^* A_1)\big[cos(\Delta\omega t) + \frac{\alpha(L)}{2}\big\{cos((\Delta\omega + \Omega)t) - cos((\Delta\omega - \Omega)t)\big\}\big] + |A_1|^2 \alpha(L)^2 sin^2(\Omega t)\Big]^2 \tag{3.3}$$

We can ignore the last term, as $\alpha(L) << 1$, and unmodulated terms contribute

only to the DC current. We then obtain,

$$P_{ESA}(t) \propto 4|A_1|^2|A_2|^2\Big[cos(\Delta\omega t) + \frac{\alpha(L)}{2}\Big\{cos((\Delta\omega+\Omega)t) - cos((\Delta\omega-\Omega)t)\Big\}\Big]^2 \tag{3.4}$$

The Fourier transform of equation (3.4) gives a peak signal at the AOM frequency shift $\Delta\omega$, and two sideband peaks at frequencies $|\Delta\omega \pm \Omega|$ introduced by the acoustic wave modulation. Further algebra on equation (3.4) gives us the following expression for the modulation amplitude $\alpha(L)$,

$$P_{ESA}^{\text{AOM}}[dBm] - P_{ESA}^{\text{Sideband}}[dBm] = 20\log\Big[\frac{\alpha(L)[\text{rad}]}{2}\Big] \tag{3.5}$$

Hence, the modulation amplitude $\alpha(L)$ can be extracted independent of the photodetector responsivity and gain. Now, with this $\alpha(L)$, we can calculate the voltage required for a π- phase shift $V_\pi = \pi\, V_{RF}/\alpha(L)$, where V_{RF} is the voltage amplitude of the input RF signal.

For the power of the upper sideband peak in equation (3.4) we find:

$$P_{ESA}^{\text{Sideband}} \propto |A_1|^2|A_2|^2\,\alpha(L)^2\Big(cos((\Delta\omega+\Omega)t)\Big)$$

$$\implies P_{ESA}^{\text{Sideband}} \propto P_{laser}^2 P_{RF}$$

As $\alpha(L)^2 \propto P_{RF}$, where P_{RF} is the applied RF power to the IDT, and $|A_1|^2|A_2|^2 \propto P_{laser}^2$, where P_{laser} is the input laser power. Thus, the above equation can be written as,

$$P_{ESA}^{\text{Sideband}}[dBm] = 2P_{laser}[dBm] + P_{RF}[dBm] + constant \tag{3.6}$$

This shows how the modulated power depends on the input laser power and the driving RF power.

3.3.1 Experimental setup and validation

The experimental setup used for the measurement is shown in figure 3.8. The light signal from a tunable C-band laser (Syntune) was divided into two parts by a 99/1 fiber splitter, with 1% of the signal routed through an acousto-optic modulator (Gooch & Housego Fiber-Q, driver model 1200 AF-AINA-2.5 HCR) to frequency-shift the signal by 200 MHz. The other 99% of the signal was fed into the DUT. A Rhodes & Schwarz-SMR40 signal generator was used as an RF source to actuate the IDT. The modulated signal from the waveguide was mixed with the output signal from the AOM via a 50/50 fiber combiner and fed into a fast photodetector (Thorlab PDB480C). The output of the PD was analyzed with an electrical spectrum analyzer (Agilent N9010A).

After setting up the equipment, first, the optical transmission through a 450 nm wide waveguide with grating couplers was measured. This was done to determine the wavelength of maximum transmission. The grating couplers are designed to have maximum transmission around 1550 nm, as can be seen from figure 3.9(a), before deposition of the PZT film. However, figure 3.9(b) shows that the deposition of the PZT thin film shifts this maximum transmission wavelength. This is due to the difference in refractive index between the PZT film and the standard cladding oxide. The lowering of the optical transmission from the PZT sample (compared to the transmission from the sample without the PZT film) could be attributed to the propagation loss in the PZT and the coupling loss from the PZT-coated grating couplers. After a few other tests, the maximum transmission wavelength was estimated to be around 1590 nm. Hence, for the subsequent modulation measurement, the laser was operated at 1590 nm.

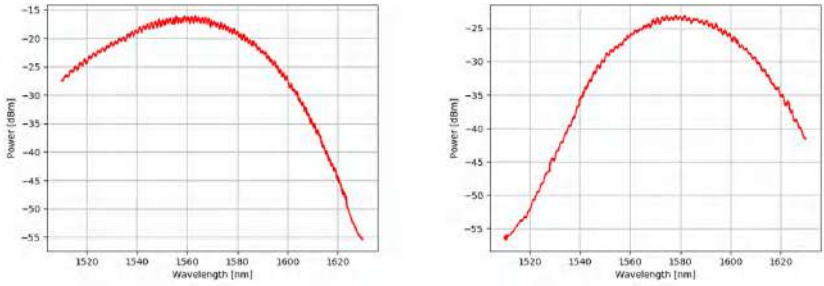

(a) (b)

Figure 3.9: Optical transmission of a 450 nm wide waveguide with input laser power of 1.4 dBm, (a) without PZT film, (b) with 200 nm PZT film on top.

The data sheet of the RF probe (GS100) mentioned the voltage amplitude tolerance to be 50V. Hence, for poling the PZT film under the IDT, the RF probe was used for the smaller electrode gaps (< 4 μm), whereas a DC probe was used for the larger electrode gaps (≥ 4 μm). After poling the PZT film, the modulation spectrum was measured for a given driving RF frequency.

Figure 3.10 (a) shows the phase modulation spectrum measured in a 450 nm wide waveguide when an IDT of period 12 μm, aperture 100 μm and 20 finger-pairs (N_p) was driven with a 19 dBm RF signal at 600 MHz. As expected, strong sideband peaks were observed at 600 $\pm$ 200 MHz. While it was nice to get the desired modulation immediately in the first trial, the moment the RF probe was lifted, the modulated sideband peaks still remained (albeit at a bit lower signal).

Additionally, a sharp peak at the driving RF frequency (600 MHz) was observed. This signal was termed as antenna signal since it appeared at the source frequency. This antenna signal was stronger when the RF probe landed on the

IDT; otherwise, a weaker antenna signal was observed when there was no contact with the DUT. Furthermore, when the RF probe was connected to an IDT far away from the measured waveguide, the modulation sideband still appeared, as shown in figure 3.10 (b). Here, the IDT labeled as E3 has a period of 12 μm and an aperture of 215 μm, whereas F4 has a period of 24 μm and an aperture of 450 μm. Both IDTs (with N_p = 20) were located at different locations on the chip, away from the measured waveguide, such that the actuated SAW from them should not propagate through the waveguide. These observations raised two main questions. First and foremost, where did these observed modulation signals come from? Because they appeared even when the RF probe was not connected to the DUT. Secondly, how to get rid of the (emitted RF) antenna signal? These questions triggered a thorough investigation of the measurement setup.

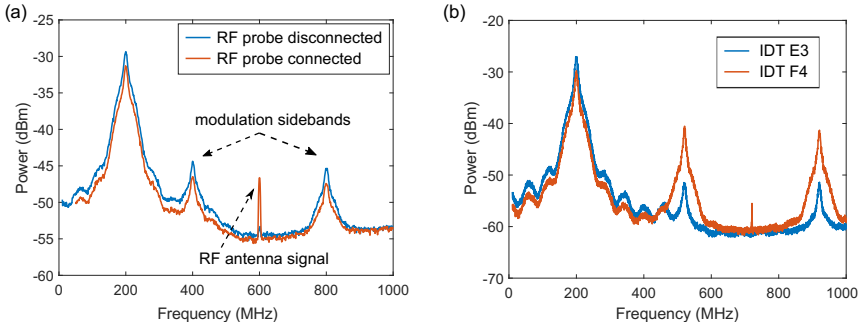

Figure 3.10: Issues with the first measurement trial (a) modulation sideband measured with RF probe connected and disconnected on the DUT. The driving RF signal was 19 dBm at 600 MHz (b) RF probe connected on two different IDTs far away from the measured WG.

3.3.1.1 Troubleshooting the modulation signal

To understand the origin of the modulation signal (sideband peaks) in the first trial, the phase modulation was measured in different configurations. As already shown in figure 3.10, the modulated sidebands appeared when the RF probe was connected to the IDT next to the waveguide, other IDTs on the chip far away from the waveguide, or even when the RF probe was lifted up. Furthermore, the fiber was disconnected from the DUT and directly connected to the PD. So, in this case, no light was on the chip, but when the RF probe landed on one of the IDTs on the chip, strong modulation peaks appeared. Additionally, when either the RF source or the laser was switched off, it disappeared. These observations indicated that the RF signal was interfering with the light signal somewhere other than on the chip. This hypothesis seemed plausible given the strong RF antenna signal that

was observed.

Next, it was tested whether the antenna signal was influencing the modulation because the detector components (PD and EXA) were close to the RF source. A long fiber ($\sim$ 10 m) was used to connect the DUT output to the photodiode (PD) so that the PD and EXA could be kept far away from the RF source. Even then, the modulated signal (rather weak) was observed.

In the next approach, a metal box (from the ID lab[3]), as shown in figure 3.11(a), was used as a Faraday cage. This was used to shield the enclosed equipment from interfering with the emitted RF signal. The cubical box of size $\sim$ 0.5 m contained an RF port and a small hole to allow fiber connection. The fiber from the laser was directly connected to the balanced PD and the RF probe was landed on one IDT on the chip. This was done to allow a false modulation from the emitted RF signal and rule out any modulation from the waveguide next to the IDT. Now, each equipment was put into the Faraday cage (subject to fitting) one by one, as shown in figure 3.11(b) and the phase modulation data was collected with 15 dBm RF signal at 800 MHz. Figure 3.11(c) presents the phase modulation spectrum measured on these arrangements. It can be noticed that when the Syntune laser was put into the Faraday cage, no false modulation was detected. The spectrum remained flat except for the first (200 MHz) and second-order (400 MHz) AOM peaks. This proved that the light was interfering with the RF signal in the laser itself. To further corroborate the laser interference, another laser with better electromagnetic compatibility (EMC), Santec TSL510, and the previously used Syntune laser were tested without the Faraday cage. Figure 3.11(d) shows the phase modulation spectrum from the two lasers. It was clear that the poor EMC of the previously used laser (Syntune) was responsible for the false modulation signal. Hence, the Santec laser was used for the subsequent measurement. Nevertheless, it was noted that for both lasers, the antenna signal was still visible. Therefore, the next troubleshooting was carried out to get rid of this effect.

3.3.1.2 Troubleshooting the antenna signal

As it was observed that the antenna signal (at the driving RF frequency in the measured spectrum in EXA) remained even when the laser issue was solved. The antenna signal was stronger when the RF probe was connected to the (metallic) IDT. It scaled with the RF power but not with the laser power, suggesting its sole dependence on the RF source. In fact, even when the DUT output was disconnected from the balanced PD, a (weak) antenna signal appeared in the spectrum measured with EXA, as shown in figure 3.12(a). To avoid any possible interference with the PD, it was kept in the Faraday cage. It was realized that the antenna signal persisted even when the detection system (balanced PD in Faraday cage+EXA) was taken far

[3] troubleshooting of the antenna signal was assisted by Joris Van Kerrebrouck from the IDLab

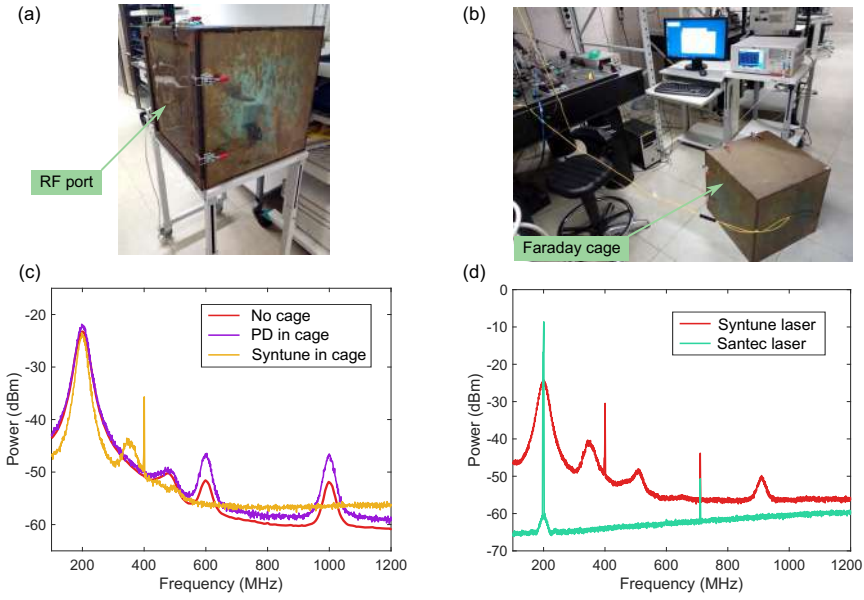

Figure 3.11: Troubleshootinging the modulation signal (a) Faraday cage setup (b) antenna signal at the RF frequency measured even away from the setup i.e. in photonics hub (c) measurement with different equipment in the Faraday cage (d) measurement with two different lasers.

away from the setup. For example figure 3.12(b) shows the antenna signal detected in the photonic hub, while the setup was inside the measurement room. This signal was mitigated only after taking the detection setup to the other corridor, beyond 2 concrete walls from the setup. That means the balanced PD was able to catch the emitted RF signal very far, suggesting to use another PD with better EMC. Figure 3.12(c) shows the measurement from two different PDs when an 8 dBm RF signal was applied to the IDT at 490 MHz. Now with the new Discovery PD (PD-40GHz Discovery LabBuddy), the antenna signal did not appear suggesting better EMC. Additionally, the noise floor goes down due to the higher sensitivity of the new PD. Figure 3.12(d) presents the measured antenna signal power with respect to the driving RF frequency (at 10 dBm input power). This shows that the antenna signal is frequency-dependent. While the Discovery PD was able to quench much of the antenna signal, for some frequencies (280-380 MHz) these signals still persisted, albeit much weaker. Anyhow, these signals do not impact the heterodyne measurement because the modulation peaks appear away ($\pm$ 200 MHz) from the driving RF frequency. In the homodyne measurement, these signals can be measured without the light input and later can be subtracted from the modulation spectrum.

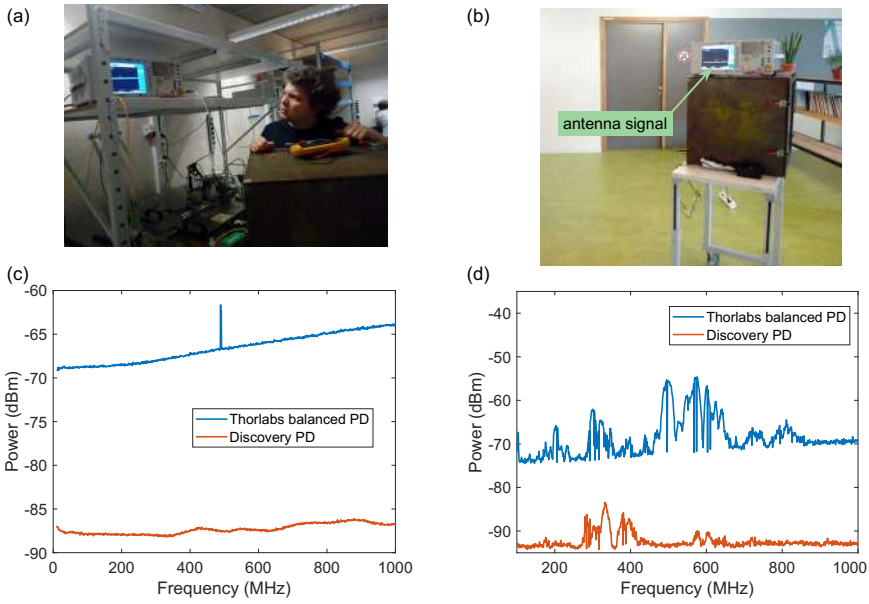

Figure 3.12: Troubleshooting the antenna signal (a) EXA showing the antenna signal detection without the light input (b) antenna signal measured even away from the setup (in photonics hub) without any light input to the balanced PD (c) measurement with different PD (d) antenna signal spectrum with respect to the driving RF frequency from two different PDs.

3.3.2 Modulation measurement

Finally, after solving the measurement issues, with the revised setup (containing the Santec laser and the Discovery PD), the heterodyne measurement was carried out on different DUTs.

Figure 3.13(a) shows the output power spectrum when an IDT with period 12 μm is actuated with a 15 dBm RF signal at 576 MHz. As described in equation 3.4, the peak at 200 MHz corresponds to the AOM driving frequency and the two sidebands of the carrier, at 576 $\pm$ 200 MHz, result from the acousto-optic modulation. To characterize the modulation strength, we measured the amplitude of the upper sideband peak with respect to the applied RF frequency, for different IDTs, as shown in figure 3.13(b), (c), and (d).

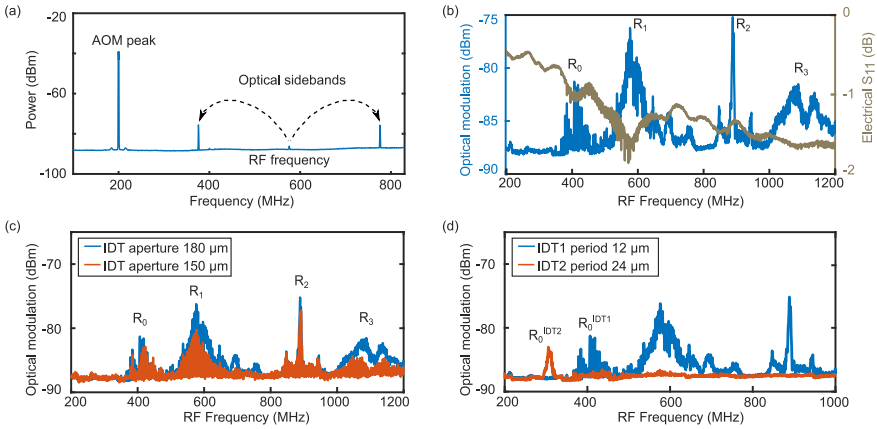

Figure 3.13: (a) Measured output spectrum for IDT with period 12 μm actuated with a 15 dBm RF signal at 576 MHz, showing the carrier peak at the AOM driving frequency (200 MHz) and optical sidebands at 576 $\pm$ 200 MHz. (b) Frequency-dependent modulation spectrum (blue) and S_{11} (brown) for IDT with period 12 μm. The S_{11} spectrum shows a dip at 410 MHz and 576 MHz, while the measured optical modulation spectrum shows peaks at 410 MHz, 576 MHz, 888 MHz, and 1088 MHz. (c) Modulation spectra for IDT with aperture 180 μm and 150 μm. (d) Modulation spectra for IDT1 (with period of 12 μm, aperture 180 μm, 20 finger-pairs), placed 6 μm away from the waveguide, and IDT2 (with period 24 μm, aperture 280 μm and 30 finger-pairs), placed 1024 μm away from the waveguide.

In figure 3.13(b), we compare the results from the optical modulation measured in the waveguide and the electrical S_{11} measured on the corresponding IDT (with period 12 μm and aperture 180 μm). We notice that the optical modulation peaks at 410 MHz and 576 MHz are consistent with the transduction dips in the electrical S_{11} response. For the modulation peaks at 888 MHz and 1088 MHz, however, we do not see clear dips in the S_{11} signal. We suspect this might be due to the additional noise or cross-talk at higher RF frequencies in the S_{11} measure-

ment. Thus, both the electrical and optical measurements confirm the excitation of acoustic waves and corresponding optical phase modulation in the waveguide.

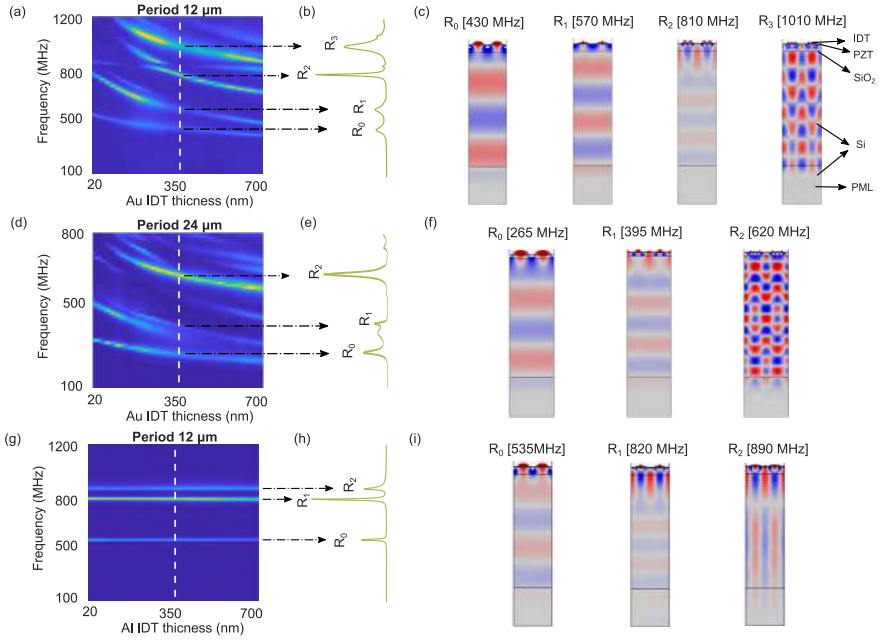

Figure 3.14: FEM calculated acoustic dispersion diagram with respect to the IDT thickness from a unit cell of (a) 12 μm period Au IDT, (d) 24 μm period Au IDT and (g) 12 μm period Al IDT. The color map represents normalized elastic strain energy. (b), (e) and (h) show the elastic strain energy spectrum plotted for 350 nm IDT thickness. (c), (f) and (i) show the vertical-displacement profile of the corresponding modes for a 350 nm thick IDT. For the simulation details see the appendix B.2

In figure 3.13(c), we show the modulation spectra from devices with IDT aperture 180 μm and 150 μm. As expected, we see a proportional increment in the modulation strength when the modulation length (IDT aperture) is increased. In figure 3.13(d), we show the modulation spectra from devices with two different IDT periods. The spacing between the IDT aperture and the waveguide core edge is 6 μm for IDT1 (period 12 μm, 20 finger-pairs) and 1204 μm for IDT2 (period 24 μm, 30 finger-pairs). In the latter case (IDT2), the modulation spectrum shows only one peak while for IDT1 multiple peaks are visible. To understand this and get insight into the characteristics of the acoustic modes corresponding to these peaks, we carried out a detailed FEM simulation on a unit cell of the IDT, assuming periodic boundary conditions. The details of the simulation setup are discussed in the appendix B.2.

Figure 3.14 shows the main results. In figure 3.14(a) we show the acoustic mode dispersion with respect to the thickness of an Au IDT (period 12 μm). Fig-

ure 3.14(b) shows the elastic energy spectrum for a PZT thickness of 350 nm indicating 4 peaks, and the associated mode profiles are shown in figure 3.14(c). We note that R_0 at 430 MHz, R_1 at 570 MHz, R_2 at 810 MHz and R_2 at 1010 MHz correspond to the fundamental SAW mode, a pseudo-SAW mode, a leaky-SAW mode, and a leaky mode. These can be linked to the peaks observed in the experimental spectrum shown in figure 3.13(c) at 410 MHz, 576 MHz, 888 MHz, and 1088 MHz for IDT1. The small deviation between experimental and simulated results can be attributed to a slight mismatch in the geometric and material parameters used in the simulation and the real experiment. Additionally, the Si tiling pattern on the chip (see figure 3.7) was not included into the simulation.

Similarly, figure 3.14(f), where the period was increased to 24 μm, shows the excitation of 3 main modes, whereby R_0 at 265 MHz, R_1 at $\sim$ 395 MHz and R_2 at 620 MHz correspond to the fundamental SAW mode, a pseudo-leaky SAW mode, and a leaky mode respectively. Given the leaky character of R_1 and R_2, only R_0 can travel a longer distance, explaining why we observed only a single modulation peak in figure 3.13(d) for IDT2.

From the acoustic dispersion diagrams shown in figure 3.14 (a) and (d), we notice that when the IDT thickness is negligible, there are three main modes excited: the fundamental SAW mode, a leaky-SAW mode, and higher order (weak) SAW mode. However, when we increase the IDT thickness, the added mass-loading and grating reflection decrease the mode frequencies and introduce more leaky modes. While the mass-loading effect from the IDT can be desirable for some sensing applications [8], in our case, it is undesirable as it weakens the SAW transduction strength and diffracts more energy into the substrate. As a result, the acousto-optic interaction in a waveguide in the surface layer gets weaker. To solve the problem of grating reflection, in some cases, a split-finger IDT is used [9, 10], because the reflected waves from the grating then add up destructively. However, in the case of periodic poling, this condition is not satisfied. Therefore, in our case, thinner and lower-density metal electrodes could be a possible solution.

In figure 3.14(g), we show the acoustic dispersion diagram for an Aluminum IDT, which has a low density (density $\sim$ 1/7 of Au) and lower acoustic impedance mismatch. Now we do not see any shift in the mode frequencies.

Therefore, in the next progression of fabrication, we used Al IDT on top of the photonics chip. We used electron-beam lithography to pattern a small period IDT, which allows the excitation of higher (GHz) frequency acoustic waves. We deposited 100 nm thick Al using e-gun evaporation, followed by a metal lift-off process. Then, we patterned additional contact pads with photo-lithography, followed by a $\sim$ 330 nm thick Al deposition and lift-off process. Finally, we covered the top of the device with a 50 nm Al_2O_3 layer using atomic-layer deposition (ALD). An example of the resulting devices is shown in the inset of figure 3.15.

Figure 3.15 shows the modulation spectrum measured from a 100 nm thick

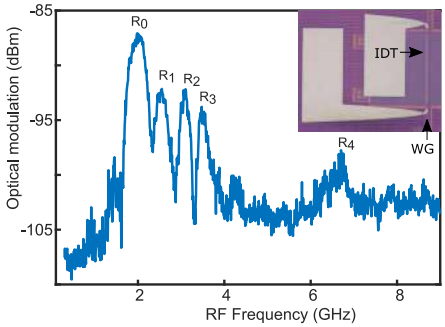

Figure 3.15: Measured optical modulation spectrum for an Al IDT with 4 finger-pairs, period 2 μm (finger-width 500 nm) and aperture length 70 μm, actuated with 12 dBm RF power. The spectrum shows modulation peaks at 2 GHz (R_0), 2.55 GHz (R_1), 3.1 GHz (R_2), 3.47 GHz (R_3) and 6.7 GHz (R_4). The inset shows a microscope image of the fabricated device, which was spaced 2 μm from the waveguide in a region without Si tiling.

Al IDT with period 2 μm driven with 12 dBm of RF power. We find modulation peaks at 2 GHz (R_0), 2.5 GHz (R_1), 3.1 GHz (R_2), 3.5 GHz (R_3) and 6.7 GHz (R_4). From an FEM simulation, we conclude the first and the strongest modulation peak (R_0) to be the fundamental SAW mode [11] while the other peaks belong to higher-order modes.

In figure 3.16 (a) and (b), we show how the modulated power depends on the input laser power and the RF driving power respectively. These measurements were done on the IDT of period 12 μm at an RF frequency of 576 MHz. The slopes obtained from a linear fit of the data are very close to the expected values (1 and 2 respectively) as discussed in equation 3.6. The small deviation is attributed mainly to the higher order terms in the phase modulation, which are not negligible anymore at higher RF power and poor signal-to-noise ratio at lower optical power.

From comparing the AOM peak (-39.15 dBm) and the modulation peak (-75.60 dBm) in figure 3.13(a), we extract the phase modulation amplitude $\alpha(L)$ using equation 3.5. We obtained $\alpha(L)$ to be $\approx 0.03\ rad$, when the Au IDT with period 12 μm, 20 finger pairs and aperture of 180 μm is actuated with 15 dBm RF power at 576 MHz. The corresponding V_πL is $\approx$ 3.35 V·cm. Similarly, for the Al IDT of period 2 μm and aperture 70 μm, the modulation peak at 2 GHz (R_0) was measured to be at -87.3 dBm (figure 3.15), while the AOM peak was noted at -43.5 dBm. This gives $\alpha(L) \approx 0.0077\ rad$ and the corresponding V_πL to be $\approx$ 3.60 V·cm. This is a significant improvement, considering that the Al IDT now consists of only 4 finger pairs. While we believe the main reason for this improvement is a low mass-loading and grating reflection from the Al IDT, as discussed above, the other contributing factors could be the absence of the Si tiling pattern and a stronger acousto-optic overlap in the waveguide (width 0.45 μm) from the acoustic wave

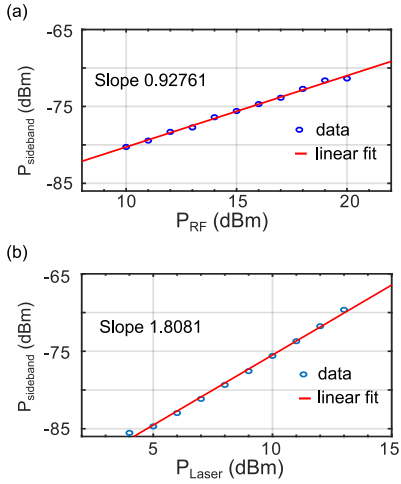

Figure 3.16: Modulated power (sideband peak) dependence on, (a) the driving RF power at a fixed laser input of 10 dBm, and (b) the laser power at a fixed RF power of 15 dBm. The measurement was done on the IDT of period 12 μm at an RF frequency of 576 MHz

(wavelength $\sim 1\mu$m).

With a similar PZT layer, a modulator exploiting the electro-optic (EO) effect has been reported to exhibit V_πL $\approx$ 3.2 V·cm [12]. In [13], using a Si waveguide integrated with AlN and an IDT consisting of 107 finger-pairs actuated at 3.11 GHz, the V_πL was reported to be 1.8 V·cm. Thus, our figures of merit are competitive to state-of-the-art electro-optic and acousto-optic modulators integrated on Si PICs

3.4 Conclusion

We investigated the piezo-electrical actuation of SAWs using a photonic-compatible PZT film. During the electrical characterization, we found out the importance of poling the polycrystalline PZT film for an efficient SAW actuation. Hence, all the subsequent PZT films were poled, and we demonstrated the SAW actuation. Then, we integrated a PZT thin film on a planarized SOI photonic chip to induce acousto-optic modulation in a waveguide with MHz acoustic waves. Through FEM analysis, we pointed out the issue of mass-loading and grating reflection from the Au IDT used in the device. We then fabricated a new device with an Al IDT and a smaller period to actuate GHz acoustic waves. We obtained a competitive V_πL $\approx$ 3.6 V·cm with an Al IDT consisting of only 4 finger-pairs, without patterning the PZT layer or under-etching the device. Further improvements in the device performance are expected when the scattering and damping loss factors are eliminated.

For instance, the IDT design can be optimized to match the electrical impedance, thus minimizing the RF power reflection. Additionally, the current bi-directional IDT actuates the acoustic waves in both directions, thus, only half of the acoustic energy is utilized for the modulation. We can define an acoustic reflector to collect the other half or design a unidirectional SAW actuator [14, 15]. Furthermore, the device could be under-etched to avoid leakage of any acoustic energy into the substrate and any interference from the bulk acoustic waves. The under-etching test is reported in chapter 5.

3.5 Additional information

3.5.1 Acousto-optic interaction

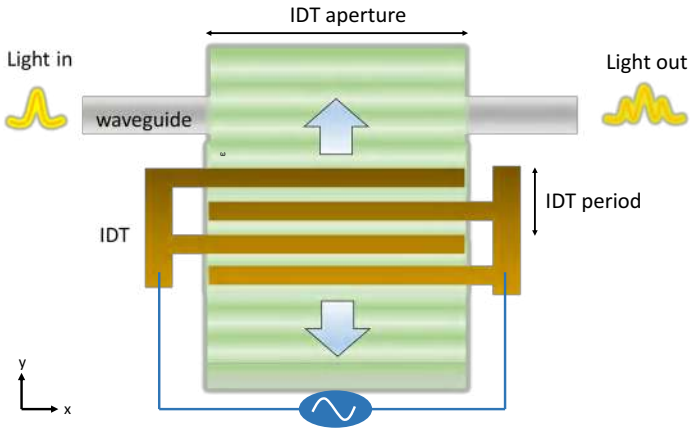

Figure 3.17: The IDT actuated acoustic beam (Ω) diffracts the input waveguide mode (ω_0) into two sidebands ($\omega_0 \pm \Omega$). The wavelength of the fundamental SAW mode Λ= IDT period/2, for the PZT with the periodic (in-plane) domain orientation.

The electric field of a waveguide mode traveling along x is given by:

$$\psi(x,t) = A\Re e^{i(\omega_0 t - k_0 n_{eff}\, x)} \tag{3.7}$$

Where A is the electric field amplitude, ω_0 is the angular frequency, $k_0 = 2\pi/\lambda_0$ with λ_0 as the free space wavelength and $n_{eff}(\omega_0)$ is the effective refractive index of the waveguide mode. The index modulation in the waveguide material due to an acoustic wave traveling along y (as shown in figure 3.17) can be written as:

$$n(y,t) = n^0 + \Delta n \sin\big(\Omega(t - y/v_{ac})\big)$$

Where n^0 is the material index without any modulation, Δn is the index change due to the modulated strain from the elastic wave (photoelastic effect). Ω and v_{ac}

are the angular frequency and the phase velocity of the acoustic wave respectively. These material indices determine the effective index of the waveguide mode, which can be approximated as,

$$n_{eff}(t) = n^0_{eff} + \Delta n_{eff} \sin(\Omega\, t) \tag{3.8}$$

where n^0_{eff} is the effective index without any perturbation and Δn_{eff} is the amplitude of the effective index change due to the acousto-optic interaction. Δn_{eff} depends on the overlap integral between the strain-field and the optical-field [16]. From the photoelastic effect, Δn_{eff} can be calculated as:

$$\Delta n_{eff} = \frac{n^3_{eff}}{2} \frac{\int_D E^* \boldsymbol{pS}\, E\, dr}{\int_D E^* E\, dr} \tag{3.9}$$

Here D is the 2D cross-section of the waveguide, E is the electric field of the waveguide mode, $\boldsymbol{p}$ is the photoelastic tensor of the waveguide medium and $\boldsymbol{S}$ is the strain field induced by the acoustic wave.

We assume the modulator length is small, so the spatial variation in n_{eff} along the modulator (x-direction) is negligible as $\Omega\, \Delta t = \Omega\, L/v_p << 1$, where v_p is the light phase velocity. Thus, considering no attenuation, the waveguide mode propagating through the modulator can be written as:

$$\psi(x,t) = A\Re e^{i(\omega_0 t - k_0\, n^0_{eff}\, x)} e^{-ik_0\, x \Delta n_{eff} \sin(\Omega\, t)}$$

$$\psi(x,t) = A\Re e^{i(\omega_0 t - k_0\, n^0_{eff}\, x)} e^{i\alpha(x) \sin(\Omega\, t)} \tag{3.10}$$

Where $\alpha(x) = -k_0 \Delta n_{eff} x$ is the modulated phase amplitude. The sinusoidal phase term here can be expanded in terms of the Bessel functions (J_N) $\Longrightarrow$ $e^{i\alpha \sin(\Omega\, t)} = \sum_{-\infty}^{\infty} J_N(\alpha) e^{iN\Omega t}$, where N is an integer. Hence, we get the following expression:

$$\begin{aligned} \psi(x,t) = A\Re\, e^{i(\omega_0 t - k_0\, n^0_{eff}\, x)} \Big[J_0(\alpha(x)) \\ + \sum_{N=1}^{\infty} J_N(\alpha(x)) \left[e^{iN\Omega t} + (-1)^N e^{-iN\Omega t} \right] \Big] \end{aligned} \tag{3.11}$$

If the modulator length and Δn_{eff} are assumed to be small, the phase modulation $\alpha(x) << 1$. Hence, the Bessel function can be simplified as, $J_N(\alpha(x)) \approx \alpha(x)^N/(2^N N!)$. Therefore, neglecting the higher-order terms in the above equation,

$$\begin{aligned} \psi(x,t) = A\Re\, e^{-ik_0\, n^0_{eff}\, x} \Big[e^{i\omega_0 t} \\ + \frac{\alpha(x)}{2} \left[e^{i((\omega_0+\Omega)t} - e^{i((\omega_0-\Omega)t} \right] \Big] \end{aligned} \tag{3.12}$$

We see that as the carrier mode propagates along the modulator, it is diffracted into Stokes and Antistokes sidebands with frequencies $\omega_0 \pm \Omega$. The phase obtained by the Antistokes wave generated at $x = 0$ accumulated over the modulation length L is then:

$$\begin{aligned} \phi_A &= (\omega_0 + \Omega)t_1 \\ &= (\omega_0 + \Omega)\frac{L}{v_p(\omega_0 + \Omega)} \\ &= (\omega_0 + \Omega)\frac{n_{eff}(\omega_0 + \Omega)L}{c} \end{aligned} \tag{3.13}$$

The phase of an Antistokes wave scattered at the end of the modulator on the other hand equals the phase obtained by the carrier wave over the modulation length L:

$$\begin{aligned} \phi_c &= \omega_0 t_2 \\ &= \omega_0 \frac{L}{v_p(\omega_0)} \\ &= \omega_0 \frac{n_{eff}(\omega_0)L}{c} \end{aligned} \tag{3.14}$$

Hence, the phase difference built-up between these Antistokes sidebands scattered at the beginning ($x = 0$) and the end of the modulator ($x = L$):

$$\begin{aligned} \Delta\phi_L &= \phi_A - \phi_c \\ &= \frac{L}{c}\Big[(\omega_0 + \Omega)\, n_{eff}(\omega_0 + \Omega) - \omega_0\, n_{eff}(\omega_0)\Big] \\ &= \frac{L\,\omega_0}{c}\Big[n_{eff}(\omega_0 + \Omega) - n_{eff}(\omega_0) \\ &\qquad + \frac{\Omega}{\omega_0}\, n_{eff}(\omega_0 + \Omega)\Big] \end{aligned} \tag{3.15}$$

Since $\Omega << \omega_0, \implies \Omega/\omega_0 \to 0$.

Also, $n_{eff}(\omega_0 + \Omega) - n_{eff}(\omega_0) \to \Omega \frac{\partial n_{eff}}{\partial \omega}\Big|_{\omega=\omega_0}$

Therefore,

$$\begin{aligned} \Delta\phi_L &= L\, k_0\, \Omega \frac{\partial n_{eff}}{\partial \omega}\bigg|_{\omega=\omega_0} \\ &= L\,\Omega\,\frac{\partial k}{\partial \omega}\bigg|_{\omega=\omega_0} \\ &= L\,\Omega/v_g(\omega_0) \end{aligned} \tag{3.16}$$

As long as L is small enough, this phase difference is negligible ($\Delta\phi_L << \pi$), and the diffracted signals will add up constructively producing a carrier peak

and two (modulated) sideband peaks in the output spectra. This is reminiscent of Raman-Nath diffraction of a light beam in free space due to an elastic beam propagation [10].

For our modulators $\Delta\phi_L$ was indeed negligible. For instance, with an IDT of aperture length (L) 180 μm and acoustic wave frequency (Ω) 576 MHz, $\Delta\phi_L$ was estimated to be $\approx 0.008 << \pi$. We used $v_g(\omega_0) \approx 1.3$ x 10^7 m/s calculated from the single mode (TE00) dispersion relation which was obtained with the Comsol mode solver.

It is noteworthy that a high phase modulation ($\alpha(L)$) can be achieved by designing a cascaded modulator system. For example, a serpentine waveguide structure can be designed next to the IDT to allow multiple (smaller) interaction lengths [13, 17]. Hence, the net phase modulation accumulated over the total interaction lengths can be very high, while the phase-mismatch ($\Delta\phi_L$) in the individual sections remains negligible.

References

[1] David Morgan. *Surface acoustic wave filters: With applications to electronic communications and signal processing*. Academic Press, 2010.

[2] PV Wright. *A review of SAW resonator filter technology*. In IEEE 1992 Ultrasonics Symposium Proceedings, pages 29–38. IEEE, 1992.

[3] *Lithium Niobate Properties*. `http://www.roditi.com/SingleCrystal/LiNbO3/liNBO3-Properties.html`. URL Accessed: 2023-03-01.

[4] J. P. George, P. F. Smet, J. Botterman, V. Bliznuk, W. Woestenborghs, D. Van Thourhout, K. Neyts, and J. Beeckman. *Lanthanide-Assisted Deposition of Strongly Electro-optic PZT Thin Films on Silicon: Toward Integrated Active Nanophotonic Devices*. ACS Applied Materials & Interfaces, 7(24):13350–13359, 2015.

[5] Markus Kratzer, Michael Lasnik, Sören Röhrig, Christian Teichert, and Marco Deluca. *Reconstruction of the domain orientation distribution function of polycrystalline PZT ceramics using vector piezoresponse force microscopy*. Scientific Reports 2017 8:1, 8(1):1–11, jan 2018.

[6] *IEEE Standard on Piezoelectricity*. ANSI/IEEE Std 176-1987, pages 0_1–, 1988.

[7] Zubair Butt, Riffat Asim Pasha, Faisal Qayyum, Zeeshan Anjum, Nasir Ahmad, and Hassan Elahi. *Generation of electrical energy using lead zirconate titanate (PZT-5A) piezoelectric material: Analytical, numerical and experimental verifications*. Journal of Mechanical Science and Technology, 30(8):3553–3558, 2016.

[8] Zhe Chen, Jian Zhou, Hao Tang, Yi Liu, Yiping Shen, Xiaobo Yin, Jiangpo Zheng, Hongshuai Zhang, Jianhui Wu, Xianglong Shi, et al. *Ultrahigh-frequency surface acoustic wave sensors with giant mass-loading effects on electrodes*. ACS sensors, 5(6):1657–1664, 2020.

[9] Antonio Crespo-Poveda, R Hey, K Biermann, A Tahraoui, PV Santos, B Gargallo, P Muñoz, A Cantarero, and MM de Lima. *Synchronized photonic modulators driven by surface acoustic waves*. Optics express, 21(18):21669–21676, 2013.

[10] Daniel Royer and Eugene Dieulesaint. *Elastic waves in solids II: generation, acousto-optic interaction, applications*. Springer Science & Business Media, 1999.

[11] Irfan Ansari, Dries Van Thourhout, John P. George, Gilles F. Feutmba, and Jeroen Beeckman. *Acousto-optic modulation in a Si-waveguide*. In 2021 IEEE 17th International Conference on Group IV Photonics (GFP), pages 1–2, 2021.

[12] Koen Alexander, John P. George, Jochem Verbist, Kristiaan Neyts, Bart Kuyken, Dries Van Thourhout, and Jeroen Beeckman. *Nanophotonic Pockels modulators on a silicon nitride platform*. Nature Communications, 9(1):4–9, 2018.

[13] Eric A. Kittlaus, William M. Jones, Peter T. Rakich, Nils T. Otterstrom, Richard E. Muller, and Mina Rais-Zadeh. *Electrically driven acousto-optics and broadband non-reciprocity in silicon photonics*. Nature Photonics, 15:43–52, 1 2021.

[14] Maria K. Ekström, Thomas Aref, Johan Runeson, Johan Björck, Isac Boström, and Per Delsing. *Surface acoustic wave unidirectional transducers for quantum applications*. Applied Physics Letters, 110(7):073105, 2017.

[15] E. Dumur, K. J. Satzinger, G. A. Peairs, Ming-Han Chou, A. Bienfait, H.-S. Chang, C. R. Conner, J. Grebel, R. G. Povey, Y. P. Zhong, and A. N. Cleland. *Unidirectional distributed acoustic reflection transducers for quantum applications*. Applied Physics Letters, 114(22):223501, 2019.

[16] Linbo Shao, Mengjie Yu, Smarak Maity, Neil Sinclair, Lu Zheng, Cleaven Chia, Amirhassan Shams-Ansari, Cheng Wang, Mian Zhang, Keji Lai, and Marko Lončar. *Microwave-to-optical conversion using lithium niobate thin-film acoustic resonators*. Optica, 6(12):1498–1505, Dec 2019.

[17] Dvir Munk, Moshe Katzman, Mirit Hen, Maayan Priel, Moshe Feldberg, Tali Sharabani, Shahar Levy, Arik Bergman, and Avi Zadok. *Surface acoustic wave photonic devices in silicon on insulator*. Nature Communications, 10(1):4214, dec 2019.

4

PZT based MEMS-actuator

In this chapter, the fabrication and characterization of PZT based micro-electro-mechanical system (MEMS) actuators are presented. The MEMS actuators were driven with an RF signal, and their deflection was measured. The deflection results further corroborated the piezoelectric actuation of our PZT film. Finally, to integrate the PZT film on a non-planarized chip or to obtain complex MEMS designs, micro-transfer printing of the PZT film was explored.

4.1 Fabrication of the MEMS device

Fabrication of the suspended MEMS structure requires multiple process steps as shown in figure 4.1. These steps were optimized as discussed in chapter 2. For the preliminary test, we suspended a simple PZT on Si beam structure, with electrodes on top. In the first step, a standard SOI substrate with 220 nm Si layer was thoroughly cleaned, dehydrated and treated with O_2 plasma for 15-20 min. Then 400 nm thick PZT film was deposited on the SOI substrate using chemical solution deposition (CSD) method as described in chapter 2 [1]. Al electrodes were patterned with optical lithography followed by e-gun evaporation and a lift-off process. Next, a thicker TI 35E resist-mask was spin-coated and patterned with optical lithography. The sample was loaded in an RIE tool to etch through the PZT and Si layer to obtain the underetch windows. Thereafter, the photoresist mask was dissolved in AZ 100 remover, followed by acetone and IPA cleaning. The sample was dehydrated for 10-15 min on a hotplate at 150 °C. The sample was

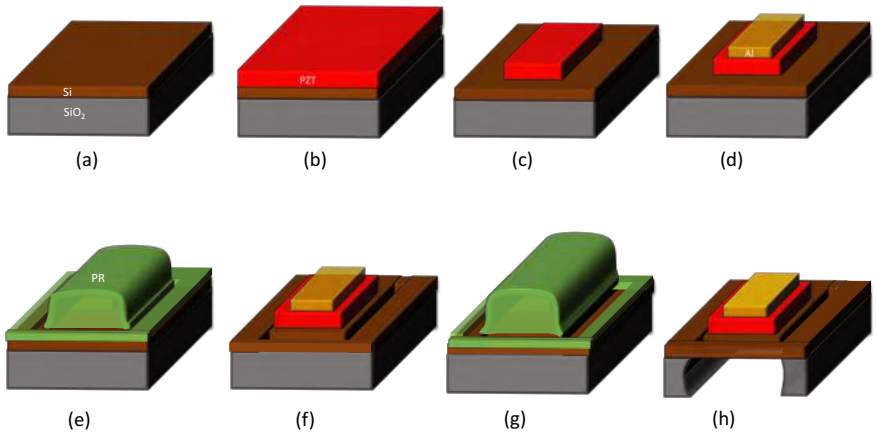

Figure 4.1: Fabrication process steps for a typical MEMS device (a) cleaned SOI substrate, (b) PZT film deposition, (c) PZT film patterning with RIE, (d) electrode fabrication (e) underetch window patterning using a photoresist mask, (f) etching through PZT/Si in the underetch window pattern (g) patterning of the protection mask on the sensitive region of the device (h) under-etching process to release the PZT/Si structure.

then loaded in an Idonus VPE 100 reactor to start the underetching process. Given the poor visibility of the etched oxide through the 400 nm PZT film, a blank SOI sample (without PZT) was processed simultaneously as a control sample. After each exposure step, the undercut oxide was monitored by observing this control sample through the microscope. This process was repeated until the widest beam on the control sample looked fully suspended, as shown in figure 4.2 (a). Figure 4.2 (b) shows the same PZT/Si beam after the release process.

As shown in figure 4.3 (a), several suspended beams were connected to the same contact pad. This was done to increase the number of suspended beams and vary the beam parameters. To confirm the full suspension of the PZT/Si beam, a cross-section was made on one of the widest beams, shown in figure 4.3(b). The SEM image of the cross-section is shown in figure 4.3 (c). This confirmed the full release of the PZT/Si beam.

4.2 LDV setup

To characterize the MEMS devices, a dedicated setup was built as shown in figure 4.4. The device was driven with an RF signal from a Rhodes & Schwarz-SMR40 signal generator. The resulting deflection/vibration was measured with a commer-

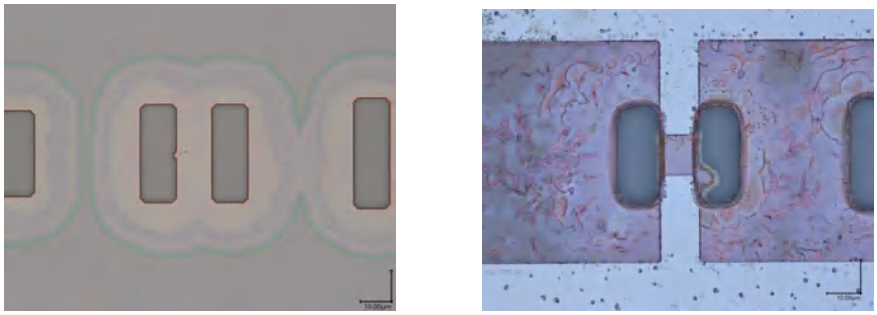

(a) (b)

Figure 4.2: Undercut visibility through a microscope (a) control SOI sample (b) test PZT/SOI sample.

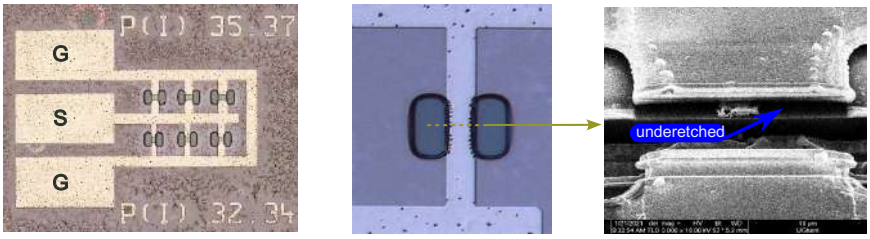

(a) (b) (c)

Figure 4.3: (a) Fabricated device containing multiple beams connected to the electrode pads in GSG configuration (ground-signal-ground), (b) image of a single beam, (c) cross-section of a fully suspended beam.

cial Laser Doppler vibrometry (LDV) system[1] from Polytec [2]. The LDV system consisted of an OFV-534 sensor head, an OFV-500 modular vibrometer, and a VD06 decoder. The LDV sensor head contained a He-Ne laser to emit a visible probe light (632 nm). Using the integrated lens in the LDV head, the emitted beam was focused to a small spot size of a diameter up to 25 μm, at a working distance of 20 cm. The laser spot and the DUT were monitored using a CCD camera connected to a computer screen. The camera exposure time was set high to locate the DUT on the chip. That particular location was marked on the screen with a whiteboard marker. Then the camera exposure time was reduced to be able to see the (localized) laser spot. Now, using the positioner attached to the LDV head, the laser spot was slowly moved to align with the marked position (on the screen). When the probe light hits the vibrating DUT, the reflected signal experiences a frequency shift (f_D) due to the Doppler effect. $f_D = 2 \cdot v/\lambda$, where v is the vibra-

[1]The LDV system setup was assisted by Emiel Dieussaert and Yanlu Li.

tion velocity and λ is the wavelength (632 nm) of the probe light. This frequency shift was measured with a heterodyne interferometer built inside the head sensor. Thus, the LDV vibrometer reads out the velocity of the vibrating surface, which was used to calculate the displacement/deflection of the DUT. The analog velocity signal from the vibrometer was sampled with a high-speed data acquisition (DAQ) digitizer, GaGe Octopus express CSE8385, which had a sampling rate of up to 65 million sampling per second (MS/s).

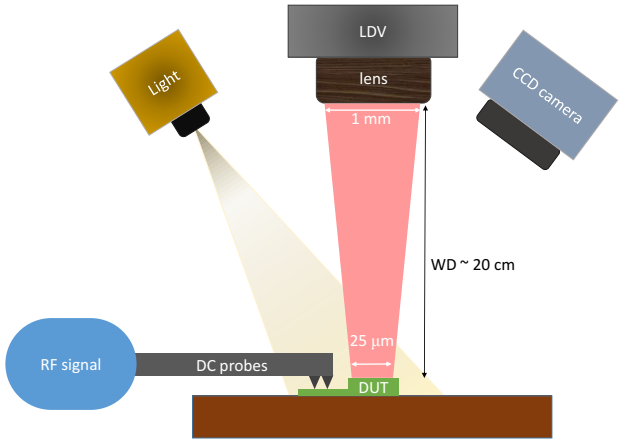

(a)

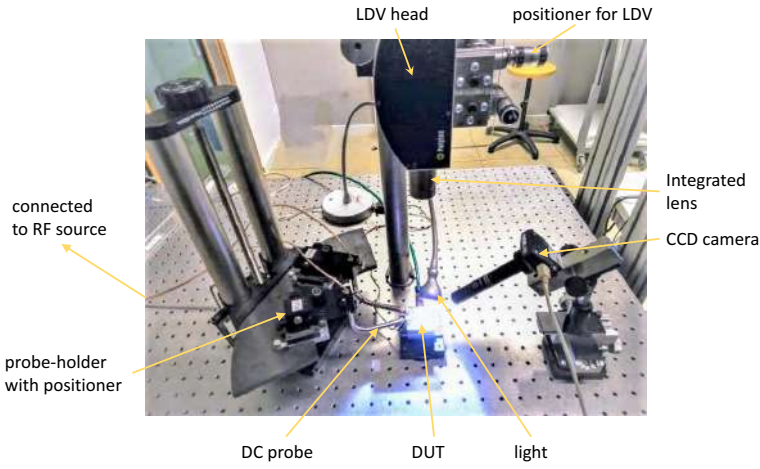

(b)

Figure 4.4: (a) Schematic of the setup (b) an image of the actual setup.

The GaGe digitizer came with a Matlab software development kit (SDK), enabling its operation via programming. Hence, the measurement setup was automated with a Matlab script described in appendix C. The script was written according to the signal analysis flow as shown in figure 4.5.

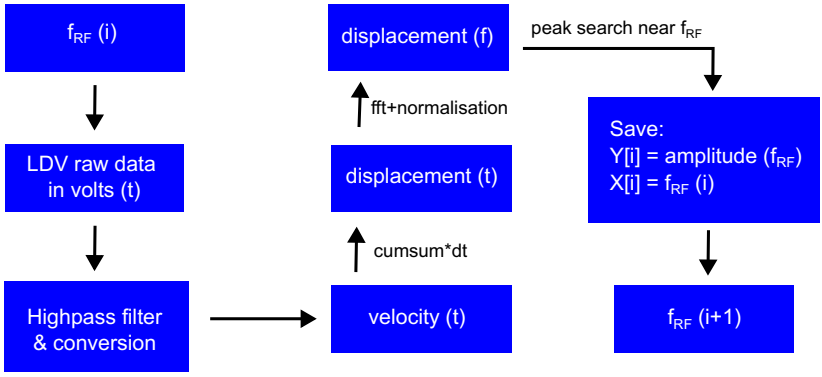

Figure 4.5: Signal analysis flow

An example of the signal processing is presented in figure 4.6. At a given driving RF frequency (1.15 MHz here), initially, a time-dependent voltage signal (raw data) was obtained. After applying a high pass filtering (f_{pass} = 500 kHz), and multiplying with the conversion coefficient (100 mm/s/V for the vibrometer used), we get the velocity signal v(t) as shown in figure 4.6(a). Now, the velocity signal was converted into the displacement signal using y(t) = $\sum v(t) \cdot \Delta t$. Here, the time step $\Delta t = 1/f$, where f is the sampling rate. Due to the summation process, the noise in the data was averaged out, resulting in a cleaner displacement signal as shown in figure 4.6(b). A fast Fourier transformation (FFT) on the displacement signal gives the amplitude spectrum, as shown in figure 4.6(c). Finally, the vibration amplitude of the DUT is obtained using a peak search function near the applied RF frequencies. These steps were repeated for each driving RF frequency to get a frequency-dependent amplitude spectrum.

Note that the size of the (focused) laser spot is roughly the same order or larger than the suspended beam structures. Hence, the measured deflection is an average deflection over the spot area. Nevertheless, considering the Gaussian distribution of the laser, the majority of the contribution comes from the deflection at the center position of the laser spot. Therefore, the LDV measurement can still provide a qualitative understanding of the deflection from the laser spot position.

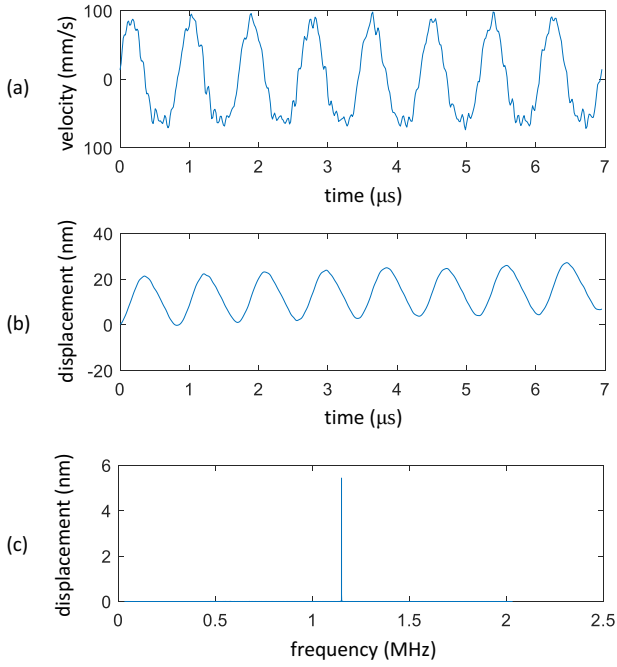

Figure 4.6: (a) Time domain velocity data of a DUT driven with an RF signal of frequency 1.15 MHz, after high-pass filtering (f_{pass} 500 kHz) (b) time domain displacement data, (c) frequency domain amplitude data after FFT and normalization.

4.3 Measurement results

The first measurement was carried out on a suspended beam (length 26 μm and width 8 μm) with the as-deposited PZT film. Figure 4.7 (a) shows the measured amplitude spectrum when the beam was actuated with an RF signal of V_{pp} = 10V. The measurement was carried out on 3 positions on the beam (up, center, and down). The spectrum showed the fundamental resonance of the beam was around 1.25 MHz. The deflection at the center point of the beam was lower than that on the edges (up and down positions). This was expected because the as-deposited PZT film had preferential domain orientation out of the substrate plane, while the applied electric field was in-plane. Thus, the transversal driving field (owing to d_{31}) actuated a shear mode vibration in the beam. This can be seen in the finite element method (FEM) simulation of the beam as shown in figure 4.7(b). In the simulation, the beam was piezoelectrically actuated with an RF signal of V_{pp} = 10V at 1 MHz.

Thereafter, a sufficiently high DC voltage was applied to the electrodes for

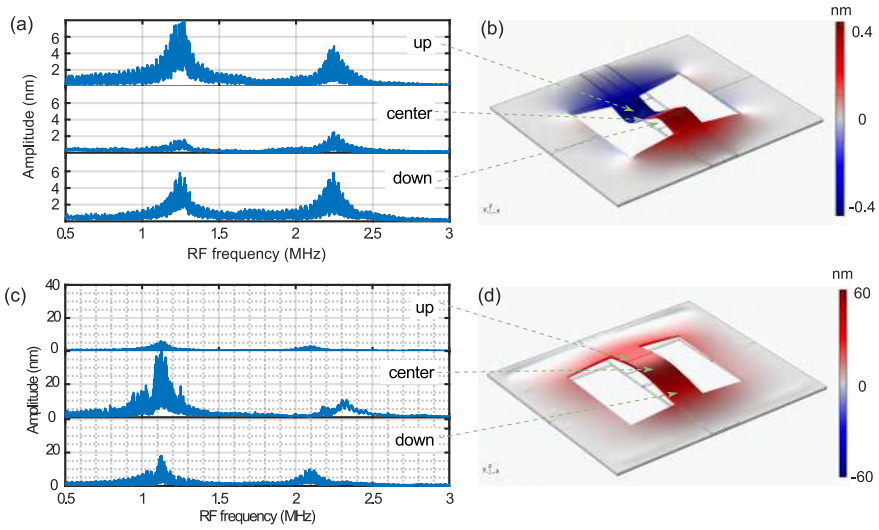

Figure 4.7: (a) Measured deflection spectrum of the as-deposited PZT/Si beam (dimension 26 $\mu m \times 8\ \mu m$) with V_{pp} = 10V, (b) a 3D FEM simulation of the PZT (c-orientation) on Si beam showing a shear mode upon actuated with an RF signal with V_{pp} = 10V at 1 MHz,(c) measured deflection spectrum of the same beam after poling the PZT domains in-plane, (d) a 3D FEM simulation of the PZT (a-orientation) on Si beam showing a longitudinal mode upon actuated with an RF signal with V_{pp} = 10V at 1 MHz.

about 50 min. This was done to pole the ferroelectric domains in the PZT film along the applied electric field (in substrate-plane). Figure 4.7(c) shows the amplitude spectrum after the poling process. Now, the highest deflection was observed at the center point of the beam and the amplitude was an order higher compared to the shear mode. This was because the driving electric field along the PZT domain polarization (owing to d_{33}) actuated a tensile vibration mode as shown in the simulation figure 4.7(d). In the subsequent measurement, the PZT film was poled and the amplitude spectrum (at the center of the beam) was measured to find out the amplitude dependence of other parameters.

Figure 4.8 shows how the amplitude depends on the RF peak-to-peak voltage (V_{pp}). Figures (a) and (b) are the measurements at the two longitudinal resonance modes at 1.15 MHz and 2.33 MHz, respectively. The amplitude looks linearly proportional to the driving voltage, which is expected. The deviation in the data increases with V_{pp}. This could be due to the mechanical cross-talks between the suspended beams. The linear fit of the data from both resonance modes gave a similar slope. This suggested that the deflection efficiency could strongly depend on the beam shape.

Figure 4.9 presents the amplitude spectrum dependence on the beam geometries. The beams were driven with an RF signal of V_{pp} 10 V. Figure 4.9(a) shows

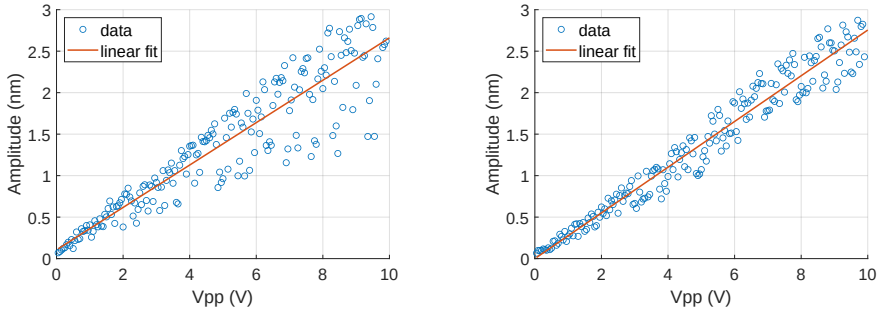

Figure 4.8: Amplitude dependence on V_{pp} for two resonance modes from PZT/Si beam (dimension 26 $\mu m \times 8\ \mu m$). (a) mode 1 driven at 1.15 MHz gives a slope of $\sim$ 0.25 nm/V (b) mode 2 driven at 2.33 MHz gives a slope of $\sim$ 0.27 nm/V .

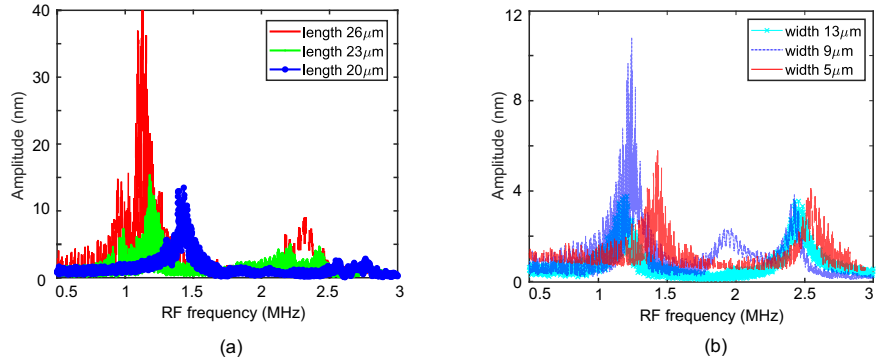

Figure 4.9: Amplitude dependence on the size of the PZT/Si beam measured at V_{pp} 10 V when (a) beam length was varied at fixed width $\sim 8\mu m$, (b) beam width was varied at fixed length$\sim 17\mu m$.

the amplitude spectrum with different lengths at a fixed width of 8 μm. As expected, when the beam length increases, the resonance frequency decreases and the amplitude increases [3, 4]. Whereas, in figure 4.9(b), the amplitude spectrum with different widths at a fixed length of 17 μm does not give a clear pattern.

4.4 Application of the PZT based MEMS actuators

The capability to actuate our PZT film was proven through the deflection measurement. This opens the possibility of integrating piezo-MEMS into the PIC. Figure 4.10 illustrates two simple actuator designs that can be employed for tuning the light coupling and n_{eff}. In figure 4.10(a) the electric field is applied via top-

bottom electrodes. Although such an actuator has already been demonstrated with the PZT layer grown using Pt buffer layer [5]. Our PZT, being optically transparent, provides extra flexibility to bring the PZT actuator next to the waveguide. This can reduce power consumption, and enhance the tuning effect. In figure 4.11(a), an FEM simulation of TE n_{eff} with respect to the z-position of an actuator is presented. A significant change in n_{eff} can be observed when the relative distance between the coupler was varied. Here, the separation between the coupler was 150 nm, and the width and the thickness of each waveguide were 400 nm and 220 nm respectively. The waveguides were considered to be defined through a 150 nm etching step on a 220 nm Si layer.

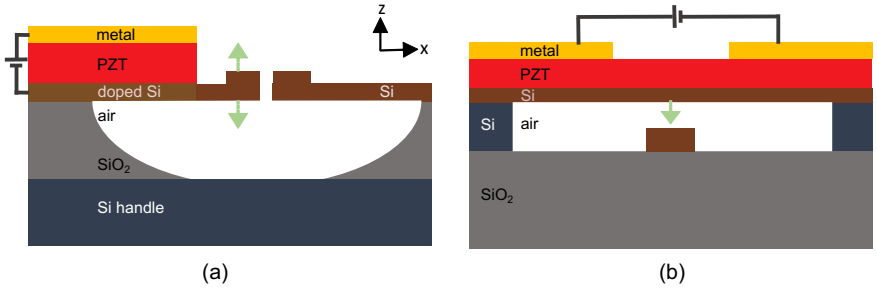

Figure 4.10: Example of piezo-MEMS configurations for photonics application (a) top-bottom electrode configuration connected with a side tuning coupler, (b) co-planer electrode configuration connected to a top tuning coupler.

In figure 4.10(b), another actuator configuration is presented, which is based on the suspended beam that was measured. Here the electric field is applied in-plane via a co-planar electrode pair. The deflection from the beam can be used for tuning the n_{eff} of the TE mode in the waveguide below. Figure 4.11(b) presents an FEM simulation of n_{eff} tuning with respect to the z-displacement of the actuator. Here, the initial separation between the top actuator and the waveguide was set to be 100 nm, and electrode-electrode spacing was 6 μm. The simulation shows that n_{eff} changes significantly in the beginning but after $\sim$ 200 nm, it starts saturating. This is because, after $\sim$ 200 nm, the actuator is too far to couple with the waveguide mode. Simulation results from these two configurations indicate that the top actuator configuration could be more efficient in tuning the TE waveguide mode.

Fabrication of the configurations described in 4.10 requires a good fabrication tolerance i.e. maintaining a certain separation (100-200 nm) between the active waveguide and the actuator. Considering these challenges, a simple side actuator design was incorporated in an MPW run. Figure 4.12(a) illustrates a graphical design system (GDS) drawing of the side actuator attached to the bus waveguide. Here, the doped Si was defined as the bottom electrode. The plan was to inkjet

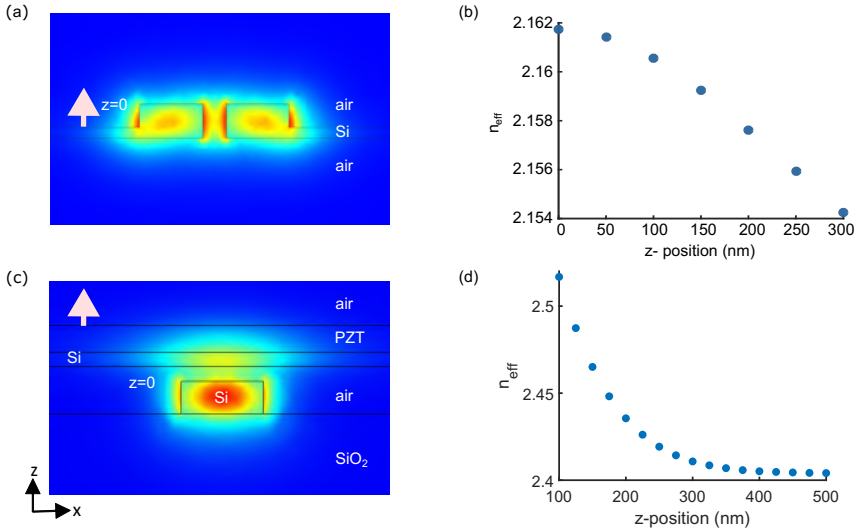

Figure 4.11: Mode simulation with respect to the displacement for different MEMS configurations. (a) mode profile with the side actuator configuration (b) simulated n_{eff} tuning with respect to the z-displacement of the side coupler waveguide (c) mode profile with the top actuator configuration (d) simulated n_{eff} tuning with respect to the z-displacement of the top actuator.

print PZT on the doped Si, and then a top electrode could be fabricated. For this post-processing purpose, a 'no fill' and 'expo' region were defined in the actuator region. However, the inkjet printing of the PZT film was not yet optimized for such a smaller region (<100 μm). And given that the MPW chip was not planarized (profile difference of up to 6 μm in the expo region), it was not possible to deposit PZT with the CSD process. As an alternative, the top actuator configuration, as shown in schematic 4.12(b) was considered. For such fabrication, the transfer printing technique could be an option.

4.5 PZT micro-transfer printing (μTP)

The surface uniformity of a chip is crucial to achieving a good quality PZT film through chemical solution deposition (CSD). If the surface profile of a substrate is not uniform, it needs planarization, which adds extra technological challenges. Micro-transfer printing (μTP) or inkjet printing of the PZT film provides an alternate route to evade this problem [6, 7]. The μTP process has been extensively studied in the photonics research group (PRG) to achieve heterogeneous integration of III-V optoelectronic components on low-loss SiN or Si platforms [8]. If the μTP process is developed for the PZT film, it can add several new functionalities

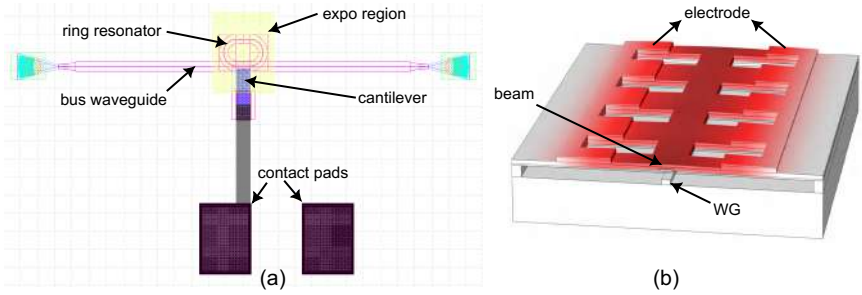

Figure 4.12: (a) A GDS design of an actuator (cantilever) attached with the bus waveguide. (b) a 3D schematic of a top-tuning actuator.

to the passive photonic platforms. Moreover, for certain MEMS configurations i.e. a top-down movement shown in figure 4.12(b), μTP can be a way to achieve that through heterogeneous integration of a PZT film atop an undercut design. In the following sections, a preliminary study on our PZT μTP is described.

4.5.1 Coupon preparation

The first challenge of μTP was to suspend long PZT coupons by under-etching the sacrificial layer. While the lower limit for the coupon size is determined by the lithography resolution and alignment error (through a microscope), the upper limit depends on the tensile strength of the coupon. Given Si and SiO_2 are traditionally used as sacrificial layers for surface-micromachining in MEMS technology [9], PZT was deposited through the CSD method as described in chapter 2 on these layers to make suspended coupons. Both wet etching (with aqueous etchant) and dry etching (with gaseous etchant) on these sacrificial layers were tested to find the optimal coupons.

4.5.1.1 Wet etching

The common wet-etchants for Si are alkaline potassium hydroxide (KOH) and tetramethyl ammonium hydroxide (TMAH) solutions. TMAH is a buffered solution (controlled pH) with the molecular formula $N(CH_3)_4OH$. TMAH exhibits anisotropic etching (faster etching along Si [100]), providing well-defined vertical sidewalls, higher selectivity against SiO_2, and a controlled etch rate. On the other hand, KOH is a relatively stronger base, which is known for isotropic etching, lower selectivity against SiO_2, and higher etch rates. Hence, the choice between the two depends on the desired etch profile and the specific requirements of the fabrication process [10]. For the SiO_2 sacrificial layer, the wet-etchants are aq. HF and BHF. Our PZT film was already observed to react with aq. HF or BHF

strongly, as discussed in chapter 2. Now, we test KOH and TMAH to etch Si layer under the PZT film and see how they react with the PZT.

A PZT film of thickness 165 nm was deposited on a standard Si substrate. The sample was cleaned and spin-coated with Ti35 photoresist at 4000 rpm for 40 seconds. The coupons[2] were patterned on the photoresist mask with optical lithography followed by etching with RIE. The photoresist mask was then washed away with acetone and IPA, and the sample was treated with an O_2 plasma for 5-10 min to clean any polymer residues. Finally, the sample was dipped into the aq. etchant at 80°C.

Figure 4.13 (a) and (b) show the optical images after 23 min exposure in KOH solution and 60 min exposure in 5% TMAH solution, respectively. It can be seen from these images that the PZT film was more affected by the long exposure to the (concentrated) KOH solution. Due to poor visibility, it was difficult to see the extent of Si underetching. Moreover, the profilometer suggested the depth of the etched Si was not enough to have full suspension. Hence, aq. KOH was not a good option. On the other hand, the PZT film appeared to withstand 5% TMAH exposure for a relatively longer time. However, there was pitting on the PZT surface and thinning down (0.73 μm) of the tether, as shown in the zoom-in image in fig 4.13 (c). This suggested that the PZT film also reacted with the diluted TMAH solution.

Another option is to use an amorphous Si (a-Si) sacrificial layer with TMAH etching, as the amorphous layer is easier to etch compared to crystalline Si. However, the attempt to deposit a PZT film on the a-Si layer did not work out, as the a-Si layer started to break down during the high temperature (450°C) annealing process. These observations suggested that wet-etching had several challenges. In addition to the described issues, the collapse of the suspended structure due to stiction during the drying process is also a well-known challenge with wet-etching. Hence, in the next experiment, underetching the PZT layer with HF vapor to remove the oxide layer was tested.

4.5.1.2 Dry etching

To release the PZT coupons in a dry environment, HF vapor was used to undercut the SiO_2 sacrificial layer as discussed in chapter 2. To release the PZT coupons with dry etching, a 290 nm PZT film was deposited on two types of substrates.

1. PZT/SOI: We already demonstrated successful fabrication of PZT on Si beam structures. Now, the goal was to test if longer coupons of PZT/Si (supported by tethers) can also be released.

[2] An existing photomask designed by Tom Vanackere (for $LiNbO_3$ coupons) was used for patterning PZT coupons.

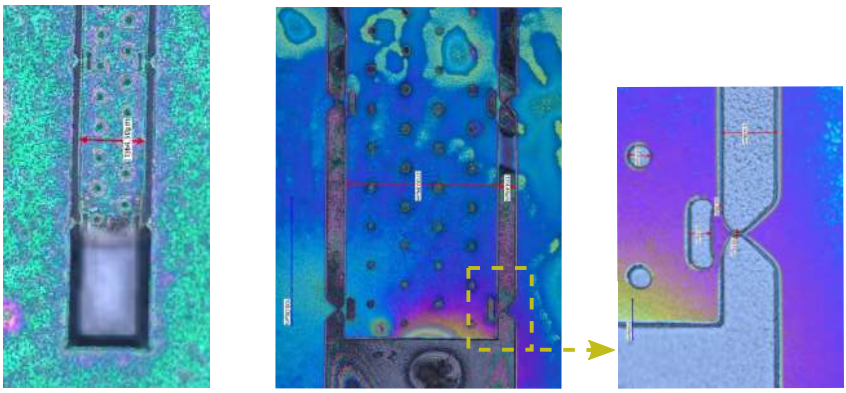

Figure 4.13: PZT/Si underetching process (a) after 23 min KOH exposure, (b) after 60 min TMAH exposure, (c) zoom-in image showing the thinning tether and pitting on the PZT film after 60 min TMAH exposure.

2. PZT/SiO_x: Since the box-oxide in a typical SOI is treated at a high temperature, its etch rate is slower. Hence, 2 μm SiO_x was deposited using the PECVD method on a Si substrate. Thereafter, a PZT film was deposited on top of that.

For this dry etch test, the samples were prepared similarly to the we-etching process as described above. In addition, before the etching process, the samples were heated on a hot plate for at least 10-15 min to ensure dehydration. Finally, the samples were loaded in the HF-VPE100 vapor etcher with the substrate holder temperature set at 40 °C. The extent of the undercut was monitored through a microscope. The progression of underetch is shown in figure 4.14.

Figure 4.14 (a) and (b) show the optical image of sample 1 (PZT/SOI) after 140 min and 240 min of HF vapor exposure, respectively. After 140 min, the lateral undercut was observed to be around 7-8 μm, suggesting 50-60 nm/min of lateral etch rate. After 240 minutes, the coupon seemed fully released. This was in line with the estimated etch rate as the hole-to-hole distance was 24 μm, so 12 μm lateral etching was required to fully release the PZT/Si coupon.

Figure 4.15 (a) and (b) show the optical image of two types of fully suspended coupons obtained from PZT on SiO_x, after 15 min and 45 min of HF vapor exposure, respectively. In figure 4.15 (a), the coupon was designed with stress-release holes, which also act as underetch windows. These holes reduced the required lateral etch distance to 12 μm (half of the hole-to-hole distance) for the full release. On the other hand, the coupon shown in figure 4.15 (b) had to be laterally etched for 60 μm (half of the coupon width) to be fully released. That is why despite the same total width (120 μm), the coupon with the holes took only 15 min, whereas

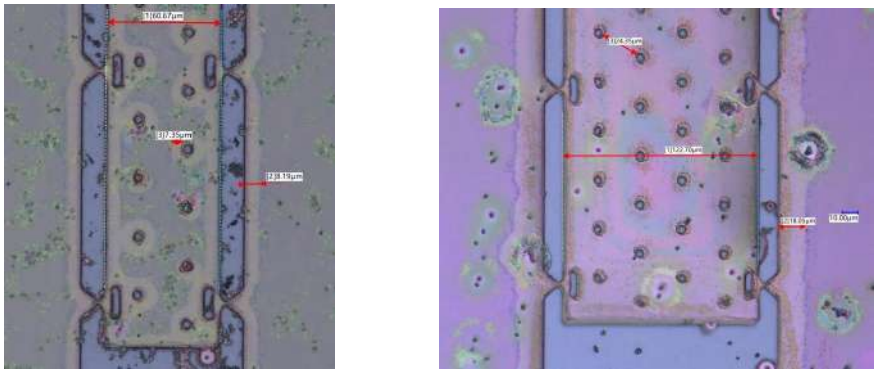

(a) (b)

Figure 4.14: Optical image of 290 nm PZT/SOI sample (a) after 140 min HF VPE (b) after 240 min HF VPE.

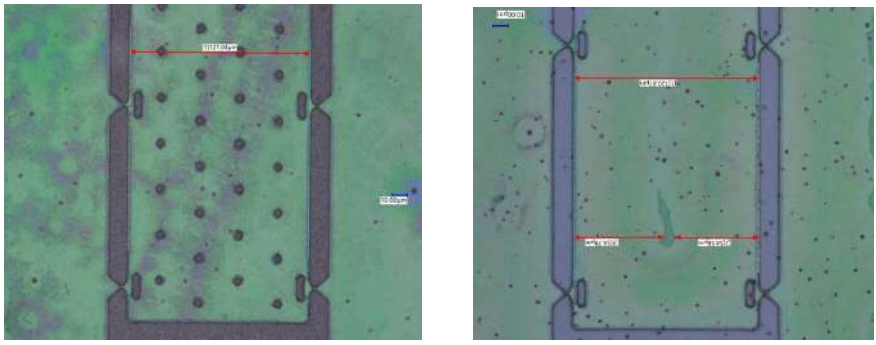

(a) (b)

Figure 4.15: (a) Suspended PZT coupon with stress-release holes after 15 min HF vpe (b) suspended PZT coupon after 45 min HF vpe.

the coupon without holes took 45 min to be fully released. The visual inspection through a microscope suggested that the sample with the short exposure of HF vapor (15 min) still had some SiOx layer left. On the contrary, the sample etched for a longer duration (45 min) looked cleaner. This can be seen by comparing the etched SiO_2 region in figure 4.15 (a) and (b). To find out the etched depth, a profilometer measurement with Dektak was done across the underetch window on these two samples. The measured average slope height (ASH) indicated that the sample after only 15 min HF vapor exposure, still had $\sim$ 540 nm of SiO_2 layer left. Whereas the second sample with 45 min of HF vapor exposure had almost no SiO_2 layer left.

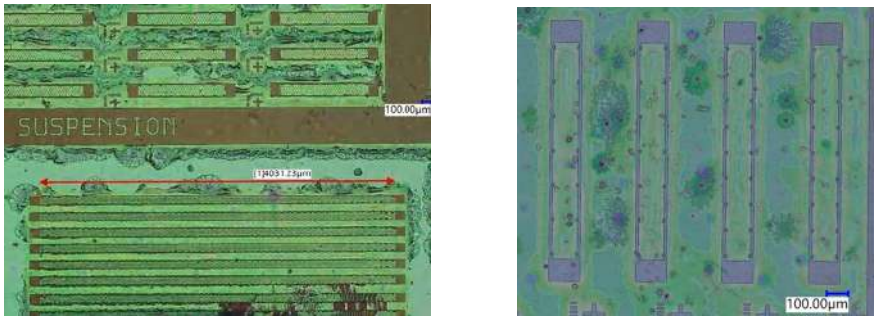

(a) (b)

Figure 4.16: (a) Up to 4 mm long and 120 µm wide released PZT coupons with stress-release holes (b) up to 1 mm long and 120 µm wide suspended PZT coupons without holes.

Figure 4.16 (a) and (b) show the released long coupons with holes and without holes respectively. As expected, the stress-release holes enabled the release of long PZT coupons up to 4 mm, due to rather uniform stress distribution in the suspended coupons. On the other hand, the length of the successfully released PZT coupons without holes was found to be up to 1 mm, as shown in figure 4.16 (b). To get a quick idea of whether these coupons were actually released or not, scotch tape was used to peel-off the released coupons. The peeled-off coupons were observed with a microscope. This suggested that the coupons were most likely released and could be used for μTP.

4.5.2 Transfer printing

For the μTP test[3], two Si substrates were used as target samples. Both samples were thoroughly cleaned with acetone/IPA, dehydrated, and treated with O_2 plasma for 20 minutes. One sample was used as a bare Si target sample to test the direct bonding, whereas, on the other sample, a thin adhesive BCB film (40-50 nm) was spin-coated.

Figure 4.17(a) shows a 60 μm wide and 1 mm long PZT coupon with stress-release holes, picked up with a polydimethylsiloxane (PDMS) stamp of the same size. The attempt to transfer print this PZT coupon was unsuccessful on both the target samples, even at higher temperatures. Figure 4.17(b) shows that a lot of residues from the coupons were stuck on the adhesive BCB/Si target sample. This indicated that there was a lot of residual SiO_2 underneath the PZT coupon, making it difficult for μTP. These residual SiO_2 were expected given that this sample was exposed to the HF vapor for a short duration.

[3] μTP was carried out by Jasper de Witte and Tom Vandekerckhove.

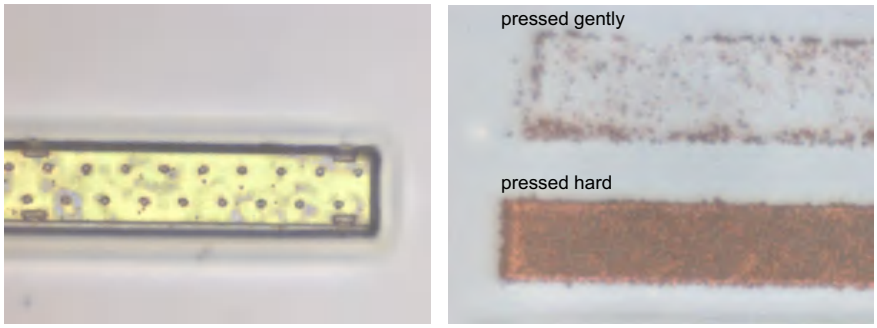

(a) (b)

Figure 4.17: (a) 60 μm wide and 1 mm long PZT coupon with holes after picked up from the source sample, (b) residues on the BCB/Si target sample after the coupon was pressed on it gently and harder.

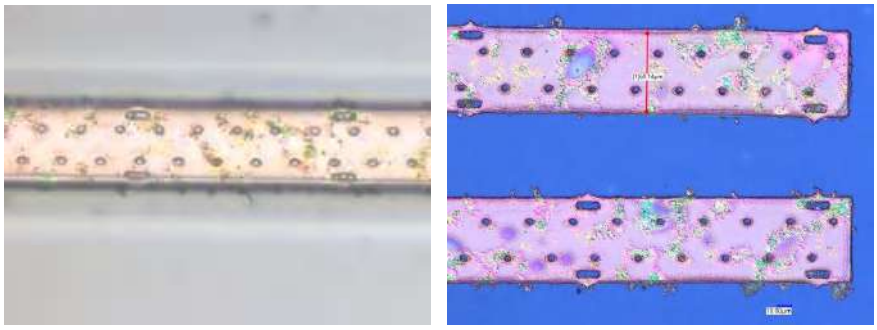

(a) (b)

Figure 4.18: (a) 60 μm wide and 1 mm long coupon after picked up from the source sample, (b) coupon after transferring on the target sample (BCB/Si).

In the next trial, μTP of PZT on Si coupons was tested. Figure 4.18 (a) shows a 60 μm wide and 1 mm long PZT/Si coupon, after being picked up with a PDMS stamp. μTP of this coupon was unsuccessful on the bare Si target sample. This poor bonding was supposedly due to the rough surface underneath the coupon from the residues or byproducts of the SiO_2 etching. On the other hand, the μTP was successful on the BCB/Si target sample, albeit at a high temperature (80 °C). The transferred PZT/Si coupons are shown in figure 4.18 (b). This further indicated that the main reason for the unsuccessful μTP of PZT coupon was indeed the residual SiO_2.

In the next μTP trial of PZT, the coupons without the stress-release holes were used. These coupons were supposed to have very low SiO_x residues as confirmed

by the profilometer measurement. Hence, they were expected to make better bonding on the target samples.

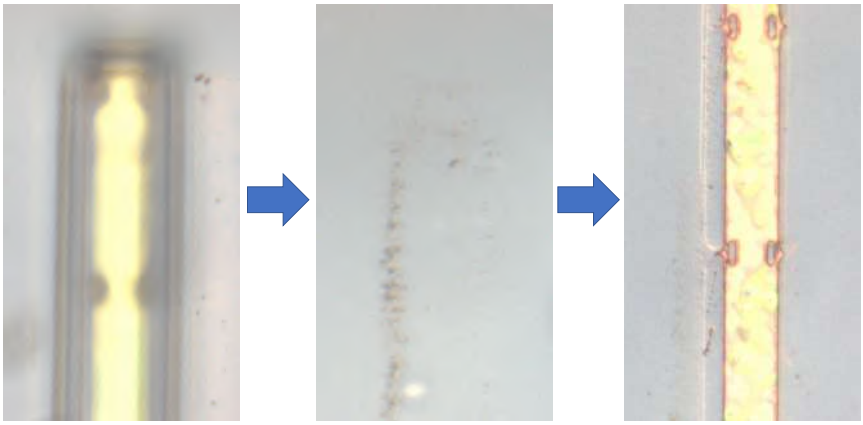

Figure 4.19: (a) 30 μm PZT coupon picked up with a 60 μm wide stamp, (b) a soft press on the target sample to get rid of residues, (c) a hard press on the target sample for μTP.

The PZT coupon of width 60 μm (and length 1 mm) broke during the pick-up step. Hence, an adjacent PZT coupon of width 30 μm and similar length was picked up. Figure 4.19 (a) shows the PZT coupon picked with a 60 μm wide and 1 mm long PDMS stamp. Having learned about the residual SiO_x underneath the coupons, now in step 2 the coupon was gently pressed on the target sample to get rid of the residues. Figure 4.19 (b) shows the transferred residues on the target sample. In the final step, the PZT coupon was pressed harder against the BCB/Si target sample at 80 °C. This led to a successful μTP of the PZT film as shown in figure 4.19 (c).

4.6 Conclusion

In this chapter, we successfully demonstrated the fabrication and characterization of PZT based MEMS devices. The PZT process optimizations reported in the previous chapter 2 were implemented for the fabrication. These actuators were characterized by a custom-built LDV setup. The measurement further confirmed the strong piezoelectric actuation with the poled PZT sample. These results prove the MEMS actuation capability of our PZT films, opening the possibilities of realizing integrated MEMS structures on PICs as illustrated by a few examples here. In the following chapter, we demonstrate some photonic MEMS devices for light modulation.

Given the technological challenges with PZT integration on a non-planarized chip, micro-transfer printing (μTP) was investigated as an alternate route. The release process using HF vpe rendered PZT coupons of length up to 4 mm and width up to 120 μm, indicating a strong tensile strength of the PZT film. The direct μTP of PZT coupons on a Si substrate was not possible due to the residues underneath the coupons. However, a successful μTP of PZT film was demonstrated on a BCB/Si target sample at 80 °C. These preliminary results suggested that PZT μTP could be a viable option, given that a clean PZT coupon is obtained. In our HF vpe there was no option to include any other carrier gas to clean up the etching byproducts. If a newer version of HF vpe with the possibility to add other etching gases could be used, it could help in getting cleaner and residues-free PZT coupons. This could be worth investigating, given the advantages of the μTP process. For example, the μTP of PZT can provide flexibility to integrate PZT on a non-uniform chip. Moreover, it can help in achieving complex MEMS designs that would otherwise be very challenging to get with conventional fabrication techniques.

References

[1] J. P. George, P. F. Smet, J. Botterman, V. Bliznuk, W. Woestenborghs, D. Van Thourhout, K. Neyts, and J. Beeckman. *Lanthanide-Assisted Deposition of Strongly Electro-optic PZT Thin Films on Silicon: Toward Integrated Active Nanophotonic Devices*. ACS Applied Materials & Interfaces, 7(24):13350–13359, 2015.

[2] Polytec. *Laser Doppler vibrometry*. `https://www.polytec.com/us/vibrometry/technology/laser-doppler-vibrometry`. URL Accessed: 2023-05-23.

[3] Brett Piekarski, Don DeVoe, Madan Dubey, Roger Kaul, and John Conrad. *Surface micromachined piezoelectric resonant beam filters*. Sensors and actuators A: Physical, 91(3):313–320, 2001.

[4] Robert Littrell and Karl Grosh. *Modeling and characterization of cantilever-based MEMS piezoelectric sensors and actuators*. Journal of Microelectromechanical Systems, 21(2):406–413, 2012.

[5] Warren Jin, Ronald G. Polcawich, Paul A. Morton, and John E. Bowers. *Piezoelectrically tuned silicon nitride ring resonator*. Opt. Express, 26(3):3174–3187, Feb 2018.

[6] Tom Vanackere, Maximilien Billet, Camiel Op de Beeck, Stijn Poelman, Gunther Roelkens, Stéphane Clemmen, and Bart Kuyken. *Micro-transfer printing of lithium niobate on silicon nitride*. In 2020 European Conference on Optical Communications (ECOC), pages 1–4. IEEE, 2020.

[7] Picavet, Ewout and Rijckaert, Hannes and Beeckman, Jeroen and Van Thourhout, Dries and De Buysser, Klaartje. *Direct integration of Pb(Zr,Ti)O3 thin films : a pathway towards high-speed modulators*. In Belgian Ceramic Society, Annual meeting, Abstracts., 2021.

[8] Gunther Roelkens, Jing Zhang, Laurens Bogaert, Maximilien Billet, Dongbo Wang, Biwei Pan, Clemens J. Kruckel, Emadreza Soltanian, Dennis Maes, Tom Vanackere, Tom Vandekerckhove, Stijn Cuyvers, Jasper De Witte, Isaac Luntadila Lufungula, Xin Guo, He Li, Senbiao Qin, Grigorij Muliuk, Sarah Uvin, Bahawal Haq, Camiel Op de Beeck, Jeroen Goyvaerts, Guy Lepage, Peter Verheyen, Joris Van Campenhout, Geert Morthier, Bart Kuyken, Dries Van Thourhout, and Roel Baets. *Micro-Transfer Printing for Heterogeneous Si Photonic Integrated Circuits*. IEEE Journal of Selected Topics in Quantum Electronics, 29(3: Photon. Elec. Co-Inte. and Adv. Trans. Print.):1–14, 2023.

[9] J Bühler, FP Steiner, and H Baltes. *Silicon dioxide sacrificial layer etching in surface micromachining*. Journal of Micromechanics and Microengineering, 7(1):R1, 1997.

[10] Kanishka Biswas and S Kal. *Etch characteristics of KOH, TMAH and dual doped TMAH for bulk micromachining of silicon*. Microelectronics journal, 37(6):519–525, 2006.

5 Suspended photonic MEMS

In this chapter, we delve into the manipulation and control of light through piezoelectrically driven photonic micro-electromechanical system (MEMS) devices. Building upon our previous experience with MEMS fabrication and characterization, we now integrate piezo-MEMS actuators within Si photonic devices to harness electro-optomechanical interaction in the waveguide. The photonic MEMS devices were fabricated by under-etching the SiO_2 sacrificial layer from the PZT deposited on an SOI photonic chip. The free suspension of the device enables a large mechanical perturbation in the suspended structure when driven at its resonance frequency. This procures a stronger strain-optic overlap in the waveguide without leaking the mechanical energy into the substrate [1]. For instance, as discussed in chapter 3, the inter-digitated transducer (IDT) driven surface acoustic wave (SAW) suffers from acoustic loss into the bulk substrate. Hence, suspending the IDT can help in confining the SAW into the waveguide, which can enhance the acousto-optic interaction.

5.1 Fabrication of the photonic MEMS devices

The two photonic MEMS devices we aimed to manufacture are illustrated in figure 5.1 (a) and (b), respectively. The suspended inter-digitated transducer (IDT), depicted in 5.1 (a), was designed to allow a resonance of the SAW within the suspended device to enhance acousto-optic interaction. The suspended electro-optomechanical transducer (EOMT), depicted in 5.1 (b), was designed to harness

both electro-optic and acousto-optic interaction within the waveguide.

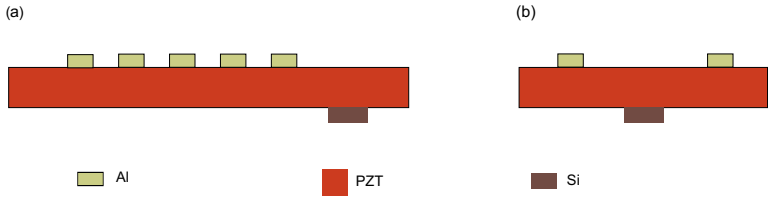

Figure 5.1: 2D schematic of the suspended devices (a) suspended IDT (b) suspended EOMT.

The devices were fabricated with the optimized process steps as discussed in chapter 2. Figure 5.2 presents the full process flow.

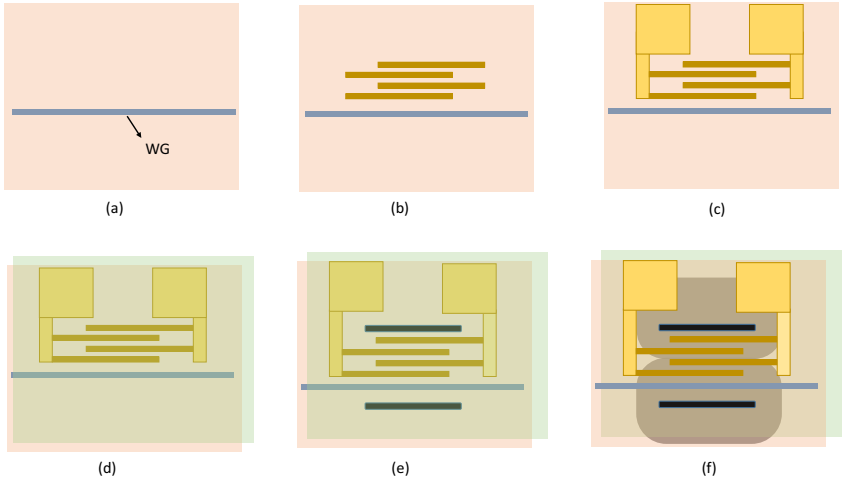

Figure 5.2: Schematic diagrams showing the top view of the process flow (a) PZT deposition on planarized Si circuit (b) e-beam lithography followed by e-gun deposition for Al IDT fingers (c) Optical lithography followed by metal evaporation for Al contact pads (d) ALD deposition of 50 nm Al_2O_3 and partial etching of Al_2O_3 film from contact pads (e) Dry etching through Al_2O_3/PZT with RIE to make etch windows (f) HF vapor exposure to under-etch SiO_2.

A photonic SOI chip with waveguide circuits was used as a starting sample. This chip was fabricated by an imec multi-project wafer (MPW) process where the waveguides were defined with deep UV exposure in a 220 nm thick silicon layer on top of a 2 μm buried SiO_2 layer. The wafer was planarized using SiO_2 deposition and chemical mechanical polishing (CMP).

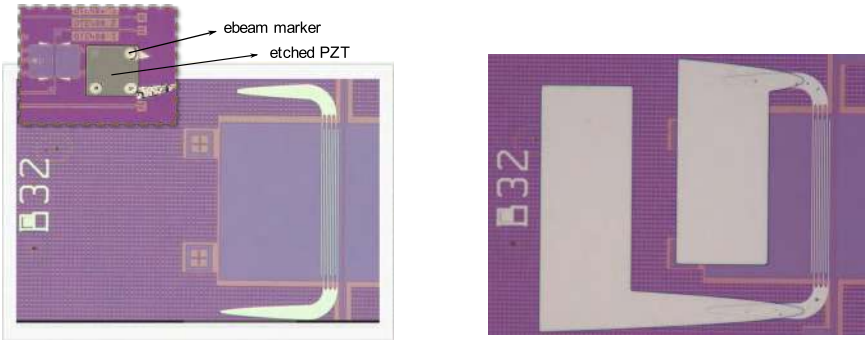

(a) (b)

Figure 5.3: (a) An e-beam lithography followed by e-gun deposition for Al IDT fingers (b) Optical lithography followed by metal evaporation for Al contact pads.

Our in-house processing on the sample starts with $\sim$ 400 nm PZT thin film deposition using the chemical solution deposition method as described in [2]. Due to the high permittivity of the PZT, it was difficult to image the high-resolution markers on the chip with e-beam. Hence, the PZT film was partially etched on locations containing e-beam markers as shown in figure 5.3(a) inset. An optimized PZT etching recipe was used with reactive-ion etching (RIE) involving CHF_3, SF_6, Ar and O_2 reactant gases. Then, the electrodes (>500 nm wide) were defined using e-beam lithography[1] followed by Al deposition using e-gun and a lift-off process. Most of the IDTs were defined with pitch 1 μm to maximize the acousto-optic overlap in the 450 nm wide Si waveguide [3]. These electrodes are shown in figure 5.3 (a). Now, the contact pads were patterned with optical lithography, followed by Al deposition with e-gun deposition and a lift-off process as shown in figure 5.3(b). Given the possibility of an alignment error in the contact region between the e-beam patterned electrodes and the UV patterned contact pads, the connection was defined as a tapered shape to minimize the scattering of microwave signals from the sharp edges in the connection line.

In the next step, a 50 nm thick Al_2O_3 film was deposited on the sample using atomic layer deposition (ALD)[2]. This low-density (less mass-loading) thin film was employed as a protection layer against HF vapor. In step (V), the Ti 35 was spin-coated on the sample, and the under-etch windows were patterned using a UV lithography process. After hard-baking the sample, the first layer of Al_2O_3 thin film was etched with a diluted 1% (by volume) buffered hydrogen fluoride (BHF) solution, followed by dry etching with RIE to remove the PZT layer. Subsequently,

[1] e-beam patterning was carried out by Muhammad Muneeb
[2] ALD was done by David Schaubroeck from the CMST group

the Ti35 hard mask was dissolved with AZ 100K remover at 70°C, and the sample was cleaned in an O_2 plasma. Thus, a prepared sample is obtained as shown in figure 5.4(a). We notice a lot of hillock formation on the Al electrode surface. They most likely appear due to stress-release in the Al film after the high-temperature ($\sim$ 250°C) ALD process [4]. Finally, in step (VI), the sample was dehydrated and loaded in an HF vapor phase etcher (Idonus VPE100) to expose the sample to HF vapor at a substrate temperature of 40°C. The undercut was monitored by looking through the microscope until the device was fully suspended. In figure 5.4 (b), an optical image of a fully suspended device is shown. It can be observed from the color contrast that due to the irregular flow of the HF vapor, the under-etching is not uniform but the targeted region (between the two underetch windows) looks fully suspended.

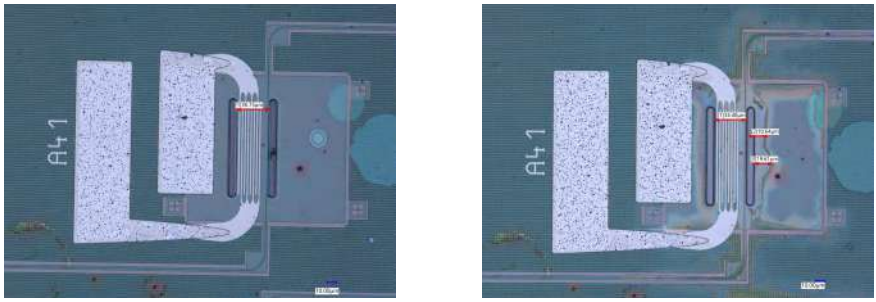

(a) (b)

Figure 5.4: (a) Prepared sample for underetching (b) after 38 min of HF vapor exposure.

To verify the full suspension of the device, a cross-section was made on one of the devices on the chip using a focused ion beam (FIB). The scanning electron microscope (SEM) images of the cross-section are shown in figure 5.5, whereas an optical image of the cross-section region is shown in the inset. In the image 5.5(a), the suspended structure can be seen with $\sim$ 2 μm of SiO_2 under-etched. We also notice that there is around 280 nm thick layer of SiO_2 still seems to be present under PZT and around the Si waveguide. Even after another exposure to HF vapor, these residues remained there. From 5.5(b), we confirm the PZT thickness to be around 400 nm.

The optical transmission was measured on a suspended device (test) and a non-suspended device (control) on the same chip using a tunable laser. The transmission result indicated $\sim$ 5 dB optical loss from the suspended structure. This could be due to the roughness of the suspended waveguide surface, as shown in figure 5.5(b).

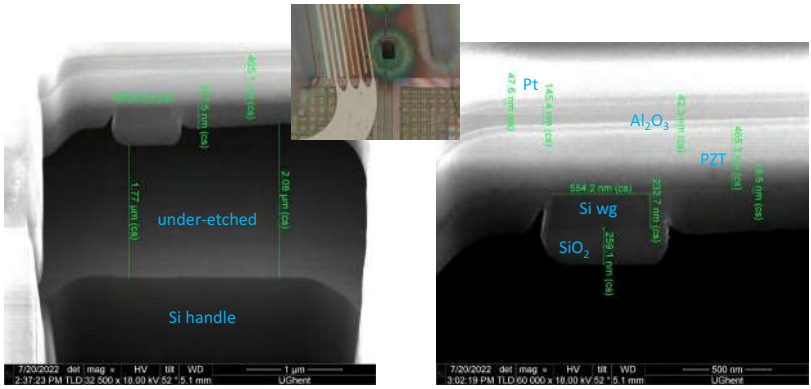

Figure 5.5: SEM image after FIB cross-section of a suspended device. (a) image showing the undercut, (b) zoom-in image showing multi-layers in the suspended structure. In the inset, the optical image shows the location of the FIB cross-section on the sample.

5.2 Results from the suspended IDT

To measure the acousto-optic modulation from the suspended IDT device, we use a heterodyne setup as described in [5]. Before starting the modulation measurement, we first measure the light transmission in the suspended device with respect to the laser wavelength. The wavelength sweep suggested the highest transmission in the device at $\sim$ 1590 nm. This is different than the expected 1550 nm because of the PZT film cladding on the grating couplers. Therefore, in the subsequent acousto-optic measurement, we used a probe light with a free space wavelength of 1590 nm from a continuous wave C-band laser.

In figure 5.6 we present the modulation efficiency $\eta^2 = P_{sideband}/P_{AOM}$ measured on the devices. Here $P_{sideband}$ is the peak power of the sideband and P_{AOM} is the peak power of the AOM signal. For a detailed description of the measurement technique, see chapter 3. Figure 5.6 (a), shows the effect of poling the PZT film on the modulation efficiency. Since our PZT is a polycrystalline thin film, we do an electrical poling of the film to align its domain polarization along the applied electric field. During the poling process, a sufficiently high DC voltage (just below the PZT breakdown voltage) is applied to the IDT to pole the underneath PZT film (along the IDT in-plane electric field). The poling voltage is determined based on the electrode-electrode spacing (pitch/2) of the IDT, So $V_{poling} \sim 15$ V/μm $\times$ pitch/2. From figure 5.6(a), we observe that after the poling, the modulation efficiency at the main resonance ($\sim$ 7 GHz) is increased, and another small mod-

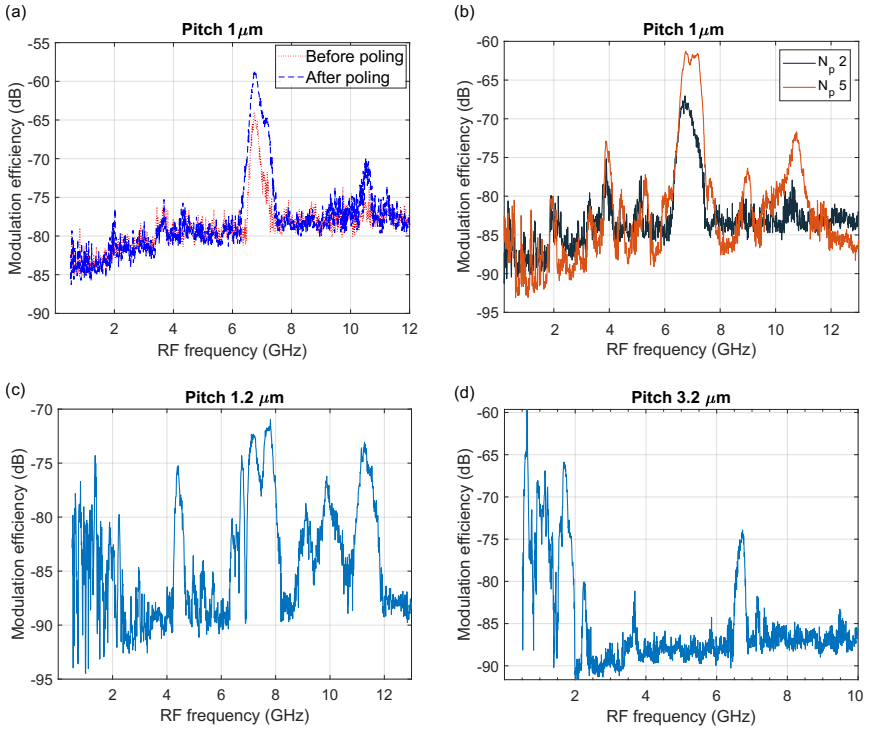

Figure 5.6: Heterodyne measurement of acousto-optic modulation efficiency of the suspended IDT devices by driving with 12 dBm RF power. (a) poling effect in the device with pitch 1 μm and aperture 70 μm (b) measured modulation (before poling) two devices with different number of finger-pairs (N_p) but same IDT pitch of 1 μm pitch and aperture 100 μm, (c) and (d) shows pitch effect in the device with IDT finger-pair of 4 and aperture 100 μm.

ulation peak appears around $\sim$ 10.5 GHz. The improvement in the modulation is expected because of the longitudinal transduction of SAW as explained in [5].

Figure 5.6 (b) illustrates the modulation from two IDTs with 3 and 5 finger-pairs N_p . For both IDTs, pitch and aperture were fixed at 1 μm and 100 μm respectively. We notice that, as expected, the modulation peak increases with the number of finger-pairs.

Figure 5.6 (c) and (d) show the modulation efficiency from two IDTs with different pitch. As expected, the IDT with a lower pitch 1.2 μm gives modulation up to 11.3 GHz (c), whereas the IDT with a higher pitch gives modulation at lower frequencies, up to 6.7 GHz only (d).

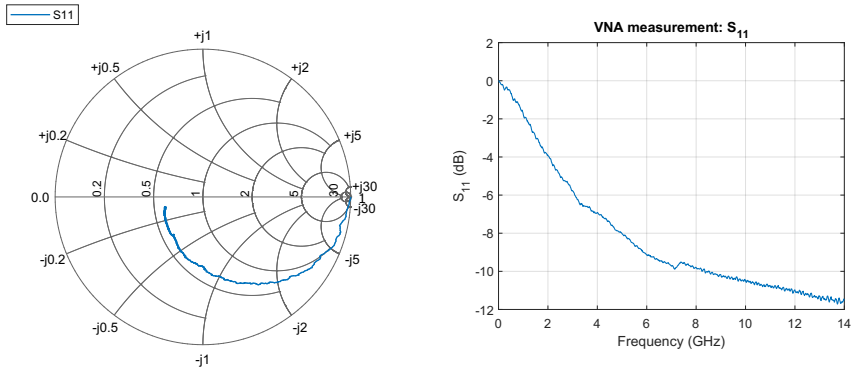

(a) (b)

Figure 5.7: VNA measurement on the device with pitch 1 μm and aperture 70 μm (a) Smithplot (impedance normalized with 50 Ω) showing the capacitive behavior of the IDT (b) magnitude of S_{11} showing a dip around $\sim$ 7.1 GHz.

Later, we measured the electrical reflection parameter S_{11} with a vector network analyzer (VNA) on the poled device with IDT pitch 1 μm and aperture 70 μm. From the VNA measurement data, we plot the Smith chart and magnitude of S_{11} as shown in figure 5.7 (a) and (b) respectively. The Smith chart shows that the suspended IDT device is capacitive, as we expect. In the $|S_{11}|$ plot, we observe a small dip around $\sim$ 7.1 GHz. This corresponds to the modulation peak frequency obtained with the optical measurement on the device, as shown in figure 5.6 (a). This indicates that indeed at$\sim$ 7.1 GHz, the suspended IDT actuates a SAW that modulates the light signal in the waveguide. The measurement shown in figure 5.6(a) was done at 12 dBm RF power. That corresponds to 1.26 V voltage amplitude (V_p) considering a 50 Ω load impedance. From this voltage, $V_\pi L$ is equal to $\pi \times V_p \times L/\alpha$; where α is the phase modulation amplitude calculated from the modulation efficiency (η^2) as $\alpha = 2 \times 10^{(\eta^2[dB]/20)}$ and L is the IDT aperture [5]. At 7.1 GHz, $V_\pi L$ was calculated to be 22.53 V·cm before poling and 12.15 V.cm after poling.

In several works [5–7], $V_\pi L$ is presented as a figure of merit for the acousto-optic modulation. However, while calculating V_p corresponding to the applied RF power, the load impedance is conveniently taken as 50 Ω, which is not correct. The load impedance depends on the device and its material properties. For example, the impedance of an IDT is frequency dependent due to its capacitive nature, and further changes at the SAW resonance frequency due to electromechanical coupling [8]. This is evident in figure 5.7(a). From the load impedance (Z_L), the actual load voltage V_L is equal to $|Z_L/(Z_L + Z_S)| \times V_S$, where Z_S = 50 Ω is the source impedance and V_S is the source voltage. For a detailed derivation, see ap-

pendix A. From the Smith chart of the poled device in 5.7(a), we obtain Z_L at 7.1 GHz to be (30-17j) Ω, which gives V_L = 1.06 V. Thus, the actual $V_\pi L$ is calculated to be 10.22 V·cm.

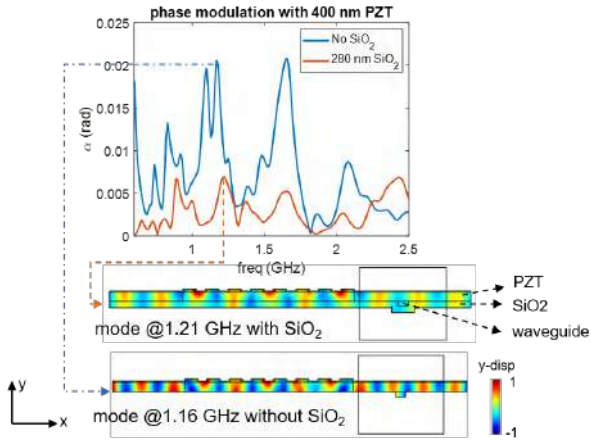

Figure 5.8: Piezoelectric actuation simulation of suspended IDT without and with 280 nm residual SiO_2. The vertical displacement profile shows the acoustic mode.

We notice that these figures of merit are lower compared to the results from the non-suspended SAW modulator reported in chapter 3. To find out the possible reason, we carried out a frequency domain simulation of the suspended IDT as illustrated in figure 5.8. Here, the Al IDT of pitch 1 μm and thickness 100 nm was defined on 400 nm PZT, and the top surface was (conformally) covered with 50 nm Al_2O_3. From this simulation result, it appears that the unwanted residual oxide (and the resulting acoustic mismatch) perturbs the resonant actuation from the IDT, lowering the acousto-optic phase modulation. Additionally, the IDT of pitch 1 μm was defined for a thinner ($\sim$ 200 nm) PZT film [3], but the PZT film in this device was thicker (400 nm). Another contributing factor for the lower modulation could be the quality of the PZT being compromised with the HF vapor exposure [9]. Unfortunately, due to the PZT production issue, we could not make new devices to investigate it further.

5.3 Piezoelectrically driven Fano resonator

Integrated electro-optic modulators based on the Pockels effect are often implemented using a co-planar electrode design in which parallel electrodes are used to apply an electric field across the electro-optic material [10]. The optical mode is confined partially or completely inside a linear electro-optic material such as barium titanate (BTO), lead zirconate titanate (PZT), or lithium niobate ($LiNbO_3$).

When an electric field is applied across the material, due to the electro-optic (EO) effect i.e. polarizability change in the material, the effective index of the mode changes. Typically, these modulators show a broadband modulation response with their bandwidth limited by the RC-effects if the modulator length is not too long, where R is the contact resistance and C is the capacitance of the device. Their flat modulation response is attributed to the lack of any mechanical perturbation (resonance), mainly for two reasons. Firstly, the traditional electro-optic materials have a weaker piezoelectric coupling, so it does not produce a significant mechanical actuation. Secondly, the compact geometry of the conventional EO modulators limits their mechanical deformation.

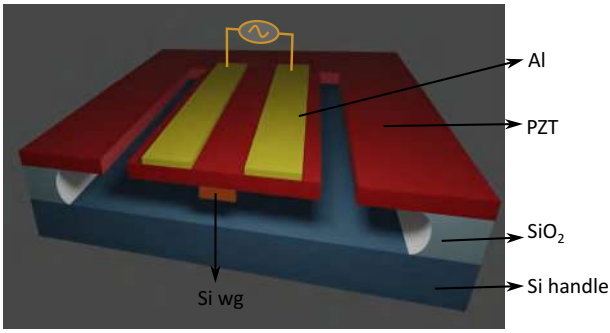

Figure 5.9: A 3D schematic of a suspended EO device. The cross-section view shows the PZT film integrated on top of the Si waveguide and the SiO_2 underneath is underetched.

In this work, we demonstrate an electro-optomechanical transducer (EOMT), where the EO device is suspended by under-etching the SiO_2 layer as illustrated in figure 5.9. The free suspension of the device offers numerous advantages. It allows a large mechanical perturbation in the suspended structure when driven (with a piezoelectric effect) at its resonance frequency. This procures a stronger strain-optic overlap in the waveguide without leaking the mechanical energy into the substrate. [1]. This gives a large optical phase modulation in the waveguide through the photoelastic effect (PE). In the suspended waveguide structure (large surface-to-volume ratio), a significant amount of the electric field from the optical mode is concentrated at the interfaces. This is due to a high refractive index contrast between the materials. When the waveguide boundary is distorted at the mechanical resonance, the field distribution changes. Hence, this so-called moving boundary (MB) effect also changes the effect mode index. In addition, the radiation pressure from the input light creates distortion in the suspended waveguide [1, 11]. However, given that the input laser power in our waveguide is not very high, this effect can be ignored. Therefore, the total index modulation for our suspended EOMT can be given as follows:

$$\Delta n_{eff}^{tot} = \Delta n_{eff}^{EO} + \Delta n_{eff}^{PE} + \Delta n_{eff}^{MB} \tag{5.1}$$

Where Δn_{eff}^{EO}, Δn_{eff}^{PE} and Δn_{eff}^{MB} are the effective index modulation from electro-optic (EO) effect, photoelastic effect (PE) and moving boundary (MB) effect respectively. At the mechanical resonance of EOMT, the polarizability of the PZT (hence n_{eff}^{EO}) changes slightly due to the electromechanical coupling. However, compared to Δn_{eff}^{PE} and Δn_{eff}^{MB}, which are strongly dependent on the mechanical deformation, Δn_{eff}^{EO} can be assumed frequency independent (see appendix 5.6.1). The frequency dependence of Δn_{eff}^{PE} and Δn_{eff}^{MB} can be expressed as following:

$$\Delta n_{eff}^{PE} + \Delta n_{eff}^{MB} = \Delta n_0^{EM} \mathcal{L}(\Omega) \tag{5.2}$$

where Δn_0^{EM} is the index modulation amplitude from the electromechanical actuation, Ω is the applied RF (angular) frequency and $\mathcal{L}(\Omega)$ is the frequency response. This index modulation (equation 5.3) arises due to the piezoelectric driving of EOMT, which can be regarded as a mechanical oscillator. Hence, this frequency response can be presented by the driven oscillator response. Assuming the linewidth (Γ) of the modulation response $<<$ the resonance frequency (Ω_m), the frequency response near Ω_m can be approximated as Lorentzian [12].

$$\mathcal{L}(\Omega) = \frac{\Gamma/2}{(\Omega - \Omega_m + j\Gamma/2)} = \frac{1}{\Delta\epsilon + j} \tag{5.3}$$

where $\Delta\epsilon = \frac{(\Omega - \Omega_m)}{\Gamma/2}$ is the reduced frequency detuning.

From equation 5.1, 5.3 and 5.3,

$$\begin{aligned} \Delta n_{eff}^{tot} &= \Delta n_{eff}^{EO} + \frac{\Delta n_0^{EM}}{\Delta\epsilon + j} \\ &= \Delta n_{eff}^{EO}\Big(\frac{\Delta\epsilon + \Delta n_0^{EM}/\Delta n_{eff}^{EO} + j}{\Delta\epsilon + j}\Big) \\ &= \Delta n_{eff}^{EO}\Big(\frac{\Delta\epsilon + q + j}{\Delta\epsilon + j}\Big) \end{aligned} \tag{5.4}$$

Where $q = \Delta n_0^{EM}/\Delta n_{eff}^{EO}$, can be termed as Fano or asymmetric parameter. The phase modulation amplitude from the modulator of length L,

$$\begin{aligned} \alpha(L) &= \frac{2\pi L}{\lambda}|\Delta n_{eff}^{tot}| \\ &= D\Big|\frac{\Delta\epsilon + q + j}{\Delta\epsilon + j}\Big| \\ \Rightarrow \alpha(L)^2 &= D^2\left(\frac{(\Delta\epsilon + q)^2 + 1}{\Delta\epsilon^2 + 1}\right) \end{aligned} \tag{5.5}$$

Where D = $\frac{2\pi L}{\lambda}\Delta n_{eff}^{EO}$ is a multiplication factor to the Fano expression.

Figure 5.10 illustrates a log plot of equation 5.5 for different values of q. Here the multiplication factor D was taken as unity for simplification. We can see that when $q << 1$ i.e. the EO modulation is much stronger than the EM modulation, the frequency response is flat as seen from a typical EO modulator. Whereas, when $q >> 1$ i.e. the EM modulation is much stronger than the EO modulation, the frequency response is Lorentzian as can be seen from an acousto-optic modulator [6, 13]. However, when both EO and EM modulations are comparable, their interference produces a Fano-shape frequency response. And the polarity of the Fano curve relies on the sign of q. Now, based on this understanding, we will characterize EOMT.

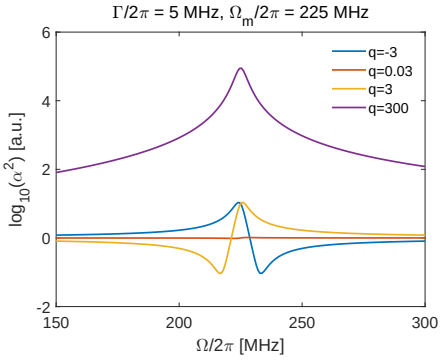

Figure 5.10: Frequency response of EOMT with different Fano parameter q.

5.4 Experimental results from the suspended EOMT

Figure 5.11(a) shows the modulation efficiency η^2 measured on EOMT1 driven with a 12 dBm RF driving signal, before and after poling the PZT film. EOMT1 has an electrode (el-el) separation of 4 μm and a waveguide width of 450 nm. Before the poling, the as-deposited PZT shows 4 main peaks labeled as B_0,B_1,B_2 and B_3. These peaks could be possibly due to the shear mode actuation through the transverse electric field (in-plane) with respect to the PZT domains, which are oriented out-of-plane after deposition. [2, 5, 14]. Moreover, the transverse electric field generates a weak EO effect. This is manifested through the low broadband (non-resonance) modulation response. The weak EO response furthermore explains the absence of any Fano response. Next, the PZT film was poled to align its domain polarization along the applied in-plane electric field. For the poling process, a DC voltage (40 V) was applied to the electrodes at room temperature for about 40-60 min.

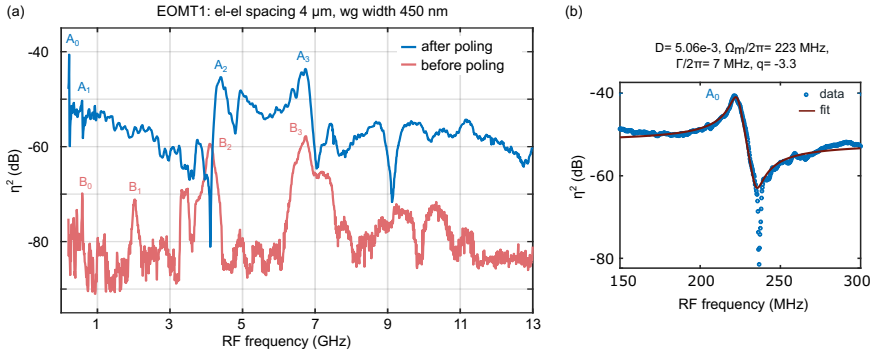

Figure 5.11: (a) Modulation efficiency (η^2) of EOMT1 of el-el spacing 4 µm and waveguide width 450 nm driven with 12 dBm RF power. (b) Measurement data of the primary Fano resonance and fit result with the Fano formula.

After the poling process, EOMT1 shows several Fano-like (asymmetric) resonances. The Fano resonance peaks are labelled as A_0 ($\sim$ 220 MHz), A_1 ($\sim$ 570 MHz), A_2 ($\sim$ 4.4 GHz) and A_3 ($\sim$ 6.73 GHz). As explained above, these Fano resonances appear due to the interference between the broadband EO response and a narrow-band mechanical mode excitation. Since the strongest Fano resonance was observed around 220 MHz, an additional measurement was carried out to collect more data points around this resonance (A_0). This measured data was then fitted with the Fano formula described in equation 5.5. Both the data and the fitting plot are presented in figure 5.11(b). With more data points, we can clearly see that the dip of the Fano curve goes to the noise floor, with an extinction ratio and slope of $\sim$ 41 dB and 1.194×10^{-3} rad/MHz, respectively. The higher frequency Fano resonance (A_3) has an extinction ratio and slope of $\sim$ 21 dB and 0.0353×10^{-3} rad/MHz, respectively.

Figure 5.12 shows the electrical measurement on EOMT1 with the VNA. The Smith plot shown in figure 5.12(a) confirms the capacitive behavior of the device and the electromechanical actuation at certain frequencies. The curve representing the magnitude of the reflection scattering parameter S_{11} presented in figure 5.12(b), shows five main transduction dips: V_0 ($\sim$ 229 MHz), V_1 ($\sim$ 600 MHz), V_2 ($\sim$ 2.50 GHz), V_3 ($\sim$ 3.31 GHz) and V_4 ($\sim$ 6.76 GHz). The dips V_0, V_1, V_3 and V_4 correspond to the resonance peaks A_0, A_1, A_2 and A_3 from EOMT1 as presented in figure 5.11(a).

Now, using the data from both electrical and optical measurements, the figure of merit for EOMT1 was calculated as presented in table 5.1. The table illustrates that $V'_\pi L$ calculated with Z_L is higher than the $V_\pi L$ calculated with 50 Ω. This is because our capacitive device has a higher impedance at lower frequencies.

Figure 5.13(a) shows the modulation efficiency η^2 measured for EOMT2 driven

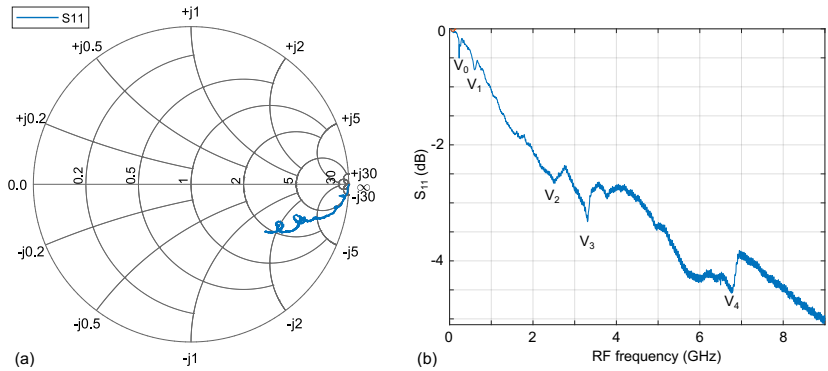

Figure 5.12: Electrical measurement with VNA on EOMT1 (a) Smith plot showing the capacitive behavior of the device (b) the magnitude of S_{11} showing the transduction dips.

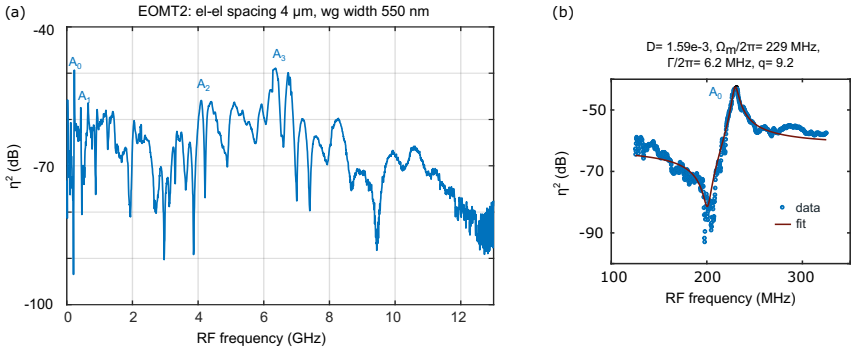

Figure 5.13: (a) Modulation efficiency (η^2) of EOMT2 of el-el spacing 4 μm (TE waveguide 550 nm) driven with 14 dBm RF power (b) Measurement data of the primary Fano resonance and the fitting result with the Fano formula.

with 14 dBm of RF power. EOMT2 has an electrode (el-el) separation of 4 μm but a waveguide width of 550 nm. This measurement was taken after poling the PZT film. Here, we see Lorentzian peaks, Fano peaks, and dips. We believe this might be due to a stronger perturbation in the wider Si waveguide. Figure 5.13(b) shows a detail data points around the primary mode (A_0) of EOMT2 and a fit to the Fano curve. We notice that the Fano curve has opposite polarity compared to the similar mode from EOMT1.

To understand this polarity difference, we calculated the strain-optic overlap integral along the x-direction (Γ_{SOxx}) for the PZT and Si layers as described below,

$$\Gamma_{SOxx} = -\frac{n_{eff}^3}{2} \frac{\int_D E^* \left(sign(p_{ij}) * S_{xx}\right) E \, dr}{\int_D E^* \epsilon E \, dr} \tag{5.6}$$

peak	$\Omega/2\pi$ (MHz)	η^2 (dB)	α (rad)	$V_\pi L$ (V·cm) @Z_o= 50 Ω	$Z_L/50$ (Ω)	$V'_\pi L$ (V·cm) @Z_L
A_0	220	-40.6	0.019	2.12	6.33-j23.07	4.19
A_1	570	-50.50	0.006	6.47	4.35-j10.22	12.46
A_2	4400	-45.30	0.011	3.64	2.49-j2.95	6.15
A_3	6730	-43.6	0.013	3.00	2.33-j1.86	4.67

Table 5.1: Figure of merit calculated from the measured modulation efficiency (η^2) and S_{11} of EOMT1.

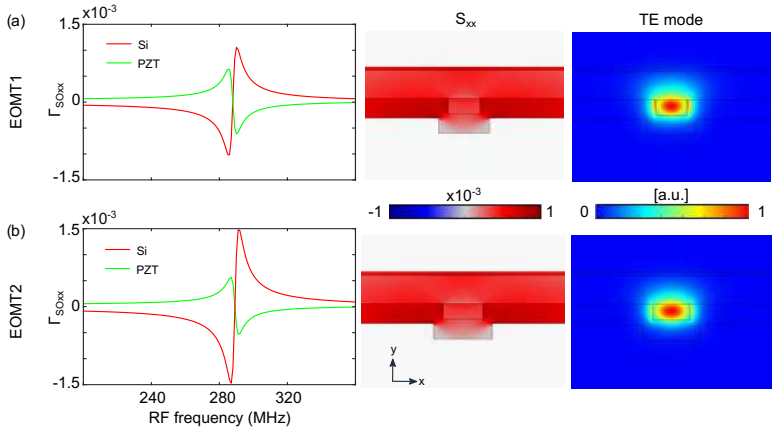

Figure 5.14: Strain-optic overlap integral (Γ_{SOxx}), surface plot of the strain-x component (S_{xx}) at $\sim$ 290 MHz and TE mode profile from (a) EOMT1 and (b) EOMT2.

Here $sign(p_{33})$ for PZT is $+$ and $sign(p_{11})$ for Si is $-$. This term was introduced to take the sign of p_{ij} into account. This expression is similar to Δn_{eff}^{PE} except for the value of p_{ij}. The coefficient p_{ij} values were omitted for both layers as the accurate value for PZT is not known. In figure 5.14, we see that the strain-optic overlap (Γ_{SOxx}) from the two layers are in opposite polarity due to the opposite signs of their p_{ij}. This indicates that the net polarity of the PE modulation depends on which layer is dominating. Also, as expected, we observe that Γ_{SOxx} in Si increases when the waveguide width is increased. We believe this trade-off between the PE contribution from the Si and PZT layer could be the reason for the opposite polarity of EOMT2 compared to that of EOMT1.

Figure 5.15 shows η^2 measured on a third device, EOMT3, driven by 14 dBm of RF power. EOMT3 has an electrode (el-el) separation of 5 μm and a waveguide width of 550 nm. The measurement on the device before poling shows one strong peak (B_0) at $\sim$ 6.62 GHz. However, after poling the PZT film, several peaks are observed. In this case, we only see Lorentzian-shape resonances in the modulation

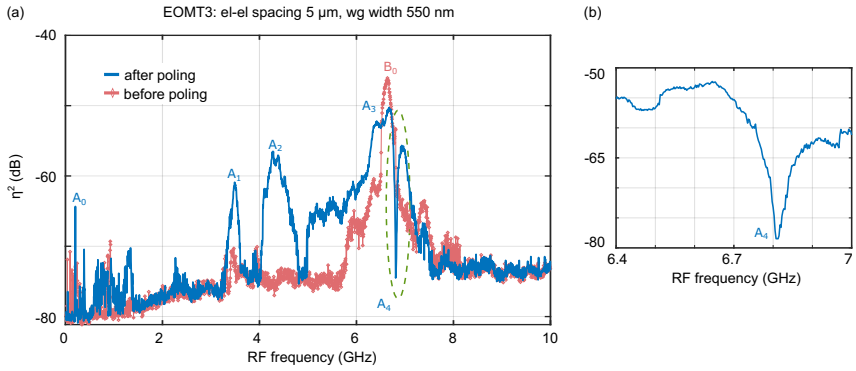

Figure 5.15: (a) Modulation efficiency (η^2) of the suspended EOMT of el-el spacing 5 µm and waveguide width 550 nm driven with 14 dBm RF power. (b) Plot with more data points around the sharp dip at ∼ 6.8 GHz.

but no clear Fano resonance. Additionally, the background EO response is also very weak. This suggests that the PZT film might not have been completely poled. This is a plausible explanation since EOMT3 has a wider electrode separation, and our poling voltage was limited by the voltage tolerance of the GS probe (∼ 45 V), so we could not apply a sufficiently high voltage. The other noteworthy observation is the sharp dip (A_4) around 6.8 GHz. We believe this feature appears due to the interference between the longitudinal mechanical mode actuated by the poled PZT domains and the shear mechanical mode actuated by the out-of-plane PZT domains.

5.5 Conclusion

We fabricated a suspended IDT next to a waveguide and etched the underneath SiO_2 to create an acoustic resonance from the actuated SAW. This was done to enhance the acousto-optic interaction in the waveguide. However, we found the figure of merit from these devices to be poor compared to that of a non-suspended SAW modulator. We suspect this could be due to the thicker PZT film, as the acoustic strain from the small period IDT does not sufficiently reach the waveguide. Besides, the HF exposure might have some detrimental effect on the PZT film quality. This is something that needs to be thoroughly investigated. Unfortunately, we could not carry out this investigation due to the issue with the PZT film deposition.

On the same chip, we also designed suspended EOMT, which oscillates strongly when driven with an RF signal at its resonance frequency. The interference between the narrow-band modulation from the mechanical oscillation and the broad-

band modulation from the electro-optic effect results in a Fano-shape modulation spectrum. At the lower mechanical mode 223 MHz, we obtained a very high modulation extinction of 41 dB. And, for a higher-order mode at 6.7 GHz, we obtained a lower extinction of 21 dB. Our results demonstrate a novel way to generate Fano resonance in PICs that could open up new possibilities for the development of highly sensitive devices.

5.6 Additional information

5.6.1 Calculation of the n_{eff} modulation

When a suspended structure is actuated with the piezoelectric effect, it can experience a change in the effective refractive index (Δn_{eff}) through the following mechanisms:

5.6.1.1 Moving boundary (MB) effect

When a mechanical motion is exerted into the waveguide, the waveguide boundaries are distorted. This changes the electric field distribution at the boundaries in accordance with Maxwell's continuity law. If the optical mode field lines experience sharp medium changes, the mechanical distortion can have a significant impact on n_{eff}. This change can be estimated by integrating the distortion and the optical field components at the interface as described below [15].

$$\Delta n_{eff}^{MB} = \frac{n_{eff}}{2} \frac{\oint_B (Q \cdot \hat{n}) \left(E_{\parallel}^* \Delta\epsilon E_{\parallel} - D_{\perp}^* \Delta\epsilon^{-1} D_{\perp} \right) dS}{\int_D E^* \epsilon E \, dr} \tag{5.7}$$

where Q is the displacement field, $\hat{n}$ is the outward normal vector of the boundary, E and D are the electric field and the displacement field of the optical mode. The subscripts $\parallel$ and $\perp$ denote parallel and perpendicular components at the boundary. ϵ is the permittivity of the waveguide mode. $\Delta\epsilon = \epsilon_1 - \epsilon_2$ and $\Delta\epsilon^{-1} = \epsilon_1^{-1} - \epsilon_2^{-1}$, where ϵ_1 and ϵ_2 are the permittivity of the medium 1 (denser medium) and medium 2 respectively. Here D stands for the 2D cross-section domain of the waveguide.

In figure 5.16 (a), Δn_{eff}^{MB} calculated from the different interfaces of EOMT1 are shown. For this calculation, only the interfaces closer to the mode profile were selected, as other interfaces had negligible effect. Here, we observe that the strongest contribution comes from the Si-PZT interface. This is because of a strong index contrast and the optical field density, as can be seen from the mode profile in figure 5.14(a). On the other hand, the outer-most interface SiO_2-air has a weaker MB effect as both the index contrast and the optical field are comparatively lower at this interface.

5.6.1.2 Photo-elastic (PE) effect

In addition to the distortion of the electric field density at the boundary, the mechanical perturbation also influences the bulk properties of the waveguide medium. This volumetric perturbation affects the electron density of the dielectric medium [16], thus changing the n_{eff}. This index change can be calculated as follows [17]:

$$\Delta n_{eff}^{PE} = -\frac{n_{eff}^3}{2} \frac{\int_D E^* \boldsymbol{pS}\, E\, dr}{\int_D E^* \epsilon E\, dr} \tag{5.8}$$

where E is the electric field of the waveguide mode, $\boldsymbol{p}$ is the photoelastic tensor of the waveguide medium and $\boldsymbol{S}$ is the strain field. In the waveguide mode region, the PZT film was in-plane poled. So, the 2D simulation plane of the PZT material is a ZX plane. For such crystal orientation of PZT (a tetragonal crystal with 3m point group symmetry), $\boldsymbol{pS}$ can be expanded as follows:

$$\boldsymbol{pS} = \begin{bmatrix} p_{33} & p_{31} & p_{31} & 0 & 0 & 0 \\ p_{13} & p_{11} & p_{12} & 0 & 0 & 0 \\ p_{13} & p_{12} & p_{11} & 0 & 0 & 0 \\ 0 & 0 & 0 & p_{66} & 0 & 0 \\ 0 & 0 & 0 & 0 & p_{44} & 0 \\ 0 & 0 & 0 & 0 & 0 & p_{44} \end{bmatrix} \begin{bmatrix} S_{xx} \\ S_{yy} \\ S_{zz} \\ S_{yz} \\ S_{zx} \\ S_{xy} \end{bmatrix},$$

Therefore, for the PZT layer, equation 5.8 can be approximated as following considering a TE mode ($E_x >> E_y$),

$$\Delta n_{eff}^{PE} = -\frac{n_{eff}^3}{2} \frac{\int_D E_x^* (p_{33} S_{xx} + p_{31} S_{yy} + p_{31} S_{zz})\, E_x\, dr}{\int_D E^* \epsilon E\, dr} \tag{5.9}$$

Thus, we require two unknown material parameters, p_{33} and p_{31}, to calculate the PE contribution Δn_{eff}^{PE} from the PZT layer. It should be noted that the PZT thin film is a relatively new material for photonic applications because they are traditionally grown using a Pt buffer layer (optically lossy). That is why the photoelastic coefficients ($\boldsymbol{p}$) of such thin film have not been properly estimated. In [18], it was demonstrated that for ABO_3 type Ferroelectric thin films, $p_{33} > p_{31}$ and from [19] p_{33} can be roughly assumed to be around 0.60. Using these values as starting parameters, the experimental result shown in figure 5.11(b) was fitted with the simulation result (after normalizing them with their respective multiplication factor D) to estimate the unknown parameters for the PZT film. From the least square fitting, we obtained $p_{33} \approx 0.48$ and $p_{31} \approx 0.40$. In addition, we also extracted the other unknown PZT parameter, Pockel's coefficient $r_{33}^{eff} \approx 75$ pm/V, to calculate the EO modulation. Note that these values may not be accurate. Since the material parameters used in the simulation may be different from our PZT film. Nevertheless, these values can be used to get a qualitative understanding of the Fano behavior.

For the Si crystal orientation [110], a rotational transformation was applied on the photoelastic tensor of Si taken from [17] resulting in the following coefficients: p_{11}= -0.090, p_{12} = 0.013, p_{21} = p_{12} and p_{22} = p_{11}. For SiO_2, p_{11}= 0.121, p_{12} = 0.270 were taken from [20]. Now, using these coefficients and the simulation results, Δn_{eff}^{PE} was calculated for each layer as shown in figure 5.16(b). Here we observe that Δn_{eff}^{PE} from Si has opposite polarity compared to the rest of the layers. This is because the strongest photoelastic coefficient for Si, p_{11} has a negative sign.

5.6.1.3 Electro-optic (EO) effect

When an electric field is applied to a dielectric medium, its polarization change leads to the change in n_{eff}. If the dielectric medium is a non-centrosymmetric crystal (i.e. PZT), Δn_{eff} is linearly proportional to the applied electric field. This proportionality constant is termed as the Pockel's coefficient (r_{ij}). If the applied electric field or optical power is very high, the second-order electro-optic effect, also known as Kerr effect, can also contribute to the index change. For the coplanar waveguide and electrodes in our EOMT, the main driving field is along the x-direction ($\mathcal{E}_x$). If the effective Pockel's coefficient along the x-direction is assumed r_{33}^{eff}, the effective index change can be estimated as [21]:

$$\Delta n_{eff}^{EO} = -\frac{\epsilon_0\, n_{eff}^5}{2} \frac{\int_D \left[E_x^*(r_{33}^{eff}\mathcal{E}_x)E_x\right] dr}{\int_D E^* \epsilon E\, dr} \tag{5.10}$$

Figure 5.16(c) shows the contribution to Δn_{eff} from each mechanism described above. Here we can see that Δn_{eff}^{EO} has a rather weak frequency dependence compared to the frequency response from other mechanisms. This validates our assumption of the frequency-independent EO response for deriving the Fano expression as described in equation 5.4. Therefore, the total change in n_{eff} in the suspended device:

$$\Delta n_{eff}^{total} = \Delta n_{eff}^{MB} + \Delta n_{eff}^{PE} + \Delta n_{eff}^{EO} \tag{5.11}$$

Figure 5.16(d) shows the modulation efficiency (η^2) and the phase modulation amplitude (α^2) calculated from Δn_{eff}^{total}. Here L and λ were taken as 100 μm and 1590 nm respectively. Thus, we see a Fano resonance when EOMT1 is piezoelectrically driven with an RF signal. This simulation result corresponds to the measured Fano response reported in figure 5.11(b). The deviation in the simulation result can be attributed to the difference in the parameters used in the simulation and the experiment.

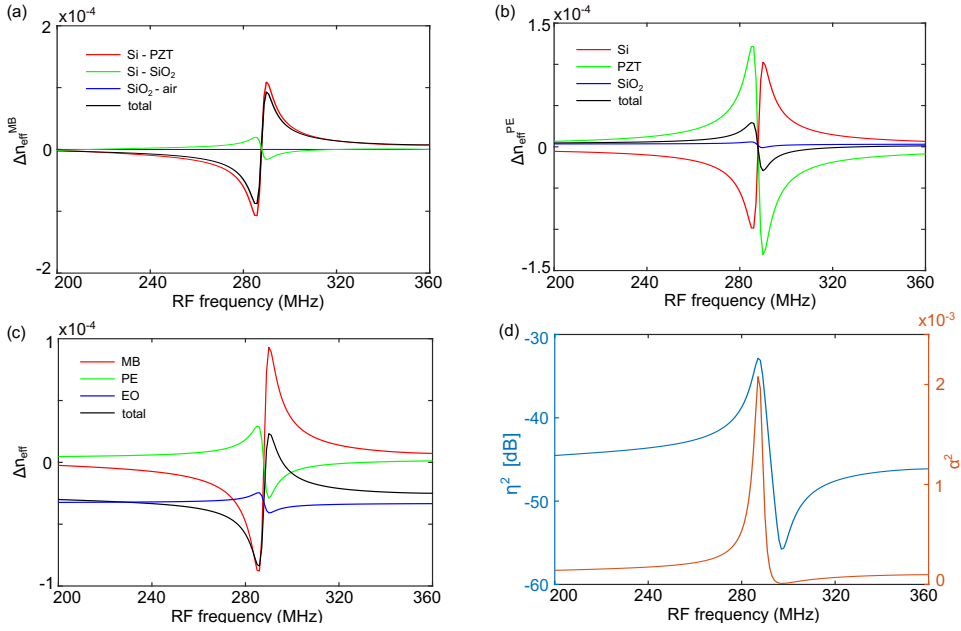

Figure 5.16: Calculation of the index modulation from the simulated results (a) Δn_{eff}^{MB} plot for different interfaces in the waveguide mode region, (b) Δn_{eff}^{PE} plot for different layers in the waveguide system, (c) Δn_{eff} contribution from different mechanisms, (d) log and linear plot of the net phase modulation.

References

[1] Peter T Rakich, Charles Reinke, Ryan Camacho, Paul Davids, and Zheng Wang. *Giant enhancement of stimulated Brillouin scattering in the subwavelength limit*. Physical Review X, 2(1):011008, 2012.

[2] J. P. George, P. F. Smet, J. Botterman, V. Bliznuk, W. Woestenborghs, D. Van Thourhout, K. Neyts, and J. Beeckman. *Lanthanide-Assisted Deposition of Strongly Electro-optic PZT Thin Films on Silicon: Toward Integrated Active Nanophotonic Devices*. ACS Applied Materials & Interfaces, 7(24):13350–13359, 2015.

[3] Irfan Ansari, Jeroen Beeckman, and Dries Van Thourhout. *PZT Based Acoustic Resonator for the Refractive Index Modulation*. In 2022 Workshop on Recent Advances in Photonics (WRAP), pages 1–2, 2022.

[4] B Cao Martin, CJ Tracy, JW Mayer, and LE Hendrickson. *A comparative study of Hillock formation in aluminum films*. Thin Solid Films, 271(1-2):64–68, 1995.

[5] Irfan Ansari, John P. George, Gilles F. Feutmba, Tessa Van de Veire, Awanish Pandey, Jeroen Beeckman, and Dries Van Thourhout. *Light Modulation in Silicon Photonics by PZT Actuated Acoustic Waves*. ACS Photonics, 9(6):1944–1953, 2022.

[6] Eric A. Kittlaus, William M. Jones, Peter T. Rakich, Nils T. Otterstrom, Richard E. Muller, and Mina Rais-Zadeh. *Electrically driven acousto-optics and broadband non-reciprocity in silicon photonics*. Nature Photonics, 15:43–52, 1 2021.

[7] Chukun Huang, Haotian Shi, Linfeng Yu, Kang Wang, Ming Cheng, Qiang Huang, Wenting Jiao, and Junqiang Sun. *Acousto-Optic Modulation in Silicon Waveguides Based on Piezoelectric Aluminum Scandium Nitride Film*. Advanced Optical Materials, 10(6):2102334, 2022.

[8] C.S. Hartmann, D.T. Bell, and R.C. Rosenfeld. *Impulse Model Design of Acoustic Surface-Wave Filters*. IEEE Transactions on Microwave Theory and Techniques, 21(4):162–175, 1973.

[9] YS Yoon, JH Kim, AM Schimidt, DL Polla, Q Wang, WL Gladfelter, and YH Shin. *RuO 2/Ru electrode on Si 3 N 4/Si substrate for microelectromechanical systems devices based on Pb (Zr 1-x Ti x) O 3 film and surface micromachining*. Journal of Materials Science: Materials in Electronics, 9:465–471, 1998.

[10] R. Soref and B. Bennett. *Electrooptical effects in silicon*. IEEE Journal of Quantum Electronics, 23(1):123–129, 1987.

[11] Raphaël Van Laer, Bart Kuyken, Dries Van Thourhout, and Roel Baets. *Interaction between light and highly confined hypersound in a silicon photonic nanowire*. Nature Photonics, 9(3):199–203, 2015.

[12] Eugene Kamenetskii, Almas Sadreev, and Andrey Miroshnichenko. *Fano resonances in optics and microwaves*. Springer Series in Optical Sciences Book Series, 2018.

[13] Irfan Ansari, Dries Van Thourhout, John P. George, Gilles F. Feutmba, and Jeroen Beeckman. *Acousto-optic modulation in a Si-waveguide*. In 2021 IEEE 17th International Conference on Group IV Photonics (GFP), pages 1–2, 2021.

[14] Irfan Ansari, Gilles F Feutmba, Emiel Dieussaert, John P George, Jeroen Beeckman, and Dries Van Thourhout. *PZT based actuator for an efficient electro-optomechanical interaction in Si-photonic integrated circuits*. In Integrated Optics: Devices, Materials, and Technologies XXVI, volume 12004, pages 266–269. SPIE, 2022.

[15] Krishna C Balram, Marcelo Davanço, Ju Young Lim, Jin Dong Song, and Kartik Srinivasan. *Moving boundary and photoelastic coupling in GaAs optomechanical resonators*. Optica, 1(6):414–420, 2014.

[16] Hans Mueller. *Theory of the photoelastic effect of cubic crystals*. Physical review, 47(12):947, 1935.

[17] DK Biegelsen. *Frequency dependence of the photoelastic coefficients of silicon*. Physical Review B, 12(6):2427, 1975.

[18] Ranu Nayak, Vinay Gupta, and K Sreenivas. *Studies on acousto-optical interaction in epitaxial thin film heterostructures*. Journal of Physics D: Applied Physics, 32(4):380, feb 1999.

[19] Kotaro Takeda, Takuya Hoshina, Hiroaki Takeda, and Takaaki Tsurumi. *Electro-optic effect and photoelastic effect of feroelectric relaxors*. Japanese Journal of Applied Physics, 55(10S):10TB05, sep 2016.

[20] RW Dixon. *Photoelastic properties of selected materials and their relevance for applications to acoustic light modulators and scanners*. Journal of Applied Physics, 38(13):5149–5153, 1967.

[21] Robert W Boyd. *Nonlinear optics*. Academic press, 2020.

6 Conclusion and outlook

6.1 Conclusion

In chapter 1, we discussed the background and scope of the piezoelectric functionalities in Si PICs and highlighted the state-of-the-art material integration to enable piezoelectric actuation. In chapter 2, we reported the process optimization on the PZT film to fabricate suspended structures. We noted that PZT, as a novel material, brings a lot of fabrication challenges. Achieving a fast etching rate of the PZT film while maintaining good selectivity against the photoresist mask posed a challenge. Nevertheless, through careful optimization of the etching parameters, we successfully attained an acceptable etching performance. Additionally, the high-temperature crystallization process during the PZT deposition makes it CMOS incompatible. However, the PZT film can be added in the back end of line (BEOL) using our CSD method, provided the substrate surface is adequately planarized. In chapter 3, we investigated the piezoelectric properties of the PZT film by actuating surface acoustic waves. We first observed the SAW actuation through electrical measurements from the IDT defined on a poled PZT layer. Next, we integrated the SAW actuator within a Si PIC and measured the optical modulation, which further demonstrated the SAW actuation. However, we realized mass-loading from the thick (350 nm) IDT made of dense Au metal was an issue. In the next iteration, we deposited a thin (100 nm) IDT made of Al. With an IDT consisting of only four finger-pairs, we obtained a half-wave-voltage-length V_{π}L $\sim$ 3.6 V·cm at 2 GHz. In [1], using a Si waveguide integrated with AlN and an IDT consisting

of 107 finger-pairs, the V_πL was reported to be 1.8 V·cm at 3.11 GHz. Furthermore, an AlScN film was integrated by [2], and with an IDT consisting of 100 finger-pairs driven at 3.04 GHz (additionally, 50 pairs of interdigital electrodes serving as a SAW reflector), the V_πL was estimated to be 0.95 V·cm. Although these figures of merit seem better, note that they were obtained with an IDT of more than 100 finger pairs (SAW modulation peak increases with the number of finger pairs [3]). Hence, our PZT-based SAW modulator shows a promising result compared to the other piezoelectric materials integrated into SOI. Unfortunately, we couldn't fabricate new devices with a similar order of finger pairs to compare the device performance due to the PZT fabrication issues.

In chapter 4, we delved into the piezoelectric actuation of PZT-MEMS structures. The successful fabrication and characterization of such piezo-MEMS pave the way for realizing photonic MEMS devices. Additionally, we tested the micro-transfer printing of the PZT films to circumvent the substrate planarization requirement. Our preliminary result shows the potential for integrating long PZT coupons, which can be further improved upon solving the residue issue from the under-etching process. In chapter 5, we fabricated photonic MEMS devices and measured the light modulation in the waveguide through the RF driving of the MEMS actuators. From the suspended IDT, we did not observe any modulation improvement compared to the non-suspended device. We suspect this could be due to the residual oxide layer and the deterioration of the PZT film quality upon prolonged exposure to the HF vapor. Again, we could not investigate it further due to the issue with the PZT film production. However, we noticed a strong Fano resonance from the suspended EOMT structures. Such a Fano resonance, with its sharp asymmetric profile, holds potential for ultra-sensitive devices. We believe these results could further improve upon solving the issue with the under-etching process.

It is noteworthy that the piezoelectric applications reported on the Si platform in this thesis can also be implemented on the SiN platform, which heavily relies on additional material integration for light modulation [4–6].

6.2 Outlook

The integration of PZT into silicon photonics presents an exciting outlook. The electrical control offered by the piezoelectric effect can lead to numerous techniques for controlling and manipulating the optical signal. For instance, piezoelectrically driven narrow-band (GHz) modulators hold a key potential in quantum information processing, as they can provide an efficient way for a microwave to optical conversion [7]. In addition to filtering, narrow-band modulation, switching, and frequency shifting [8], SAW modulators can be employed for non-reciprocal light propagation. Figure 6.1(a) shows a GDS drawing of a proposed SAW device

designed for such an application. The IDT is placed next to the waveguide such that the actuated SAW can pump its momentum along the mode propagation. The IDT period is defined such that it launches a SAW with the required momentum for an inter-modal scattering from TM_{00} to TE_{00}. The phase-matching condition for this scattering ($\Delta k = k_m$, $\Delta\omega = \Omega_m$) is illustrated in figure 6.1(b). When a TM_{00} mode enters the waveguide, the propagating SAW scatters part of it into TE_{00}. Subsequently, both modes are separated using a polarization splitter and rotator (PSR) and collected using grating couplers. Such inter-modal scattering can be exploited to make on-chip isolators as demonstrated by [9].

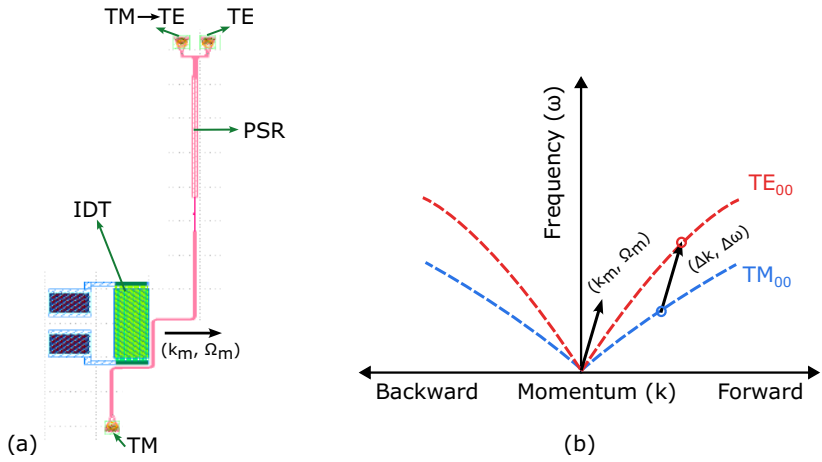

Figure 6.1: (a) A GDS design of an IDT next to a waveguide to pump momentum through SAW propagation (b) a dispersion diagram showing the phase matching condition for inter-modal scattering.

The MEMS actuation of the PZT film can also be exploited to achieve efficient tunable couplers and phase shifters, as discussed in chapter 4. Figure 6.2(a) shows a GDS drawing of a device that can be fabricated into an efficient tunable coupler. The doped Si is employed as a bottom electrode. The PZT film, followed by a top electrode, can be deposited onto the doped region. Undercutting this device can render a suspended MEMS device as illustrated in figure 6.2(b). The strong piezoelectric effect and optical transparency in our PZT can allow the fabrication of smaller MEMS devices with less risk of collapse during the under-etching process.

Future research on the material aspect could focus on optimizing PZT film production techniques, addressing challenges related to planarization, and improving under-etching processes. By refining these critical aspects, we can unlock the full potential of PZT integration, enabling more efficient and versatile transducers on photonic chips. Additionally, exploring alternative PZT integration methods that

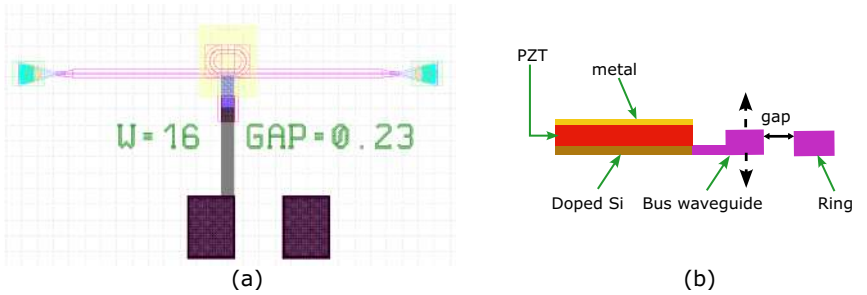

Figure 6.2: (a) A GDS design of doped Si connected to a bus waveguide of a ring resonator (b) a diagram showing the cross-section view of the proposed tunable coupler.

are fully compatible with CMOS technology would be a valuable avenue for further investigation. This could lead to the development of highly integrated and commercially viable photonic devices.

References

[1] Eric A. Kittlaus, William M. Jones, Peter T. Rakich, Nils T. Otterstrom, Richard E. Muller, and Mina Rais-Zadeh. *Electrically driven acousto-optics and broadband non-reciprocity in silicon photonics*. Nature Photonics, 15:43–52, 1 2021.

[2] Chukun Huang, Haotian Shi, Linfeng Yu, Kang Wang, Ming Cheng, Qiang Huang, Wenting Jiao, and Junqiang Sun. *Acousto-optic modulation in silicon waveguides based on piezoelectric aluminum scandium nitride film*. Advanced Optical Materials, 10(6):2102334, 2022.

[3] T. Erdogan. *Fiber grating spectra*. Journal of Lightwave Technology, 15(8):1277–1294, 1997.

[4] Tarun Sharma, Jiaqi Wang, Brajesh Kumar Kaushik, Zhenzhou Cheng, Roshan Kumar, Zhao Wei, and Xuejin Li. *Review of recent progress on silicon nitride-based photonic integrated circuits*. Ieee Access, 8:195436–195446, 2020.

[5] Sandeep S. Saseendran, Tangla D. Kongnyuy, Bruno Figeys, Federico Buja, Benedetto Troia, Sarp Kerman, Aleksandrs Marinins, Roelof Jansen, Xavier Rottenberg, Deniz S. Tezcan, and Philippe Soussan. *A 300mm CMOS-Compatible PECVD Silicon Nitride Platform for Integrated Photonics with Low Loss and Low Process Induced Phase Variation*. In 2019 Optical Fiber Communications Conference and Exhibition (OFC), pages 1–3, 2019.

[6] Jeong Hwan Song, Tangla D. Kongnyuy, Benedetto Troia, Sandeep Seema Saseendran, Philippe Soussan, Roelof Jansen, and Xavier Rottenberg. *Grating devices on a silicon nitride technology platform for visible light applications*. OSA Continuum, 2(4):1155–1165, Apr 2019.

[7] Linbo Shao, Mengjie Yu, Smarak Maity, Neil Sinclair, Lu Zheng, Cleaven Chia, Amirhassan Shams-Ansari, Cheng Wang, Mian Zhang, Keji Lai, and Marko Lončar. *Microwave-to-optical conversion using lithium niobate thin-film acoustic resonators*. Optica, 6(12):1498–1505, Dec 2019.

[8] Antonio Crespo-Poveda, R Hey, K Biermann, A Tahraoui, PV Santos, B Gargallo, P Muñoz, A Cantarero, and MM de Lima. *Synchronized photonic modulators driven by surface acoustic waves*. Optics express, 21(18):21669–21676, 2013.

[9] Donggyu B Sohn and Gaurav Bahl. *Direction reconfigurable nonreciprocal acousto-optic modulator on chip*. APL Photonics, 4(12):126103, 2019.

A

VNA measurement

A.1 Electrical characterization technique

For the electrical characterization of our devices, a Fieldfox- VNA was used. Before the measurement, VNA was calibrated in the required frequency range using a standard calibration substrate containing short, open, load and through (SOLT) contacts. This calibration ensures that the impedance of the RF probe, connector or cable are not taken into account while measuring the reflection scattering parameter (S_{11}) of the device under test (DUT) [1]. The measured reflection parameter (S_{11}) is given by,

$$S_{11} = \frac{Z_L - Z_o}{Z_L + Z_o} \tag{A.1}$$

where Z_o is the characteristic impedance (50 Ω) of VNA and Z_L is the load impedance of the DUT.

The voltage drop on the load (V_L) is obtained by solving the transmission line equation[1] for the circuit diagram shown in figure A.1(a). The diagram shows the RF signal transfer from the source to the load via a transmission line of length l. Since our device is much shorter (100 μm) than the shortest RF wavelength ($\sim$ 1.9 cm at 10 GHz), it can be regarded as a lumped element i.e. no traveling wave within the device. Assuming our transmission line (coax cable connecting the RF source to the DUT) is lossless, the voltage at a given position (x) of the

[1] Thanks to Laurens Bogaert, Joris Van Kerrebrouck (ID lab), Prof. Geert Morthier, and Prof. Sin Yin (ID lab) for the discussion and input on the transmission line.

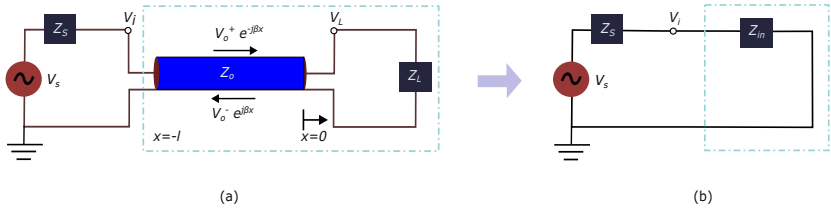

Figure A.1: (a) Circuit diagram showing the RF signal propagation through a transmission line of length l to the load, (b) an equivalent circuit diagram in terms of the input impedance (Z_{in}).

transmission line [2],

$$V_x = V_o^+ e^{-j\beta x} + V_o^- e^{j\beta x} \tag{A.2}$$

where V_o^+ and V_o^- are the forward and backward voltage amplitudes, β is the RF wave propagation constant, and x is the position of the transmission line with respect to the reference. The voltage drop over the load (at x = 0),

$$V_L = V_o^+ + V_o^- \tag{A.3}$$

Here, the two unknown constants V_o^+ and V_o^- can be obtained from the boundary conditions. Since the reflection parameter (S_{11}) is the ratio of the reflected signal to the input signal, S_{11} at the end of the transmission line,

$$\begin{aligned} S_{11} &= \frac{V_o^-}{V_o^+} = \frac{Z_L - Z_o}{Z_L + Z_o} \\ \implies V_o^- &= V_o^+ \Big(\frac{Z_L - Z_o}{Z_L + Z_o} \Big) \end{aligned} \tag{A.4}$$

Where Z_0 (= 50 Ω) is the characteristic impedance of the transmission line. Now, for the second boundary condition, we look at the beginning of the transmission line. The impedance at the input of the transmission line is given as follows [2],

$$Z_{in} = Z_o \Big(\frac{Z_L + jZ_o tan(\beta l)}{Z_o + jZ_L tan(\beta l)} \Big)$$

This Z_{in} allows simplification of the transmission line circuit as shown in figure A.1(b).

The voltage at the input of the transmission line,

$$V_i = \frac{Z_{in}}{Z_s + Z_{in}} V_s \tag{A.5}$$

Where Z_s and V_s are the source impedance and source voltage respectively. However, from equation A.2, the voltage at the input transmission line (x= $-l$) can

be formulated as follows,

$$V_i = V_o^+ e^{j\beta l} + V_o^- e^{-j\beta l} \tag{A.6}$$

Assuming the RF source impedance (Z_s) is equal to the transmission line characteristic impedance (Z_o = 50 Ω), the algebra on equation A.4, A.5 and A.6 gives

$$V_o^+ = \frac{V_s}{2} e^{-j\beta l} \tag{A.7}$$

From A.3, A.4 and A.7, the load voltage

$$\begin{aligned} V_L &= V_o^+ + V_o^+ \Big(\frac{Z_L - Z_o}{Z_L + Z_o} \Big) \\ &= \frac{V_s}{2} e^{-j\beta l} \Big(1 + \frac{Z_L - Z_o}{Z_L + Z_o} \Big) \\ &= \frac{Z_L}{Z_L + Z_o} V_s \, e^{-j\beta l} \end{aligned} \tag{A.8}$$

Hence, the voltage amplitude at the load,

$$|V_L| = \Big| \frac{Z_L}{Z_L + Z_o} \Big| |V_s| \tag{A.9}$$

Note that when a certain power (P_{RF}) is set to the RF generator, it generates a source signal such that the set power dissipates over a load of impedance Z_o = 50 Ω.

$$\implies P_{RF} = \frac{V_{rms}^2}{Z_o} = \frac{V_{disp}^2}{2Z_o}$$

$$\implies V_{disp} = \sqrt{2 P_{RF} Z_o}$$

Where V_{rms} and V_{disp} are the root-mean-square and amplitude voltage shown on the RF generator display. Since, the RF generator assumes 50 Ω load (same as the source impedance), the actual voltage amplitude generated by the RF source,

$$|V_s| = 2V_{disp} = 2\sqrt{2 P_{RF} Z_o} \tag{A.10}$$

From equation A.9 and A.10

$$|V_L| = \Big| \frac{Z_L}{Z_L + Z_o} \Big| \times 2V_{disp} = \Big| \frac{Z_L}{Z_L + Z_o} \Big| \times 2\sqrt{2 P_{RF} Z_o} \tag{A.11}$$

Hence, for a given driving power, the actual load voltage on our device can be obtained using equation A.11. We can see that when Z_L = Z_o, the load voltage V_L = V_{disp}, as expected. However, since the generator assumes impedance (Z_o) termination, it could be confusing when the output voltage from the generator is measured with an oscilloscope. Because the measured voltage amplitude appears

to be twice the set voltage amplitude (V_{disp}) shown in the display of the RF generator [3]. This doubling is observed because of a high input load impedance ($Z_L \gg Z_o$) of the oscilloscope, as can be seen from equation A.11. Similarly, in our capacitive devices, at lower frequencies, when the reactance (Z_L) is very high, V_L is also high ($\approx V_s$).

References

[1] Amr M. E. Safwat and Leonard Hayden. *Sensitivity Analysis of Calibration Standards for SOLT and LRRM*. In 58th ARFTG Conference Digest, volume 40, pages 1–10, 2001.

[2] Michael Steer. *Microwave and RF design*. NC State University, 2019.

[3] Keysight. *Why your function generator outputs twice the programmed voltage*. `https://edadocs.software.keysight.com/kkbopen/why-your-function-generator-outputs-twice-the-programmed-voltage-589745012.html`. URL accessed: 2023-03-28.

B
FEM simulation

B.1 Introduction

The linear piezoelectric constitutive equations (in strain-form) are given by [1],

$$\begin{aligned} D &= dT + \epsilon_T E \\ S &= s_E T + d^T E \end{aligned} \tag{B.1}$$

where D is the displacement field, d is the inverse piezoelectric tensor, T is the applied stress, ϵ_T is the permittivity tensor, E is the applied electric field, S is the strain tensor and s_E is the elastic compliance (inverse of stiffness/elastic) tensor of the material.

These piezoelectric constitutive equations, along with a Newtonian equation of motion, are solved to obtain the steady-state response in the frequency domain. For a multi-layer substrate with an anisotropic piezoelectric layer, these solutions are usually obtained numerically. We used a commercial FEM solver, COMSOL Multiphysics 5.5 extensively to simulate the piezoelectric response and the corresponding mechanical deformations.

B.2 Simulation of the SAW modulator

To accurately simulate the case of periodic poling of the PZT layer by the IDT electrodes, first, we calculated the electric field using an electrostatic simulation.

Then in the second step, the PZT domain orientation was aligned along these electric field lines. Now with this setup, we carried out an FEM simulation in the frequency domain to obtain the response to an RF actuation (amplitude 1V).

For the FEM simulations of the IDTs presented in chapter 3, we applied a Floquet periodic boundary condition on the left and right boundaries of the unit cell. We defined a 350 nm thick Au IDT of period 12 μm on a 200 nm thick PZT film on a silica substrate of thickness 4 $\times$ IDT period. And for the simulation shown in figure 7, we defined the IDTs on a multi-layered structure consisting of a 200 nm PZT layer, a 2.220 μm SiO_2 layer, and a Si substrate of thickness 4 $\times$ IDT period. We set the bottom 1 period of the unit cell as a perfectly matched layer (PML) domain and the bottom-most boundary as a low-reflecting boundary to absorb the incoming acoustic waves.

To visualize the propagation of the IDT-actuated acoustic waves and calculate the acousto-optic interaction in the waveguide, we created a 2D simulation setup as shown in figure B.1(a). We extended the substrate region beyond the IDT and terminated it with a PML layer (thickness = 3 $\times$ IDT period). A Si waveguide of width 450 nm and thickness 220 nm was defined underneath the PZT layer, 3 μm away from the IDT.

In figure B.1(b) and (c), we show the fundamental SAW mode launched by a 20 nm thick and 350 nm thick Au IDT (period 12 μm) respectively. We can see that for the thin IDT, the SAW transduction is stronger and the mode is mostly confined close to the surface. However, with the added mass-loading and grating reflection from a thicker IDT, as shown in B.1(c), the SAW resonance frequency is decreased, and now more acoustic energy is diffracted into the substrate.

From the simulated strain fields shown in figure B.1 and the optical field (TE mode) obtained from a mode analysis, we calculated the acousto-optic overlap integral and extracted the change in effective refractive index Δn_{eff} as shown in figure B.2. This Δn_{eff} originates from the photoelastic effect in the waveguide [2]. In our case, since the light propagates along the Si [110] direction, we applied a rotational operator on the photoelastic tensor of Si taken from [3]. Thus we obtained the following coefficients that we used for calculating the overlap integral: p_{11}= -0.090, p_{12} = 0.013, $p_{21} = p_{12}$ and $p_{22} = p_{11}$.

In figure B.2(a), we show the effect of the electrode thickness on Δn_{eff}. As expected, the index modulation decreases dramatically when the Au IDT thickness is increased from 20 nm to 350 nm IDT. In figure B.2(b), we show the effect of the number of finger-pairs (N_p) on Δn_{eff}. As expected, the resonance bandwidth decreases and the amplitude increases when N_p is increased [4].

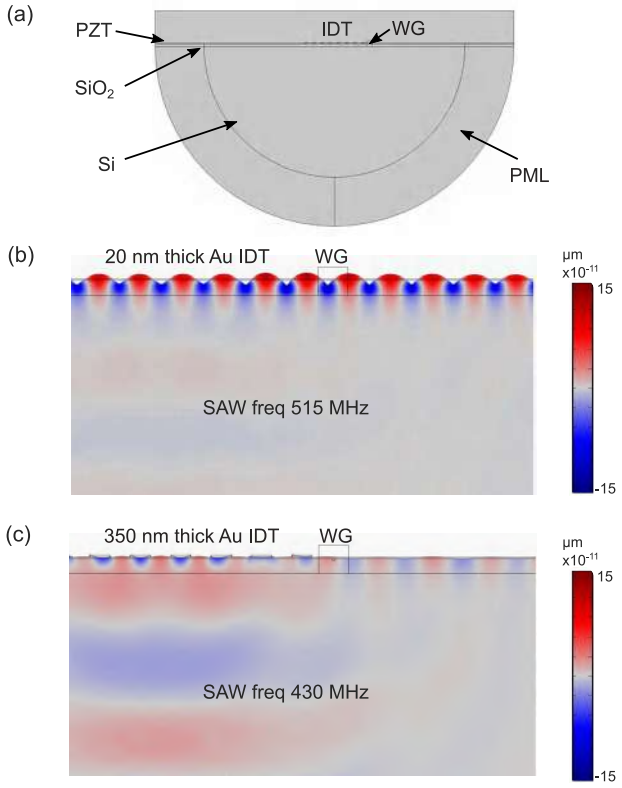

Figure B.1: (a) A 2D simulation setup showing an IDT with 4 finger-pairs defined on a 200 nm thick PZT layer on SOI. A WG is created at 3 μm spacing from the IDT, underneath the PZT layer. (b,c) Vertical displacement for the fundamental SAW mode of a 20 nm and 350 nm thick Au IDT actuated with 1V amplitude at respectively 515 MHz and 430 MHz.

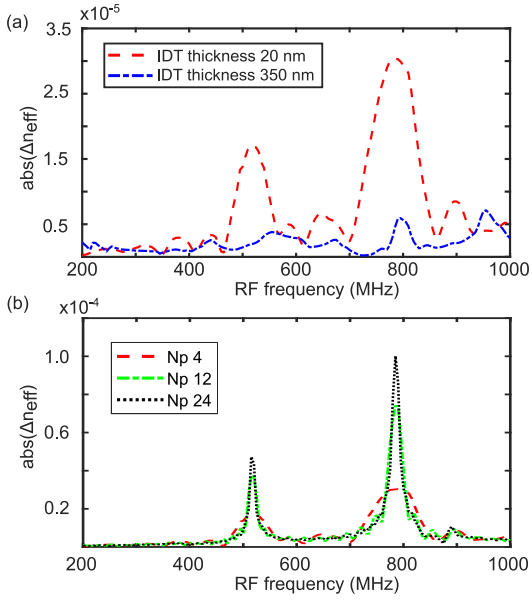

Figure B.2: Δn_{eff} calculated for 12 μm period Au IDT actuated with a 1V RF signal showing (a) effect of IDT thickness at N_p = 4, (b) effect of N_p at Au IDT thickness 20 nm.

B.3 Simulation of the suspended EOMT

We used COMSOL, a finite element method (FEM) based solver, to simulate the piezoelectric actuation of the suspended devices. To simulate the modulation from the electro-optomechanical transducer (EOMT), we defined the cross-section geometry in a 2D simulation plane as shown in figure B.3. Here the thickness of the layers were defined as: t_{AlO} = 50 nm, t_{Al} = 100 nm, t_{PZT} = 400 nm, t_{Si} = 220 nm and t_{SiO} = 280 nm. The width of the geometries were defined as: w_{el} = 1 μm, w_{Si} = 450. The separation between electrodes was defined as 4 μm and the total width of the device (w_{beam}) was taken as 6.5 μm. These geometrical values were estimated based on the optical microscope image and the SEM image of the device.

In the first step of the electromechanical simulation, an electrostatic solver was used to calculate the electric field from a voltage applied to the electrodes. The PZT domain polarization was then set along these electric field lines. This was done to account for the process whereby the PZT film was poled by a sufficiently high voltage applied to the electrodes. In the second step, an RF input signal (amplitude 1 V) was applied to the electrodes, and the piezoelectric actuation was simulated in the frequency domain. We opted for a generalized plane strain model for the solid mechanics interface to calculate the steady state solution

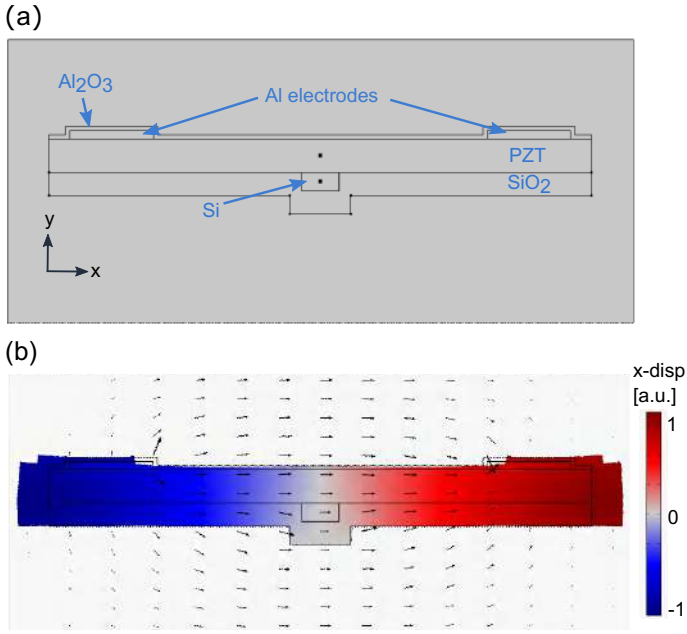

Figure B.3: (a) 2D simulation setup in the Comsol multiphysics (b) surface plot showing the x-displacement at the resonance frequency ∼ 288 MHz and the arrows denote the applied electric field.

in the frequency domain [5]. This model assumes that the suspended structure is not strictly restrained in the out-of-simulation plane direction (which was the case in our EOMT due to the extra underetching), the strains are independent of the out-of-plane coordinate and the length of the structure (out-of-simulation plane direction) is much larger than the cross-section area (in-plane). Finally, a mode solver was used to simulate the TE mode profile of the EOMT at 1550 nm.

Figure B.3(b) illustrates the simulated x-displacement of an EOMT at a mechanical resonance 288 MHz. The arrows show the electric field direction from the voltage applied to the electrodes. The PZT material properties used in the electromechanical simulation were taken from the PZT-5A [6] and the refractive index used in the optical simulation was n_{PZT} = 2.4 [7]. For other materials, standard values were taken from the literature.

References

[1] *IEEE Standard on Piezoelectricity*. ANSI/IEEE Std 176-1987, pages 0_1–, 1988.

[2] Linbo Shao, Mengjie Yu, Smarak Maity, Neil Sinclair, Lu Zheng, Cleaven Chia, Amirhassan Shams-Ansari, Cheng Wang, Mian Zhang, Keji Lai, and Marko Lončar. *Microwave-to-optical conversion using lithium niobate thin-film acoustic resonators*. Optica, 6(12):1498–1505, Dec 2019.

[3] DK Biegelsen. *Frequency dependence of the photoelastic coefficients of silicon*. Physical Review B, 12(6):2427, 1975.

[4] T. Erdogan. *Fiber grating spectra*. Journal of Lightwave Technology, 15(8):1277–1294, 1997.

[5] *How to Model Generalized Plane Strain with COMSOL Multiphysics*. `https://www.comsol.com/blogs/how-to-model-generalized-plane-strain-with-comsol-multiphysics/`. URL Accessed: 2023-07-15.

[6] Zubair Butt, Riffat Asim Pasha, Faisal Qayyum, Zeeshan Anjum, Nasir Ahmad, and Hassan Elahi. *Generation of electrical energy using lead zirconate titanate (PZT-5A) piezoelectric material: Analytical, numerical and experimental verifications*. Journal of Mechanical Science and Technology, 30(8):3553–3558, 2016.

[7] Koen Alexander, John P. George, Jochem Verbist, Kristiaan Neyts, Bart Kuyken, Dries Van Thourhout, and Jeroen Beeckman. *Nanophotonic Pockels modulators on a silicon nitride platform*. Nature Communications, 9(1):4–9, 2018.

C

Automation of the LDV setup

The following script was written in MATLAB to automate the RF driving and the deflection measurement of the MEMS actuator using the laser Doppler vibrometry (LDV) setup.

```
%% Clear MATLAB workspace and instrument connections
close all; clear; instrreset;
tStart=tic; %%start the main timer
%% User inputs %%%
my_filename='Beam_25dcenter_read1_RfreqScan_postpoling
    ';
showliveplot=0; %%% 1 to see live plot in the loop,
    any other digit to hide
my_folder='C:\Program Files (x86)\Gage\CompuScope\
    CompuScope MATLAB SDK\Main\Irfan_LDVdata\';
%% FG parameters
start_Rfreq=50e3; stop_Rfreq = 3e6; step_Rfreq=1e3; %1
    kHz normally
Vpp= 10; %RF peak to peak voltage
pausetime=10e-3; %pause time (during sweep) to let the
     vibration stabilize a bit
%% DAQ parameterstmtool
Fs=65e6;
dpoints= 2^18; %total number of data points post-
    trigger
Impd= 1e6; % channel impedance in Ohm
```

```
InpRange= 20000; % channel input  in mV
peaksearch_fspan= 10e3; %Hz
collect_data=0; %% 0 for voltage data, 1 for rawdata (
    then apply the datconversion)

%% Instrument Connection
% Find a VISA-USB object.
interfaceObj = instrfind('Type', 'visa-usb', 'RsrcName
    ', 'USB0::0x0699::0x0343::C023371::0::INSTR', 'Tag'
    , '');
% Create the VISA-USB object if it does not exist
    otherwise use the object that was found.
if isempty(interfaceObj)
    interfaceObj = visa('NI', 'USB0::0x0699::0x0343::
        C023371::0::INSTR'); %or TEK
else
    fclose(interfaceObj);
    interfaceObj = interfaceObj(1);
end
% Create a device object.
deviceObj = icdevice('tek_afg3000', interfaceObj);
% Connect device object to FG. initiate DAQ
connect(deviceObj);
run('AddPath.m'); %add all the directories of gage DAQ
[handle]= My_GageAcquire_2(Fs, dpoints, Impd, InpRange
    );
% Configure property value(s).
set(deviceObj.Waveform(1), 'Shape', 'sin');
set(deviceObj.Voltage(1), 'Amplitude', Vpp);
set(deviceObj.Frequency(1), 'Mode', 'continuous');

RF_freq=start_Rfreq:step_Rfreq:stop_Rfreq;
peak_amp=(start_Rfreq:step_Rfreq:stop_Rfreq)*0; %%fill
    with 0 for now
%%%%%%%%%% start Optional 1a %%%%%%%%%%%%%%%%%%
if showliveplot==1
    showplot = animatedline('Color','r','LineWidth',2)
        ; %dynamic plotting
    xlabel('RF freq (Hz)'); ylabel('Peak amplitude');
        ylim([0 10e-9]);
end
% %%%%%%%%%% end Optional 1a %%%%%%%%%%%%%%%%%%
for i=1:length(RF_freq)
    tic %start timer
```

```
    set(deviceObj.Frequency(1), 'Frequency', RF_freq(i
        ));
    pause(pausetime); %give  a bit of stabilization
        time to the mems device
    %%record daq
    [t, data]= My_capture_2(handle, collect_data);
    %%processing-->fft+peak value
    n_pad = pow2(nextpow2(length(data))); %padding
    freq = (0:n_pad-1)*(Fs/n_pad); %Hz
    data = highpass(data,50E3,Fs); %fpass=50kHz in
        voltage
    signal_amp_timedomain=cumsum(data)*(0.1)./Fs; %
        velocity conversion 100 mm/s/V
    signal_amp_freqdomain = 2*abs(fft(
        signal_amp_timedomain,n_pad))/length(
        signal_amp_timedomain);
    indx = find(abs(RF_freq(i)-freq) <
        peaksearch_fspan/2); %starting index in a freq
        span
    peak_amp(i)= max( signal_amp_freqdomain(indx(1):
        max(indx))  );

    loop_finish =100* i/length(RF_freq); time_left=toc
        *(length(RF_freq)-i);
    disp(['loop finished =', num2str(loop_finish),'%',
        '           time left ~',num2str(time_left), 's
        ' ]);
    if showliveplot==1
        addpoints(showplot,RF_freq(i),peak_amp(i));
        title([' time left ~ ',num2str(time_left), 's'
            ]); % toc %elapsed timer
        drawnow
    end
end
%%%%%%%%%% start Optional 2 %%%%%%%%%%%%%%%%%%
% % convert the data to volts IF RAW DATA collected
% % Get the SampleResolution and SampleOffset from
   QueryAcqusition rather
% % then from GetSystemInfo because these values might
    change if FPGA images
% % are loaded

if collect_data==1
    [ret, acq] = CsMl_QueryAcquisition(handle);
```

```
    [ret, chan] = CsMl_QueryChannel(handle, 1); %
        channel=1
    peak_amp = (((acq.SampleOffset - double(peak_amp))
         / acq.SampleResolution) * (chan.InputRange /
        2000)) + (chan.DcOffset / 1000);
end
%%%%%%%%%% end Optional 2 %%%%%%%%%%%%%%%%%%
ret = CsMl_FreeSystem(handle);
fg=figure; plot(RF_freq*1e-6, peak_amp);
xlabel('RF freq (MHz)');ylabel('Amplitude (m)');
title(my_filename,'Interpreter', 'none');
% saveas(fg,[my_folder,my_filename,'.fig']);
% export_data= [RF_freq' , peak_amp']; %%transpose to
    make columns from arrays
% save ([my_folder,my_filename,'.asc'],'export_data',
    '-ASCII'); %-ascii-double
%% Disconnect and Clean Up: disconnect device object
    from the hardware and delete
disconnect(deviceObj);
delete([deviceObj interfaceObj]);
tEnd=toc(tStart); %%stop the main timer
disp(['Your program finished in ', num2str(tEnd),' s'
    ]);
%%%%% optionql 3 %%%%%%%announce
defaultString = ['your program is finished'];
NET.addAssembly('System.Speech');
obj = System.Speech.Synthesis.SpeechSynthesizer;
obj.Volume = 100;
Speak(obj, defaultString);
%%%%%%%%%%%% The end %%%%%%%%%%%%
```